View metadata, citation and similar papers at core.ac.uk
brought to you by CORE
provided by Western Washington University

Western Washington University
Western CEDAR

WWU Graduate School Collection
WWU Graduate and Undergraduate Scholarship

2010

# Ambient pressure organic semiconductor thin film growth by ambient axisymmetric spray

Kevin A. (Kevin Anthony) Bufkin
*Western Washington University*

Follow this and additional works at: https://cedar.wwu.edu/wwuet

Part of the Chemistry Commons

## Recommended Citation

Bufkin, Kevin A. (Kevin Anthony), "Ambient pressure organic semiconductor thin film growth by ambient axisymmetric spray" (2010). *WWU Graduate School Collection*. 84.
https://cedar.wwu.edu/wwuet/84

This Masters Thesis is brought to you for free and open access by the WWU Graduate and Undergraduate Scholarship at Western CEDAR. It has been accepted for inclusion in WWU Graduate School Collection by an authorized administrator of Western CEDAR. For more information, please contact westerncedar@wwu.edu.

# Ambient Pressure Organic Semiconductor Thin Film Growth by Ambient Axisymmetric Spray

By
Kevin Anthony Bufkin

Accepted in Partial Completion
Of the Requirements for the Degree
Master of Science

Dean of the Graduate School, Moheb A. Ghali

ADVISORY COMMITTEE

Thesis Advisor, Dr. David Patrick

Dr. Brad Johnson

Dr. Mark Bussell

Dr. Janelle Leger

**Master's Thesis**

In presenting this thesis in partial fulfillment of the requirements for a master's degree at Western
Washington University, I grant to Western Washington University the non-exclusive royalty-free right to archive, reproduce, distribute, and display the thesis in any and all forms, including electronic format, via any digital library mechanisms maintained by WWU.

I represent and warrant this is my original work, and does not infringe or violate any rights of others. I warrant that I have obtained written permissions from the owner of any third party copyrighted material included in these files.

I acknowledge that I retain ownership rights to the copyright of this work, including but not limited to the right to use all or part of this work in future works, such as articles or books.
Library users are granted permission for individual, research and non-commercial reproduction of this work for educational purposes only. Any further digital posting of this document requires specific permission from the author.

Any copying or publication of this thesis for commercial purposes, or for financial gain, is not allowed without my written permission.

Kevin Bufkin
May, 2010

# Ambient Pressure Organic Semiconductor Thin Film Growth by Ambient Axisymmetric Spray

A Thesis

Presented to

The Faculty of

Western Washington University

In Partial Fulfillment

Of the Requirements for the Degree

MASTER OF SCIENCE

By

Kevin Bufkin

May, 2010

# Abstract

Interest in using organic semiconductors in applications such as large area displays, photovoltaic devices, and radio frequency identification tags stems in part from their prospects for enabling significantly reduced manufacturing costs compared to traditional inorganic semiconductors. However many of the best performing prototype devices produced so far have involved expensive or time-consuming fabrication methods, such as the use of single crystals or thin films deposited under high vacuum conditions. This thesis examines a new approach for growing low molecular weight organic crystalline films at ambient conditions based on an organic vapor-liquid-solid growth (OVLS) mechanism using thermotropic nematic liquid crystal (LC) solvents.

# Acknowledgements

I would like to acknowledge the constant support of my thesis advisor, Dr. David L. Patrick, for the patience, wisdom and encouragement he provided during the course of this study. Dr. Patrick was a constant source of inspiration, to which I owe my greatest appreciation.

In addition I must thank Dr. Brad Johnson for his help in the realm of surface mechanics and electric field study, as well as his willingness to aid in my understanding of these topics.

I would like to thank my graduate committee, Dr. Mark Bussell, Dr. Janelle Leger, and Dr. Brad Johnson for their help in completion of my thesis.

I would also like to thank Mr. Dan Shaw and Mr. Brooks Ohlson for their aid along the way.

Also, I must thank Mr. Geoff Landis at the machine shop of Western Washington University for his tireless efforts. His expert advice and manufacturing skill made a large contribution to this project.

# Table of Contents

Abstract iv

Acknowledgements v

List of Tables viii

List of Figures ix

Chapter 1: Introduction to Organic Semiconductors 1

Charge Transport Mechanisms 3

Organic Semiconductor Thin Film Fabrication Methods 9

Organic Vapor Liquid Solid Deposition 18

Goals of Thesis 22

Chapter 1 References 23

Chapter 2: Ambient Axisymmetric-Spray 29

Particle Aggregation Model 33

Particle Deposition Model 40

Experimental Data 49

Growth Kinetics 56

Results 68

Chapter 2 References 71

Chapter 3: Ambient Axisymmetric Spray with Particle Charging 72

Corona Discharge 76

Modified AAS System 79

Characterization of the Modified AAS System 81

Film Purity 87

Modeling Deposition Rate 94

Chapter 3 References 100

Chapter 4: Results, Conclusions of Future Work 101

Theoretical Framework 102

Improvements 103

Patterning 107

Summary 109

**List of Tables** **Page**

1: Collection of organic semiconductor based devices and their methods of manufacture 17

2: Experimental parameters associated with the AAS method 30

3: Additional AAS parameters 79

4: Percent impurity calibration curve data 90

**List of Figures** **Page**

**Chapter One**


1: Schematic of inorganic semiconductor operation 3

2: Schematic of charge carrier hopping in organic semiconductors 5

3: Film performance as measured by charge carrier mobility 5

4: Crystallographic orientation of pentacene and resistivity anisotropy 6

5: Rubrene single crystal mobility anisotropy 7

6: AFM image of a pentacene film grown by OMBE 7

7: Top contact field effect transistor 8

8: Solution grown organic semiconductor crystals 10

9: Anthracene arrays grown on SAMs 11

10: Schematic of zone casting technique 11

11: schematic of solution-sheared technique 12

12: Schematic of a basic OMBE setup 12

13: OMBE method for growth on patterned substrates 13

14: Selective growth of nanocrystals 14

15: Tetracene crystals grown in a liquid film 16

16: OVLS deposition schematic 18

17: Optical images of tetracene films grown in differing environments 18

18: Orientational mechanism of LC imprinting 19

19: Structures of tetracene and anthracene 20

**Chapter Two**


2-1: Schematic of the AAS chamber 31

2-2: Particle size distribution as a function of time of flight 36

2-3: Monomer concentration versus time of flight 37

2-4: Particle size distribution as a function of initial concentration 39

2-5: Schematic of the axisymmetric stagnation-point flow region 40

2-6: Deposition rate with respect to flow rate 44

2-7: Turbulence versus laminar flow 45

2-8: Particle size distribution and deposition rate as a function of viscosity 47

2-9: Deposition rate as a function of gas density 48

2-10: SEM of a large vapor phase aggregates 49

2-11: POM of tetracene films grown at differing flow rates 50

2-12: Deposition volume versus sublimation rate 51

2-13: Deposition volume versus deposition time 52

2-14: Radial intensity study 54

2-15: Representation of epitaxial growth 56

2-16: Examples of crystals with differing fractal dimensions 57

2-17: Regimes of epitaxial growth 58

2-18: SEM images of tetracene thin film growth study 60

2-19: AFM of long deposition time tetracene morphology 61

2-20: Nucleation density versus time 63

2-21: Nucleation density versus flux rate 64

2-22: Size scaling plot for the low coverage images 67

2-23: Tetracene thin film grown by AAS 69

**Chapter Three**

3-1: Regions of the point-to-plane corona discharge 76

3-2: Radial current density plot for a point-to-plane corona discharge 77

3-3: Schematic of the AAS system with the addition of particle charging 80

3-4: Current/voltage plot 83

3-5: Radial distribution plots for different $V_{ft}$ values 84

3-6: Long exposure time photography image of the ionization region 85

3-7: Oxidative products of tetracene 87

3-8: IR spectra of 98% pure tetracene 89

3-9: Impurity calibration plot 91

3-10: Purity of tetracene films grown by AAS in different environments 93

3-11: Theoretical deposition rate versus particle size with particle charging 96

3-12: Theoretical deposition rate as a function of substrate voltage 97

3-13: Experimental deposition rate as a function of substrate voltage 98

**Chapter Four**

4-1: Films of anthracene and tetracene which show evidence of surface based growth 103

4-2: Anthracene thin film grown by the AAS method 104

4-3: Optical image of an anthracene film 105

4-4: Radial UV-Vis intensity study 106

4-5: Tetracene patterned film by shadow masking 107

4-6: Tetracene patterned films by electro masking 108

# Chapter One

## Introduction to Organic Semiconductors: Properties and Methods of Manufacture

Ever since the invention of the transistor in 1947, inorganic semiconductor based devices have dominated the electronics industry.[1] Although semiconducting behavior in an organic material (iodine-doped polyacetylene) was first observed over 30 years ago, organic semiconductors have until relatively recently been considered little more than a novelty.[2] However, in the last 15 years, organic semiconductors have begun to be viewed – and have started to be used – as viable substitutes for inorganic semiconductor materials in certain niche applications.[3,4] Their utility stems from the unique properties of organic semiconductors, including their compatibility with flexible substrates, their chemically tunable electronic properties, and their potentially lower cost to manufacture. In order for organic semiconductor materials to see more widespread use however, a number of issues that arise from scaling up their manufacturing methods must be solved and their performance must continue to improve. This thesis focuses on addressing one of these issues, namely, the need to develop methods for preparing high quality, large area films of organic semiconductors rapidly and at low cost.

Organic semiconductors seem to offer the greatest potential as substitutes for inorganic semiconductors in low cost/low performance devices rather than high-performance devices such as computer memory, due to their lower charge carrier mobility and on/off current ratios.[5,6] Already, organic semiconductor materials have been used as active layers for devices such as organic solar cells,[7,8,9,10] organic light

emitting diodes,[11,12,13,14] and organic field-effect-transistors.[15] In fact, the properties of organic semiconductor materials allow for devices with distinct advantages over their inorganic counterparts in these areas. For example, organic solar cells have been prepared using flexible substrates compatible with mounting on a range of surfaces, from curved roofs, to cars and even clothing.[16,17] Organic field effect transistors have been used to manufacture electronic paper,[18,19] humidity and chemical sensors, [20,21,22,] pressure transducers,[23] and radio-frequency identification tags.[24,25] Organic light emitting diodes have shown significant advantages over traditional lighting including use in what some observers consider to be the future standard for high resolution, high contrast ratio televisions as well as displays which can be embedded in fabrics.[26]

Organic semiconductors come in a variety of forms, the three most important being organic molecular crystals (i.e. low molecular weight organic crystalline solids), polymers, and liquid crystals. Organic molecular crystal semiconductors, studied both in single crystal and thin film form, currently show the most promising electrical properties.[27] Polymeric semiconductors, however, are easier to process and thus appear to be more suitable for printed electronics.[27] Liquid crystal semiconductors are a relatively new class of materials and have shown promising results, but have yet to find practical application.

The performance of organic semiconductor based devices is highly dependent upon the electrical properties of the semiconducting layer,[28,29,30,31,32,33,34] typically characterized by its charge carrier mobility, defined as the ratio of the charge carrier velocity to the magnitude of an applied field (to be discussed later).[35]

## Section 2
## Charge Transport Mechanisms

Even though both organic semiconductor and inorganic semiconductor materials are capable of performing similar functions, their mechanisms of charge transport differ significantly. Charge transport in inorganic semiconductor materials is characterized by band theory in which bonding and non-bonding orbitals widen to form delocalized energy bands spanning the length of the solid. This is represented in figure 1A, which shows an energy level diagram for a typical inorganic semiconductor. In the ground state, the valence band is populated by bonded valence orbital electrons and the conduction band remains empty. Excitation of an electron from the valence band to the conduction band can occur by a number of mechanisms including photon capture, thermal excitation, or charge carrier injection. When an electron is excited from the valence band to the conduction band it leaves behind a positively charged electron deficient region known as a "hole" (denoted $h^+$) in the valence band (figure 1B). Both the conduction band electrons and the valence band holes can be mobile, serving to transport charge within the material. In the case of a semiconductor under no external influence (figure 1B), the charge carriers will drift

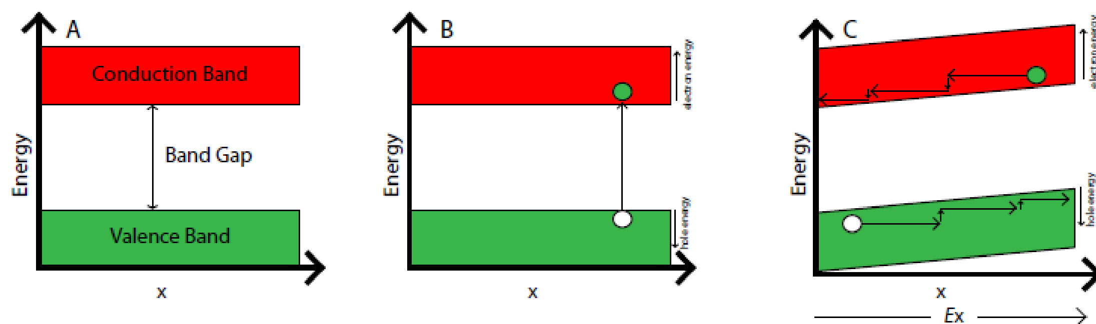


Figure 1: A) illustration of the delocalized band energy levels. B) Excitation of an electron from the valence band. C) Under an applied field, charge carriers drift in a physical direction based on the field direction.

randomly so that their total averaged velocity will be zero. Application of an electric field results in a net flow of charge carriers within the semiconductor, and hence a flow of current as shown in figure 1C. The speed at which a charge carrier travels relative to the strength of the applied field is known as the charge carrier mobility, $\mu$, measured in cm $V^{-1}$ $s^{-1}$. The conductivity of a semiconductor obeys equation 1, where $\mu_e$ and $\mu_h$ are the mobilities of electrons and holes respectively, $n$ as the density of electrons, $p$ as the density of holes, and $e$ as the charge on an electron. [36]

(1) $$\sigma = en\mu_e + ep\mu_h$$

Unlike the covalently bonded atoms in an inorganic semiconductor, the molecular constituents of an organic semiconductor interact through relatively weak van der waals forces. Consequently, they do not form the same kind of delocalized bonding networks characteristic of inorganic semiconductors and thus charge transport occurs via a different mechanism. Although at low temperatures where destructive lattice vibrations (phonons, which increase intermolecular separation and thus destroy the bands) are small, organic semiconductor materials can show band-like transport similar to inorganic semiconductor materials like silicon discussed above,[37] the widths of the conduction and valence bands are on the order of tens to hundreds of meV, much smaller than that of their inorganic counterparts.[38]

At elevated temperatures charge transport occurs instead by an incoherent hopping mechanism, in which charge carriers overcome an energy barrier to transfer or “hop” from a molecular orbital on one molecule to an empty orbital on the next molecule. Since all organic semiconductors contain conjugated π systems, their molecularly delocalized π bonding networks are primarily involved in charge transport. Figure 2-A illustrates these hopping events for an organic semiconductor under no applied field in which charge migration is diffusive, with no net flow of current. In figure 2-B, a bias is applied and thus charge carriers tend to travel downhill to lower energy states. The degree of overlap between the π orbitals of neighboring molecules largely determines the size of this energy barrier. Consequently, highly ordered molecular crystals with closely interacting π orbitals tend to possess the largest charge carrier mobilities.

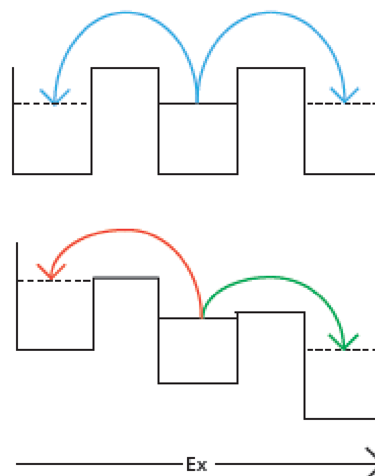

Figure 2: A) hopping of an electron with no applied field. Note that there is equal energy requirement for transport in both directions. B) hopping of an electron with an applied field. In this case, there is a high energy requirement for the electron to hop against the field, while hopping in the direction of the field will result in a drop in potential.

Due to the role of π orbital overlap in charge transport, a well ordered and densely packed crystal structure is necessary for high charge

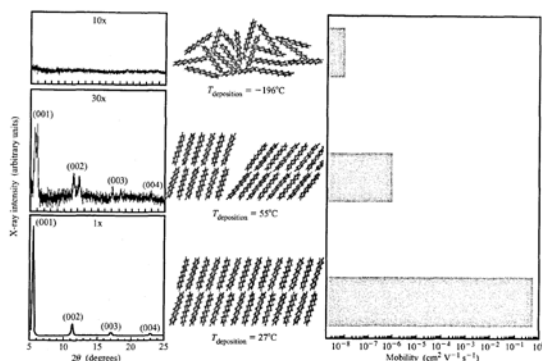

Figure 3: Film performance as measured by charge carrier mobility.
**Left:** X-Ray Diffractograms showing degree of film order.
**Middle:** Visual representation of pentacene film order.
**Right:** Electron mobility measurements for the three degrees of order. Adapted from [39]

carrier mobility. This is illustrated in figure 3, which shows how the degree of charge carrier mobility in pentacene films depends on the degree of molecular order. Simply by varying the degree of crystallinity the charge carrier mobility changes by up to 11 orders of magnitude.[39] Therefore, an organic semiconductor thin film must be free of structural defects in order to function efficiently.

In addition to structural defects, charge carrier mobility in organic semiconductors is also highly sensitive to impurities. Impurities have severe detrimental effects due to their ability to act as charge carrier traps (a charge carrier trap localizes a mobile charge carrier due to strong molecule/charge carrier interactions) as well as their ability to create lattice distortions, thus decreasing the molecular order.[40] For example, when the percentage of 6,13-pentacenequinone impurity in a pentacene crystal was decreased from 0.17% to 0.028%, the charge carrier mobility roughly doubled.[41] Consequently, high purity is also required in addition to a high degree of structural (crystallographic) order.

A third consideration in efforts to prepare high mobility organic semiconductor materials is crystallographic orientation. To illustrate, figure 4-A shows pentacene's crystal structure, with molecules packed in a herringbone arrangement having face-to-edge and end-to-end orientation. This molecular orientation leads to anisotropic

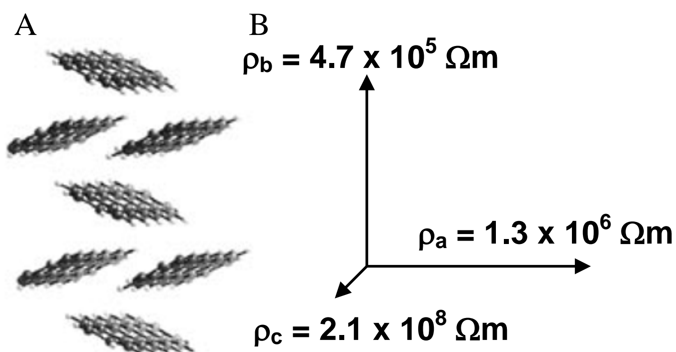


Figure 4: Crystallographic orientation of pentacene. B) Anisotropic resistivity of a macroscopic pentacene crystal with respect to direction of charge carrier travel.

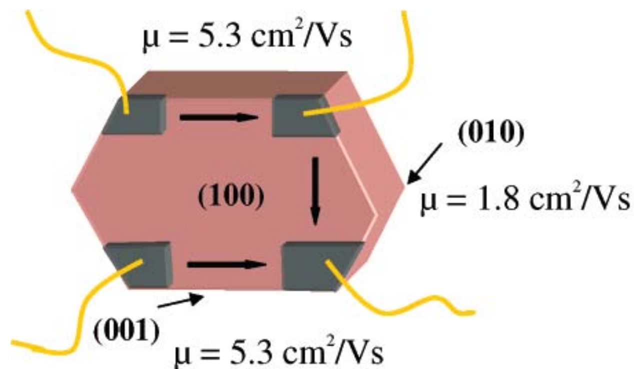

Figure 5: Rubrene single crystal device patterned with electrodes. Adapted from [44]

resistivity based on the direction of charge carrier travel.[42] For charge carriers moving from face-to-edge, there exists the highest degree of π orbital overlap and thus the energy barrier for hopping is small. In contrast, there exists comparatively little π orbital overlap for end-to-end molecules and thus the energy barrier for hopping is higher in that direction. Figure 4-B shows how these properties affect charge transport in a macroscopic single crystal. Depending on crystallographic orientation and thus the degree of π -orbital overlap, resistivity can vary by up to three orders of magnitude.[43] As another example, the charge carrier mobility in a rubrene single crystal can also vary by roughly a factor of three based on crystallographic orientation (figure 5).[44] Therefore, in addition to molecular order and low impurity levels, long range crystallographic orientational order is required to produce high performance organic semiconductor devices.

Finally, most applications of organic molecular crystalline semiconductors involve thin films, such as the pentacene film shown in figure 6, which was grown by organic molecular beam epitaxy (OMBE).[45] Note the random orientation

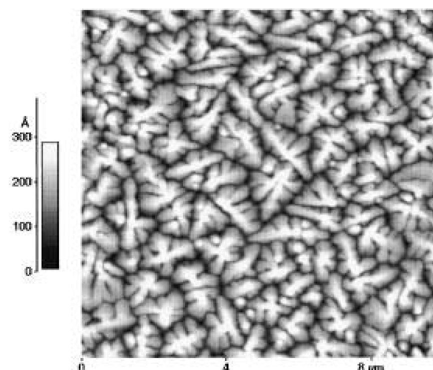
Figure 6: AFM image of a Pentacene film grown by OMBE. Adapted from [45]

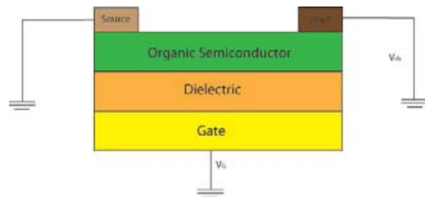

Figure 7: Top contact organic field effect transistor.

of the pentacene crystals as well as the irregular inter-crystal spacing, typical of OMBE grown films. Now consider the use of this film in an application, such as the organic field effect transistor shown in figure 7. As charge carriers travel from the source to the drain electrodes, they encounter grain boundaries which they must traverse to move from one crystallite to the next. Each of these hopping events presents a barrier to charge transport analogous to a series resistor, impeding charge flow and decreasing the overall mobility of the film. Additionally, as the crystals are randomly oriented, mobility can vary widely over the length of the film. Thus, the final requirement for a high quality organic semiconductor thin film is that it must be composed of relatively large densely packed and properly oriented grains.

## Section 3
## Organic Semiconductor Thin Film Fabrication Methods

I will now discuss some of the most common ways of fabricating organic semiconductor devices, including some new approaches developed in the past few years aimed at improving upon traditional methods. Organic molecular crystal based devices usually consist of either a single crystal or a thin film in which a large number of crystals are packed closely together. In some cases, single crystal devices actually rival the electrical properties of inorganic semiconductor based devices, but are notoriously difficult to prepare and work with.

The fabrication of single crystal devices begins either with hand-picking a crystal of the desired morphology and then manually placing it on a device substrate, or randomly casting a collection of crystals onto pre-patterned source-drain electrodes.[35] Both methods are incompatible with high throughput manufacturing due to the large number of delicate steps required for fabrication.[46] Additionally the hand-picking method has been shown to cause contamination and damage to the fragile organic semiconductor crystals, which can decrease the performance of the device.[47] Solution based transfer methods offer an alternative to hand picking, but can introduce microscopic debris from casting solvents, and there is no suitable method for controlling deposition onto prefabricated electrodes. Therefore, although single-crystal based devices are useful for controlled, fundamental studies, their incorporation into practical commercial applications does not appear likely.[48,49]

For practical applications, thin film-based devices are much more promising. Methods for their preparation include OMBE, solution-processing, and dip coating (a

relatively simple procedure in which single crystals suspended in a solution are deposited on a substrate by dipping the substrate into the solution). As discussed above, crystallographic alignment is a crucial property for organic semiconductor thin film performance. Therefore, methods of organic semiconductor thin film growth which do not induce film alignment are typically combined with a secondary alignment method. Presented in the following section are some relevant fabrication methods.

Solution-processing has proven an attractive field due to its ability to grow large crystals of tunable morphology. These methods are based on different ways to controllably supersaturate a solution and promote regulated nucleation. Supersaturation can be achieved in a number of ways including cooling a saturated solution, evaporating solvent from a saturated solution, or depositing additional material into a pre-saturated solution. Shown in figure 8 are solution grown crystals which show sizes much larger than those grown by OMBE.[50] While solution processing can grow high quality, phase pure crystals, parameters such as solvent evaporation rate, substrate temperature, and organic semiconductor solubility must be carefully selected and controlled. Also, solution processing has been known to introduce impurities either from the solution or from unwanted chemical reactions with dissolved materials.

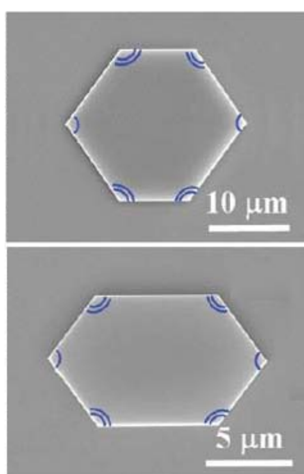

Figure 8: Solution grown organic semiconductors. Adapted from [50]

Solution-processing has also been used in conjunction with a number other of methods to induce micro and macro-structural order. One such application involves patterned self assembled monolayers (SAMs) as templates. SAMs have shown an ability to direct the deposition of conjugated polymers,[51,52] oligomers[53] and low molecular weight organic semiconductor thin films.[90,54,55] Patterning of organic semiconductors by this method requires treating a substrate to create lyophilic and lyophobic areas. A supersaturated solution of the desired material is then cast onto the substrate, usually by spin coating. As unfavorable interaction between solvent and substrate drive the solution to recede to the lyophilic areas, both soluble and insoluble materials are drawn with it. Figure 9 shows a film of anthracene crystals grown on micropatterned SAMs after solution recession.[61] By swapping lyophobic and lyophilic areas, it is possible to create either small square anthracene films or a film with anthracene deficient areas. This technique can afford another level of order by fashioning line defects in the substrate to incorporate 1D macroscopic order.[35]

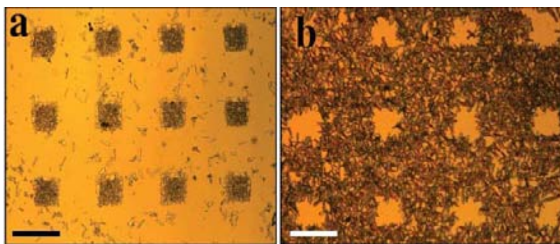


Figure 9: Optical images of anthracene arrays on SAMs. A) anthracene squares B) anthracene background. Adapted from [61] copyright 2005 American Chemical Society

Another recently developed solution-processing method capable of controlling structural order is zone-casting. A schematic representation of this

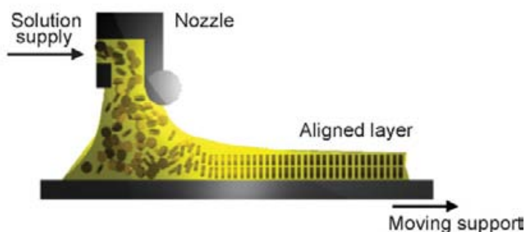


Figure 10: Schematic presentation of zone-casting technique. Adapted from [56]

technique is presented in figure 10. In the zone casting technique a continuously supplied solution is spread by means of a nozzle onto a moving support. Both the solution and the support are thermally controlled to reach an appropriate ratio of solvent evaporation and supply, creating a stationary gradient of concentration. The resulting meniscus controls direction of crystallization while retaining the solution based growth advantages discussed earlier.[56]

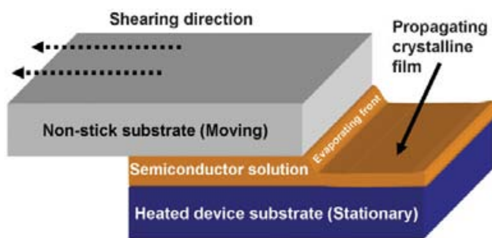

Figure 11: Schematic of the solution-sheared technique. Adapted from [89]

Solution-sheared deposition is another solution processing based method designed to pattern films on isotropic substrates.[57] Figure 11 illustrates how this method employs a small volume of a highly dilute organic solution sandwiched between two preheated silicon substrates. The top wafer is treated to be lyophillic while the bottom wafer serves as the device substrate. As the top wafer is drawn past the substrate, it exposes a dilute liquid front that evaporates and produces a seed film containing multiple crystal grains. These seed crystals serve as nucleation sites for the remaining molecules in solution which propagate along the direction of shearing, leading to a good degree of macroscopic film order.

Most organic semiconductor thin films designed for use in OFETs have been grown by OMBE.[58] A typical OMBE chamber consists of two regions, a

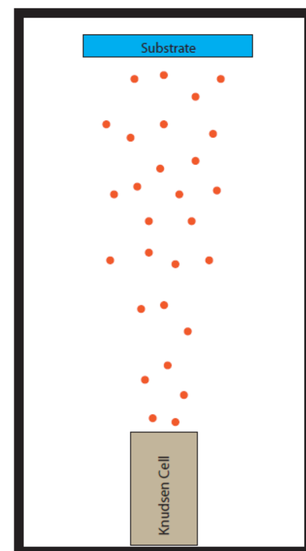

Figure 12: Schematic of a basic OMBE setup

Knudsen cell and a deposition region, both heated and held at high vacuum, illustrated in figure 12. In the Knudsen cell, an organic semiconductor material is heated above its sublimation temperature to produce a stream of vapor phase particles. The sublimated vapor is then transferred to a cooler condensing region where it can be deposited on a range of substrates.[59,60] OMBE under high vacuum can produce high quality organic semiconductor thin films since there is little to no vapor phase aggregation and substrate surfaces can be kept immaculately clean.[58,103,104,101,106] The necessity of high vacuum is this method's main drawback however, since working in a high vacuum environment introduces significant costs. Also, films grown by traditional OMBE methods consist of randomly oriented, small grain sizes with irregular packing, similar to the pentacene film presented earlier.

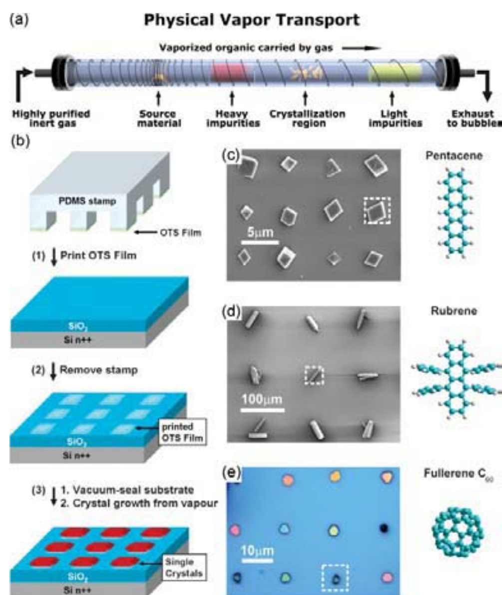


Figure 13: OMBE method for growth of organic semiconductor single crystals a) Deposition chamber with in situ purification. b) Schematic of microcontact printing. c-e) patterned arrays of organic semiconductor single crystals. The dotted square indicates size and location of OTS-stamped domains. Adapted from [60]

The OMBE technique has been combined with substrate preparation to selectively nucleate organic semiconductor crystals.[60] For example, figure 13 shows films of several organic semiconductor materials deposited onto patterned octadecyltrichlorosilane stamped regions which lead to selective crystal growth in the patterned areas.[60] The films show regular inter-crystal spacing and high chemical purity. Note however the small crystal sizes

(compared to solution based growth) as well as the random crystallographic orientation inherent in OMBE based methods. Even with these shortcoming, the resultant organic semiconductor thin films were incorporated with flexible plastic OFETs which showed comparable characteristics to amorphous silicon transistors.[61,62,63]

Another recently developed OMBE based patterning method involves the selective growth of nanocrystalline seeds scavenged by the dip coating method.[64] As shown in figure 14, selected nanocrystals are placed on a substrate and successively grown by OMBE to create nanowires with axial control inherent in the dip-coating method.[95] This simple method has shown capable of creating complicated structures such as nanowire grids. While this method provides a high degree of alignment, there is no high throughput method for single crystal creation and casting, and selection of the seed crystal must be done with care as the resultant crystals will grow in a manner based on the morphology of the seed.

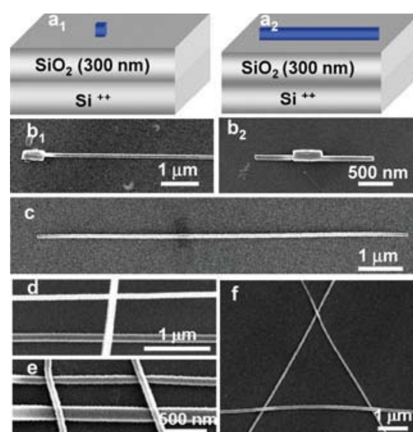


Figure 14: Selective growth of nanocrystals. It can be seen that growth will occur on either one or both sides of the crystal. Note that the wires are highly linear, and with patterned substrates complicated wire structures have been grown. Adapted from [95]

Due to the importance of film alignment, several alignment method have been employed and used in conjunction with existing fabrication methods. External magnetic and electric fields have been used to induce organic semiconductor thin film alignment since organic semiconductors often contain conjugated $\pi$-orbitals and therefore exhibit diamagnetic anisotropy. Large molecular crystals can be directly

aligned by this method. Also, liquid crystals (LCs) and SAMs can be influenced by electric and magnetic fields, resulting in alignment of crystals immersed in solution.[65,66,67,68,69,70]

Treating substrates to induce alignment of organic semiconductor thin films can be achieved a number of ways. One such method of alignment is mechanical rubbing. This simple technique needs only mild pressure and temperature, allowing for compatibility with fragile substrates. Line defects can be "rubbed" into a substrate using a number of materials including Teflon bars, soft hair brushes, velvet cloths, or rayon pile cloths.[35] This technique has been successfully used to align both LCs and small conjugated molecules.[71,72,73,74] Line defects can also be created using a process called photoalignment, in which a photosensitive polymer is exposed to a linearly polarized UV light, causing preferential cross-linking along the polarizing direction, resulting in a larger number of polymer chains oriented in one particular direction.[35] This technique has also been shown to successfully align LCs and small conjugated molecules like pentacene through the alignment of polymer layers such as polyimide.[75,76,77,78,79,80] Photoalignment offers advantages over rubbing by reducing problems such as sample contamination, static charge generation, and scratches (surface roughness affects nucleation and growth of crystals).[81,82]

One method of particular relevance to the present work was performed by Sokolowski *et al.* in which a high vacuum OMBE chamber was used to continuously supersaturate a liquid solution to grow crystals of the organic semiconductor tetracene.[83] As shown in figure 15, the resulting crystals had exceptionally large sizes. As a result of this study, it was confirmed that factors such as nucleation

density and crystal morphology inside a liquid medium could be controlled by deposition rate. However, this method still required a high vacuum environment and affords no control over crystallographic orientation.

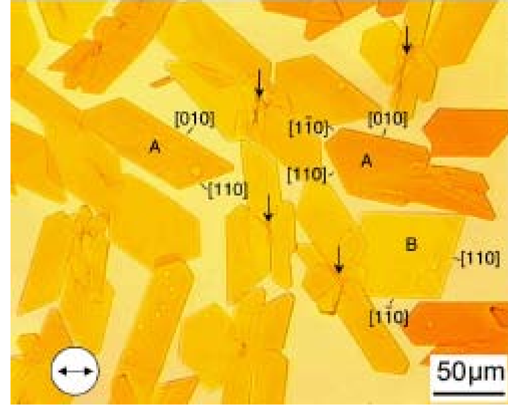

Figure 15: Tetracene crystals grown in a liquid film. Adapted from [83]

Another method of particular interest was presented by Forrest *et al.* in which a low pressure (0.1 to 10 torr) OMBE chamber was used to grow organic semiconductor thin films by passing a flow of carrier gas containing an organic semiconductor vapor over the substrate.[84] This deposition method showed advantages over other high vacuum OMBE methods by allowing for multi-component deposition over larger areas and the use of somewhat higher pressures.[85] This approach is also compatible with patterning when incorporated with shadow masking and changes in the geometry of the vapor jet nozzle.[85]

A summary of the properties of films prepared by the preceding methods is given in table 1. For reference, the minimum charge carrier mobility acceptable for an organic thin film transistor is 1 V $cm^{-2}$ $s^{-1}$, with any mobility exceeding 10 V $cm^{-2}$ $s^{-1}$ being regarded as high quality.[27]

| Compound | Organic Semiconductor Type | Organic Semiconductor Growth Method | Mobility ($cm^2 V^{-1} sec^{-1}$) | $I_{on}/I_{off}$ | Reference |
|---|---|---|---|---|---|
| tetracyanoquinodimethane | single crystal | OMBE | $10^{-4}$ | NR | 90 |
| ethynyl-linked alternating anthracene/ fluorene copolymer | polymer film | Sol. Proc. | $6 \times 10^{-4}$ | $10^4$ | 86 |
| hexa-peri-hexabenzocoronene (HBC-$C_{12}$) | liquid crystal | zone casting | $5 \times 10^{-4}$ | NR | 87 |
| poly(3-alkylthiophene) | polymer film | friction-transfer | $7.4 \times 10^{-3}$ | NR | 88 |
| cyclohexyl-substituted quaterthiophene | thin film | Sol. Proc. | 0.02 | NR | 98 |
| poly(9,9-dioctylfluorene-co-bithiophene) | polymer film | Sol. Proc./LC rubbing | 0.02 | NR | 89 |
| $C_{60}$ | single crystal | OMBE | 0.03 | NR | 90 |
| poly(9,9-dioctylfluorene-co-bithiophene) | polymer film | friction-transfer | 0.04 | NR | 91 |
| α-quinquethiophene | thin film | OMBE | 0.05 | $>10^5$ | 92 |
| 5,5'-bis(4-octyloxyphenyl)bithiophene | oligomer | Sol. Proc. | 0.05 | NR | 93 |
| α-sexithiophene | thin film | OMBE | 0.08 | $>10^5$ | 92 |
| 2,6-Bis[2-(4-pentylphenyl)vinyl]anthracene | thin film | OMBE | 0.1 | $10^6 - 10^7$ | 94 |
| Copper phthalocyanine | single crystal | Sol. Proc./ OMBE | 0.1 | NR | 95 |
| Poly(3-hexylthiophene) | polymer | Sol. Proc. | 0.1 | $>10^6$ | 96 |
| Perlfuorpentacene | thin film | OMBE | 0.11 | $10^6$ | 97 |
| trimethylsilyl-substituted quaterthiophene | thin film | Sol. Proc. | 0.11 | NR | 98 |
| α-septithiophene | thin film | OMBE | 0.13 | $>10^5$ | 92 |
| copper hexadecafluorophtalocyanine | single crystal | Sol. Proc./ OMBE | 0.2 | NR | 95 |
| Tetracene | thin film | OMBE | 0.23 | $10^5$ | 99 |
| Pentacene | single crystal | Sol. Proc. | 0.4 | $10^6$ | 100 |
| Pentacene | thin film | OMBE | 0.7 | >100 | 101 |
| Tetracene | single crystal | OMBE | 1.0 | NR | 102 |
| Pentacene | thin film on chemically modified substrate | OMBE | 1.2 | $10^5 - 10^7$ | 103 |
| Rubrene | thin film | OMBE | 2.4 | $10^7$ | 104 |
| Pentacene | thin film with polymer dielectric | OMBE | 3 | $10^5$ | 105 |
| Rubrene | single crystal | OMBE | 15.4 | NR | 106 |

Table 1: Collection of organic semiconductor based devices, their method of manufacture, and their electronic properties.

## Section 4
## Organic Vapor Liquid Solid Deposition

This thesis research builds upon a method developed by Wilkinson *et al.*[107] that combines concepts from OMBE with solution-processing and utilizes the orientational control mechanism of liquid crystal imprinting. Organic Vapor Liquid Solid (OVLS) deposition is a vapor-phase deposition technique which grows organic films in a thin layer of thermotropic liquid crystal (LC) solvent, applied by spin coating onto a rubbed polyimide alignment layer, as represented in figure 16.[107] OVLS provides an organized fluid environment in which organic molecular crystals nucleate and grow. The technique produces large crystals, enables control over crystallographic orientation, morphology, and size, and is carried out under near ambient conditions. OVLS is therefore compatible with a variety of substrates and organic materials. Due to the increased diffusion of molecules in a liquid environment, OVLS can grow crystals under near ambient temperatures to sizes only possible

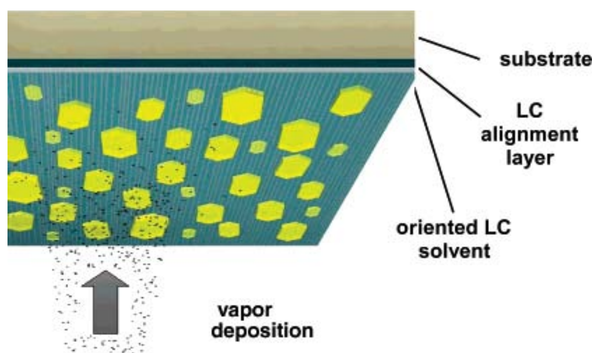


Figure 16: OVLS deposition schematic. Adapted from [107]

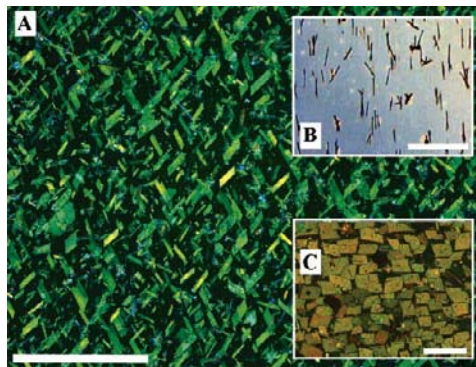


Figure 17: Optical micrographs of tetracene films on Si(100) coated with rubbed PVA and A) LC ZLI-3417 B) LC E7 C) LC MBBA. All scale bars are 100 μm. Adapted from [107]

at high temperatures for bare surface growth. OVLS has shown an ability to grow highly ordered films of the organic semiconductors tetracene, pentacene and anthracene, and should be applicable to a wide range of materials.

The OLVS method affords additional controllability with the selection of the solvent. The ability to tune growth characteristics is a long-recognized advantage of solution-phase crystallization via chemical interactions with the solvent.[108] Shown in figure 17 are some differing crystal morphologies of tetracene, ranging from platelets to needles to compact lozenges based solely on the growth medium. It is therefore possible to select a desired crystal morphology by choice of growth medium.

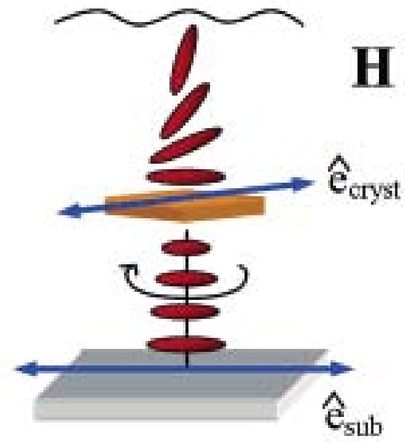

Figure 18: orientational mechanism of LC imprinting. Adapted from [107]

Orientation of organic semiconductor crystals in OVLS differs from the other approaches discussed above due to the fact that the crystals are floating freely in the LC solvent. The orientational mechanism arises from a mechanical torque applied to misaligned crystals resulting from surface anchoring and curvature elasticity, as illustrated in figure 18.[107] To quantify the degree of order, an order parameter was calculated by equation 2:

(2) $$s = < cos2\theta >$$

Where θ is the angle between a specific axis ([110] for tetracene) of a crystal and the mean orientation of all crystals within the film and the brackets represent an

average over all observations. The order parameter is zero for completely dissordered films and 1 for completely ordered films. Films grown by the OVLS method obtained *s* values from 0.9 to 0.99, proving the OVLS mechanism as a powerful tool for organic semiconductor thin film alginment.[107]

Previous research in the Patrick group introduced the OVLS method and demonstrated its promise in a few model systems. However, this work also revealed a number of shortcomings associated with the method, including poor reproducibility and the need for unacceptably long deposition times (on the scale 14h to 1 day). If these limitations could be overcome, OVLS would allow for the large scale production of organic semiconductor devices. Also, OVLS could be used to deposit and grow films of any material which satisfied the requirements for the system (slightly soluble, air stable, readily sublimes under ambient pressure), not exclusively organic semiconductors.

To improve upon the OVLS method, two organic semiconductors were studied in this work: tetracene and anthracene. These compounds are linear fused-ring organic semiconductors from the archetypal polyacene family, shown in figure 19.[109]

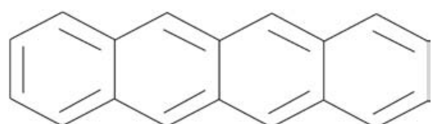


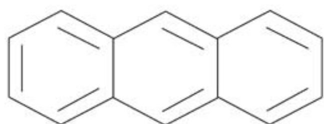


Figure 19: structures of tetracene and anthracene

Tetracene was chosen due to reasonably high chemical stability, the fact that it can be readily sublimated, and its favorable electronic properties, making it a good candidate for a variety of applications.[110,111,112,113,114,115] Anthracene was also studied as it is more

chemically stable and grows larger crystals. Also, since anthracene is a bi-product of petroleum distillation, it benefits from a 100 fold decrease in cost.

# Section 5
# Goals of Thesis

Interest in using organic semiconductors in applications such as large area displays, photovoltaic devices, and RFID tags stems in part from their prospects for enabling significantly reduced manufacturing costs compared to traditional inorganic semiconductors. However many of the best performing prototype devices produced so far have involved expensive or time-consuming fabrication methods, such as the use of single crystals or thin films deposited under high vacuum conditions. This thesis examines a new approach for growing low molecular weight organic crystalline films at ambient conditions based on an organic vapor-liquid-solid growth (OVLS) mechanism using thermotropic nematic liquid crystal (LC) solvents.

In this research I have introduced a laminar flow of an inert carrier to increase deposition rate as well as to decrease overall aggregation times, as well as vapor phase particle charging, which increases deposition rate even further. I have studied the effects of carrier gas flow rate, sublimation rate, carrier gas composition, particle charging, and plasma environment and found that a delicate balance between flow rate and sublimation rate must be maintained, while carrier gas composition and plasma environment affect both chemical purity and deposition dynamics. Particle charging was shown to not only increase the rate of deposition, but also to allow for an additional control over the path of the particle beam.

## Chapter One References


**1** W. Shockley, G. L. Pearson, *Physical Review* **1948**, 22.

**2** C. K. Chiang, C. R Fincher, Y. W. Park Jr., A. J. Heeger, H. Shirakawa, E. J. Louis, S. C Gau, A. G. MacDiarmid, *Phys. Rev. Lett.* **1977**, 39.

**3** L. Shuhong, W. M. Wang, A. L. Briseno, S. C. B. Mannsfeld, Z. Bao, *Advanced Materials* **2009**, 21.

**4** S. Takao, P. Bholanathm, H. Jia, H. E. Katz, *MRS Bulletin* **2008**, 33.

**5** Drury, C. J.; Mustaers, C. M. J.; Hart, C. M.; Matters, M.; de Leeuw, D. M. *Appl Phys. Lett.*, **1998**, 73.

**6** F. Garnier, R. Hajlaoui, A. Yasser, *Science*, **1994**, 265.

**7** P. F. Baude, D. A. Ender, M. A. Haase, T. W. Kelley, D. V. Mures, S. D. Theiss, *Appl. Phys. Lett.* **2003**, 82.

**8** T. Martenz, J D'Haen, T. Munters, L. Goris, Z. Beelen, J. Manca, M. D'Oliesaeger, D. Vanderzande, L Se Schepper, R. Andriessen, *Mat. Res. Soc. Symposium Porceedings* **2002**, 725.

**9** M. Ramos, T. Rispens, C. Hummelen, J. Janes, *Synth. Met.* **2001**, 119.

**10** J. M. Leger, D. G. Patel, D. B. Rodovsky, G. P. Bartholomew, *Adv. Funct. Mat.* **2008**, 18.

**11** W. Tang, S. Van Slyke, *Appl Phys Lett.* **1987**, 51.

**12** H. Burroughes, C. Bradley, R. Brown, N. Marks, K. Mackey, H. Friend, L. Burns, B. Holmes, *Nature* **1990**, 347.

**13** T. Sekitani, H. Nakajima, H. Maeda, T. Fukushima, T. Aida, K. Hata, T. Someya, *Nature* **2009**, 8.

**14** S. Sepeai, M. M. Salleh, M. Yahaya, A. A. Umar, *Thin Solid Films* **2009**, 517.

**15** Katz H. E., Bao, Z., *J. Phys. Chem.* **2000**, 104.

**16** R. A. Gaudiana, Abstracts of Papers, 238th ACS National Meeting, Washington, DC, United States, August 16-20, 2009

**17** M. Gross, *Chemistry in Britain* **2001**, 31.

**18** A. Rogers, Z. Bao, K. Baldwin, A. Dodabalapur, B. Crone, V. R. Raju, V. Kuck, H. Katz, K. Amundson, J. Ewing, P. Drzaic, *Proc. Natl. Acad. Sci. USA* **2001**, 98.

**19** G. H. Gelinck, H. E. A. Huitema, E. Van Veenendaal, E. Cantatore, L. Schrijnemakers, J. B. P. H. van der Putten, T. C. T. Geuns,M. Beenhakkers, J. B. Giesbers, B. H. Huisman, E. J. Meijer, E. M. Benito, F. J. Touwslager, A. W. Marsman, B. J. E. van Rens, D. M. De Leeuw, *Nat. Mater.* **2004**, 3.

**20** Z. T. Zhu, J. T. Mason, R. Dieckmann, G. G. Malliaras, *Appl. Phys. Lett.* **2002**, 81.

**21** L. Torsi, A. Dodabalapur, *Anal. Chem.* **2005**, 77.

**22** K. Hutchinson, G. Srdanov, R. Menon, J. Gabriel, B Knight, F. Wudl, *Synth. Mat.*, **1997**, 86.

**23** J. Locklin, Z. Bao, *Anal. Bioanal. Chem.* **2006**, 384.

**24** D. Voss, *Nature* **2000**, 407.

**25** R. Rotzoll, S. Mohapatra, V. Olariu, R. Wenz, M. Grigas, K. Dimmler, O. Shchekin, A. Dodabalapur, *Appl. Phys. Lett.* **2006**, 88.

**26** D. A. Pardo, G. E. Jabbour, N. Peyghambarian, *Adv. Mater.* **2000**, 12.

**27** Y. C. Cheung, D. L. Trosi, A. *Phys. Chem. Chem. Phys*, **2008**, 10.

**28** J. Locklin, M. E. Roberts, S. C. B. Mannsfeld, Z. Bao, J. Macromol. *Sci. Polym. Rev.* **2006**, 46.

**29** D. J. Gundlach, Y. Y. Lin, T. N. Jackson, S. F. Nelson, D. G. Schlom, *IEEE Electron Device Lett.* **1997**, 18.

**30** H. Sirringhaus, P. J. Brown, R. H. Friend, M. M. Nielsen, K. Bechgaard, B. M. W. Langeveld-Voss, A. J. H. Spiering, R. A. J. Janssen, E. W. Meijer, P. Herwig, D. M. de Leeuw, *Nature* **1999**, 401.

**31** M. L. Tang, T. Okamoto, Z. N. Bao, *J. Am. Chem. Soc.* **2006**, 128.

**32** M. L. Tang, M. E. Roberts, J. J. Locklin, M. M. Ling, H. Meng, Z. N. Bao, *Chem. Mater.* **2006**, 18.

**33** A. Sung, M. M. Ling, M. L. Tang, Z. A. Bao, J. Locklin, *Chem. Mater.* **2007**, 19.

**34** M. Ando, M. Kawasaki, S. Imazeki, H. Sasaki, T. Kamata, *Appl. Phys. Lett.* **2004**, 85.

**35** S. Liu, W. M. Wang, A. L. Briseno, S. C. B. Mannsfeld, and Z. Bao, Controlled deposition of Crystalline organic semiconductors for field-effect-transisitor applications, *Advanced Materials* **2009**, 21.

**36** Silinsh, E. A.; Capek, V. Charge Carrier Interaction with Local Lattice Environment. *Organic Molecular Crystals: Interaction, Localization and Transport Phenomena*, 1; American Institute of Physics: New York, 1994; 83-141

**37** J. Cornil, J. Ph. Calbert, J. L. Brédas, *J. am. Chem. Soc.* **2001**, 123

**38** S. Haas, F. Stassen, G. Schuck, K. P. Pernstich, D. J.l Gundlach, B. Batlogg, *Phys. Rev. B* **2007**, 76.

**39** C. D. Dimitrakopoulos and D. J. Mascaro, *IBM J. Res. Devel.* **2001**, 45.

40 T.P. Nguyen, *Mat. Sci. in Sem. Process.*, **2006**, 9, 1-3

**41** O. D. Jurchescu, J. Baas, T. T. m. Palstra, *Appl. Phys. Lett.* **2004**, 84.

**42** J. E. Anthony, J. S. Brooks, D. L. Eaton, S. R. Parkin, *JACS* **2001**, 123.

**43** V. C. Sundar, J. Zaumseil, V. Podzorov, E. Menard, R. L. Willett, T. Someya, M. E. Gershenson, J. A. Rogers, *Science* **2004**, *303*.

**44** R. Zeis, C. Besnard, T. Siegrist, C. Schlockermann, X. Chi, C. Kloc, *Chem. Mater.* **2006,** 18.

**45** Gundlach, *Appl.Phys. Lett.* **1999** 74.

**46** A. L. Briseno, S. C. B. Mannsfeld, M. M. Ling, S. H. Liu, R. J. Tseng, C. Reese, M. E. Roberts, Y. Yang, F. Wudl, Z. N. Bao, *Nature* **2006**, 444.

**48** O. S. Liu, C. Reese, M. E. Roberts, Z. Bao, *Adv. Funct. Mater.* **2007**, 17.

**49** V. C. Sundar, J. Zaumseil, V. Podzorov, E.Menard, R. L. Willett, T. Someya, M. E. Gershenson, J. A. Rogers, *Science* **2004**, 303.

**50** R. Li W. Hu, Y. Liu, D. Zhu, *Accounts of Chem. Res.*, **2009,** 12.

**51** M. L. Chabinyc, W. S. Wong, A. Salleo, K. E. Paul, R. A. Street, *Appl. Phys. Lett.* **2002**, 81.

**52** K. S. Lee, G. B. Blanchet, F. Gao, Y. L. Loo, *Appl. Phys. Lett.* **2005**, 86.

**53** A. Chandekar, J. E. Whitten, *Appl. Phys. Lett.* **2007**, 91.

**54** A. L. Briseno, J. Aizenberg, Y. J. Han, R. A. Penkala, H. Moon, A. J. Lovinger, C. Kloc, Z. A. Bao, *J. Am. Chem. Soc.* **2005**, 127.

**55** S. H. Liu, W. C. M. Wang, S. C. B.Mannsfeld, J. Locklin, P. Erk, M. Gomez, F. Richter, Z. N. Bao, *Langmuir* **2007**, 23.

**56** W. Pisula, A. Menon, M. Stepputat, I. Lieberwirth, U. Kolb, A. Tracz, H. Sirringhaus, T. Pakula, K. Mullen, *Adv. Mater.* **2005**, 17.

**57** H. A. Becerril, M. E. Roberts, Z. Liu, J. Locklin, Z. Bao, *Adv. Mater.* **2008**, 20.

**58** C. Kloc, P. G. Simpkins, T. Siegrist, R. A. Laudise, *J. Cryst. Growth* **1997**, 182.

**59** Z. N. Bao, *Adv. Mater.* 2000, 12.

**60** C. Reese, Z. N. Bao, *Mater. Today* **2007**, 10.

**61** H. Klauk, D. J. Gundlach, J. A. Nichols, T. N. Jackson, IEEE Trans. *Electron Devices* **1999**, 46.

**62** X. L. Chen, A. J. Lovinger, Z. N. Bao, J. Sapjeta, *Chem. Mater.* **2001**, 13.

**63** H. Klauk, M. Halik, U. Zschieschang, G. Schmid, W. Radlik, W. Weber, *J. Appl. Phys.* **2002**, 92.

**64** Q. X. Tang, H. X. Li, Y. B. Song, W. Xu, W. P. Hu, L. Jiang, Y. Q. Liu, X. K. Wang, D. B. Zhu, *Adv. Mater.* **2006**, 18.

**65** Z. Aliadib, K. Davidson, H. Nooshin, R. H. Tredgold, *Thin Solid Films* **1991**, 201.

**66** I. O. Shklyarevskiy, P. Jonkheijm, N. Stutzmann, D. Wasserberg, H. J. Wondergem, P. C. M. Christianen, A. P. H. J. Schenning, D. M. de Leeuw, Z. Tomovic, J. S. Wu, K. Mullen, J. C. Maan, *J. Am. Chem. Soc.* **2005**, 127.

**67** M. I. Boamfa, K. Viertler, A. Wewerka, F. Stelzer, P. C. M. Christianen, J. C. Maan, *Phys. Rev. Lett.* **2003**, 90.

**68** J. Oguma, R. Kawamoto, H. Goto, K. Itoh, K. Akagi, *Synth. Met.* **2001**, 119.

**69** I. O. Shklyarevskiy, P. C. M. Christianen, J. C. Maan, A. P. H. J. Schenning, E. W. Meijer, O. Henze, W. J. Feast, *Mol. Cryst. Liq. Cryst.* **2004**, 410.

**70** I. O. Shklyarevskiy, P. Jonkheijm, P. C. M. Christianen, A. P. H. J. Schenning, A. Del Guerzo, J. P. Desvergne, E. W. Meijer, J. C. Maan, *Langmuir* **2005**, 21.

**71** M. Prelipceanu, O. G. Tudose, O. S. Prelipceanu, S. Schrader, K. Grytsenko, *Mater. Sci. Semicond. Proc.* **2007**, 10.

**72** M. L. Swiggers, G. Xia, J. D. Slinker, A. A. Gorodetsky, G. G.Malliaras, R. L. Headrick, B. T. Weslowski, R. N. Shashidhar, C. S. Dulcey, *Appl. Phys. Lett.* **2001**, 79.

**73** A. J. J. M. van Breemen, P. T. Herwig, C. H. T. Chlon, J. Sweelssen, H. F. M. Schoo, S. Setayesh, W. M. Hardeman, C. A.Martin, D. M. de Leeuw, J. J. P. Valeton, C. W. M. Bastiaansen, D. J. Broer, A. R. Popa-Merticaru, S. C. J. Meskers, *J. Am. Chem. Soc.* **2006**, 128.

**74** L. Kinder, J. Kanicki, P. Petroff, *Synth. Met.* **2004**, 146.

**75** W. Y. Chou, H. L. Cheng, *Adv. Funct. Mater.* **2004**, 14.

**76** S. H. Jin, H. U. Seo, D. H. Nam, W. S. Shin, J. H. Choi, U. C. Yoon, J. W. Lee, J. G. Song, D. M. Shin, Y. S. Gal, *J. Mater. Chem.* **2005**, 15.

**77** A. G. Dyadyusha, T. Y. Marusii, Y. A. Reznikov, A. I. Khizhnyak, V. Y. Reshetnyak, *JETP Lett.* **1992**, 56.

**78** M. Schadt, K. Schmitt, V. Kozinkov, V. Chigrinov, *Jpn. J. Appl. Phys.* **1992**, 31.

**79** J. H. Kim, Y. Shi, S. Kumar, S. D. Lee, *Appl. Phys. Lett.* **1997**, 71.

**80** M. Nishikawa, B. Taheri, J. L. West, *Appl. Phys. Lett.* **1998**, 72.

**81** S. E. Fritz, T. W. Kelley, C. D. Frisbie, *J. Phys. Chem. B* **2005**, 109.

**82** T. Fujiwara, J. Locklin, Z. N. Bao, *Appl. Phys. Lett.* **2007**, 90.

**83** M. Voigt, S. Dorsfeld, A. Volz, M. Sokolowski, *Phys. Rev. Lett.* **2003**, 91.

**84** M. Shtein, H. Gossenberger, J. B. Benziger, S. R. Forrest, *J. Appl. Phys.*, **2001**, 89.

**85** M Sthein, P Peumans, J. B. Benziger, S. R. Forrest, *J Apply. Phys.*, **2003**, 93.

**86** J. U. Ju, D. S. Chung, S. O. Kim, C. E. Park, Y-h. Kim, S-k. Kwon, *J. Pol. Sci. A: Pol. Chem.* **2009** 47.

**87** W. Pisula, A. Menon, M. Stepputat, I. Lieberwirth, U. Kolb, A. Tracz, H. Sirringhaus, T. Pakula, K. Mullen, *Adv. Mater.* **2005**, 17.

**88** S. Nagamatsu, N. Tanigaki, Y. Yoshida, W. Takashima, K. Yase, K. Kaneto, *Synth. Met.* **2003**, 137.

**89** H. Sirringhaus, R. J. Wilson, R. H. Friend, M. Inbasekaran, W. Wu, E. P. Woo, M. Grell, D. D. C. Bradley, *Appl. Phys. Lett.* **2000**, 77.

**90** A. L. Briseno, J. Aizenberg, Y. J. Han, R. A. Penkala, H. Moon, A. J. Lovinger, C. Kloc, Z. A. Bao, *J. Am. Chem. Soc.* **2005**, 127.

**91** S. P. Li, C. J. Newsome, D. M. Russell, T. Kugler, M. Ishida, T. Shimoda, *Appl. Phys. Lett.* **2005**, 87.

**92** S. Nagamatsu, K. Kaneto, R. Azumi, M. Matsumoto, Y. Yoshida, K. Yase, *J. Phys. Chem. B*, **2005**, 109.

**93** T. Fujiwara, J. Locklin, Z. N. Bao, *Appl. Phys. Lett.* **2007**, 90.

**94** H. Meng, F. Sun, M. B. Goldfinger, F. Gao, D. J. Londono, W. J. Marshal, G. S. Blackman, K. D. Dobbs, D. E. Keys, *JACS*, **2006**, 128.

**95** Q. X. Tang, H. X. Li, Y. B. Song, W. Xu, W. P. Hu, L. Jiang, Y. Q. Liu, X. K. Wang, D. B. Zhu, *Adv. Mater.* **2006**, 18.

**96** H. Sirringhaus, N. tessler, R. H. Friends, *Science*, **1998**, 280.

**97** Y. Sakamoto, T. Suzuki, M. Kobayashi, Y. Gao, Y. Fukai, Y. Inoue, F. Sato, S. Tokito, *JACS* **2004**, 126.

**98** S. C. B. Mannsfeld, A. Sharei, S. Liu, M. E. Roberts, Z. Bao, *Adv. Mater.* **2008**, 20.

**99** J. M. Choi, K. Lee, D. K. Hwang, J. H. Park, E. Kim, G. Im, *Electrochemical and Solid State Lett.* **2006**, 9.

**100** Yasuo Kimura* and Michio Niwano, *Langmuir* **2009**, 25.

**101** Y. Y. Lin, D. J. Gundlach, S. F. Nelson, T. N. Jackson, *IEEE Electron Device Letters* **1997**, 18.

**102** P. Jens, N. Jens, T. A. Kuma, *Mater. Res. Soc. Symp. Proc.* **2005**, 871.

**103** Y. Jang, W. H. Lee, Y. D. Park, D. Kwak, J. H Cho, *Appl. Phys. Lett,* **2009**, 94.

**104** C. Yi, S. Ishiang, *Appl. Phys. Lett*, **2009**, 94.

**105** H. Klauk, M. Halik, U. Zschieschang, G. Schmid, W. radik, J. Appl. Phys. **2002**, 92.

**106** V. Podzorov1 *, E. Menard2, A. Borissov1, V. Kiryukhin1, J. A. Rogers2, and M. E. Gershenson, *Phys. Rev. Lett.* **2004**, 93.

**107** F. S. Wilkinson, R. F. Norwood, J. M. McLellan, L. Rhy Lawson, D. L. Patrick, *JACS* 2006, 128.

**108** *Crystals and Crystal Growing*; Holden, A., Singer, P., Eds.; Anchor Books- Doubleday: New York, 1960.

**109** R. W. I. de Boer, T. M. Klapwijk, A. F.Morpurgo, *Appl. Phys. Lett.* **2003**, 83.

**110** R.W.I. de Boer, A. F. Morpurgo, T. M. Klapwijk, *Appl. Phys. Lett.* **2003**, 83.

**111** P. Jens, N. Jens, T. A. Kuma, *Mater. Res. Soc. Symp. Proc.*, **2005**, 871.

**112** J. M. Choi, K. Lee, D. K. Hwang, J. H. Park, E. Kim, G. Im, *Electrochemical and Solid State Lett.*, **2006**, 9.

**113** M. Pope, C. E. Swenberg, in *Electronic Processes in Organic Crystal and Polymers*, 2nd ed., Oxford university press, Oxford, UK **1999**

**114** S. H. Lim, T. G. Bjorklund, F. C. Spano, C. J. Barden, *Phys. Rev. Lett.* **2004**, 92.

**115 N.** Geacintov, M. Pope, H. Kallmann, *J. Chem. Phys.* **1966**, 45.

# Chapter Two

## Ambient Axisymmetric-Spray

As described in chapter one, the most widely-used method for organic semiconductor thin film growth is organic molecular beam epitaxy (OMBE). Although OMBE is capable of producing high quality, high performance thin films, it has several drawbacks. Presented in this chapter is a new method for growing organic semiconductor thin films by Ambient Axisymmetric-Spray (AAS) deposition. The AAS chamber is similar to typical OMBE chambers with one important difference: deposition is carried out under near ambient pressure at room temperature, thereby removing the need for the costly equipment and lengthy procedures required for working in a high vacuum environment. The AAS chamber consists of two regions we term the mixing region and the deposition region. In the mixing region, a resistive heating element, composed of Omega Engineering Nicrome 80 wire wrapped around a Macor™ receptacle with an Omega Engineering thermocouple, is controlled by an Omega Engineering CN4321 temperature control unit. The heating element holds a graphite crucible which heats an organic semiconductor promoting controlled sublimation. The resultant vapor combines with a carrier gas fed through the side of the mixing region producing a dilute gas phase mixture, which exits the mixing region through a nozzle (VWR International disposable pipet tip 1-220uL cut to varying nozzle diameters) and enters the deposition region. The mechanics of the deposition region are complex, and will be explained in greater detail later. The system is enclosed by a 15.24 cm diameter acrylic cylinder with 1.27 cm thick walls and a 1.27

cm thick removable acrylic lid. The base of the AAS chamber is aluminum and contains a channel in which water is continuously flushed to maintain ambient temperature. All manufactured parts of the AAS chamber were built at the Western Washington University machine shop.

The AAS system affords control over organic flux rate, organic vapor phase concentration, deposition rate, and diffusion of adsorbed species. Additionally, the cost of building an AAS system is significantly lower than a high vacuum OMBE chamber (on the order of one quarter). A schematic representation of the AAS chamber is presented as figure 2-1 with a list of control parameters presented in table 2.

Table 2: Experimental parameters associated with the AAS method.

| Parameter | Abbreviation |
| --- | --- |
| **Crucible temperature** | $T_{cruc}$ |
| **Carrier gas flow rate** | $u_0$ |
| **Substrate to nozzle distance** | z* |
| **Nozzle radius** | $r_{nozzle}$ |
| **Radial distance from center of nozzle** | $r_{dep}$ |
| **Internal pressure** | P |
| **Substrate temperature** | $T_{sub}$ |
| **Deposition time** | $t_{dep}$ |
| **Mass of organic powder** | $M_{os}$ |

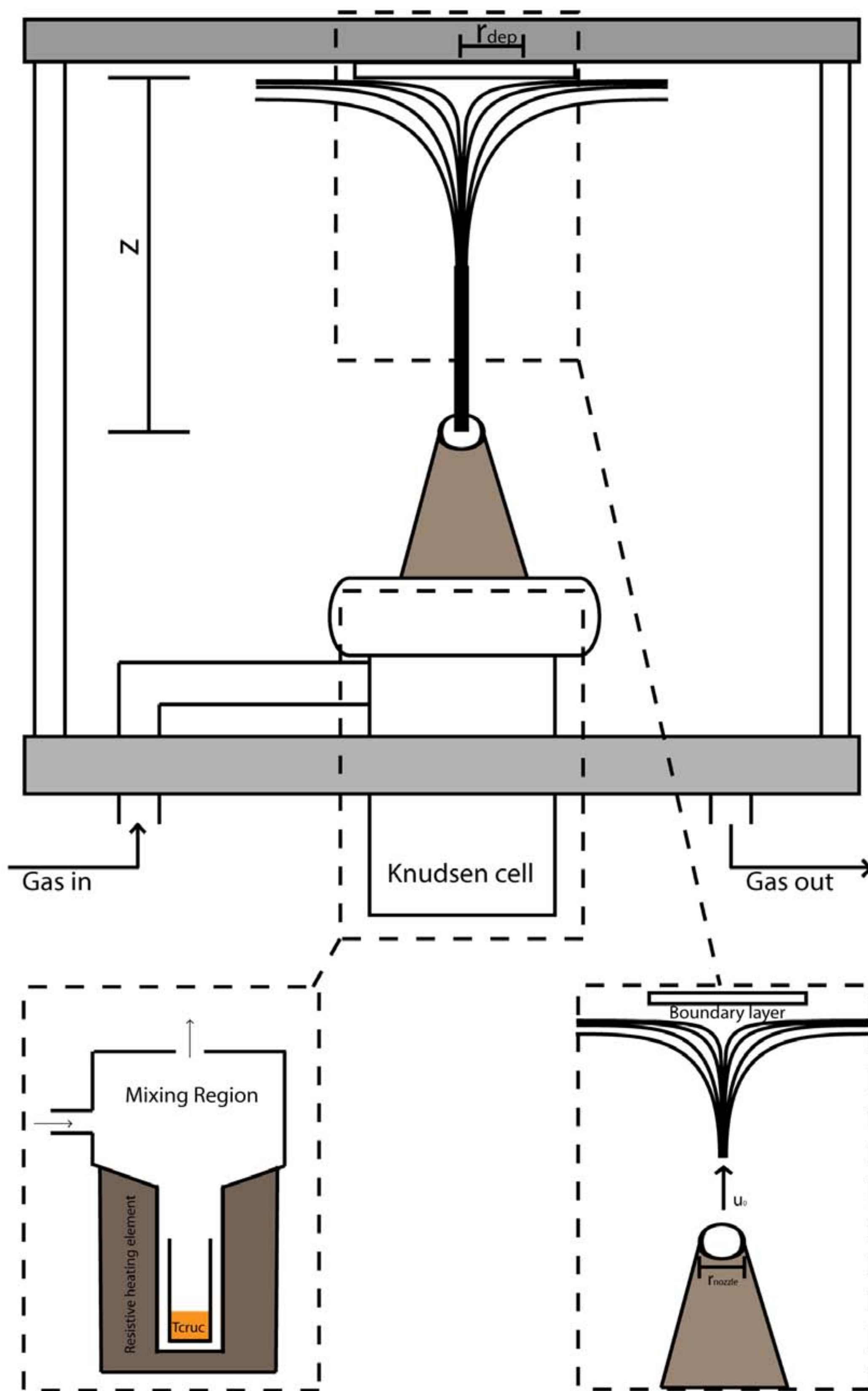


Figure 2-1: Schematic representation of the AAS chamber.

The AAS chamber was designed to accomplish three goals. First, to increase the rate of deposition so organic semiconductor thin films could be grown in minutes instead of hours. Second, to design a system with a high degree of reproducibility. Third, to reduce or eliminate one of the issues associated with standard pressure OMBE, namely, vapor phase aggregation. Due to the ability of OVLS substrates to dissolve particles of organic semiconductors, a small degree of vapor phase aggregation is acceptable.

The two regions of the AAS system must be modeled independently due to their unique hydrodynamics. In the mixing region, two concurrent mechanisms are considered: sublimation and vapor phase aggregation. Condensation in the mixing region is considered negligible for the AAS system since the sublimation event occurs in a graphite crucible heated above the sublimation temperature. Therefore, sublimation occurs at a rate S calculated by equation 2-1:[1]

(2-1) $$S \propto A \frac{{T_{cruc}}^{1/2}}{P} e^{-\Delta H_{sub}/RT_{cruc}}$$

Where $T_{cruc}$ (K) is the crucible temperature, $P$ (Pa) is the pressure of the system, $\Delta H_{sub}$ (J mol$^{-1}$) is the heat of sublimation, and $A$ (m$^2$) is the total area of sublimate.

## Section 2
## Particle Aggregation Model

In standard OMBE, the incident particle flux must consist of primarily monomers, since larger particles on a substrate will diffuse at low rates (if at all), resulting in poor quality films.[2] This situation leads to small grain sizes, a highly undesirable growth mode for semiconductor films, as discussed in chapter one. In addition, crystals grown in the vapor phase can have a large variety of complex morphologies, making controlled studies impossible. Since our system involves atmospheric pressure and the chamber is held at room temperature, vapor phase aggregation will occur and thus lead to a broadened incident particle size distribution. Presented here is a coarse approximation for cluster growth due to vapor phase aggregation. Following the work of Elimelech *et al.*, we calculate particle size distributions based upon our experimental conditions.[3] Colliding clusters will aggregate based upon an aggregation probability, assumed here to be unity (i.e. every collision results in particle fusion), and so aggregation of vapor phase particles will occur based solely upon their probability of collision. The collisional half life, or the time it takes for half of the existing vapor phase particles to collide (L molecules$^{-1}$ sec$^{-1}$) is calculated using equation 2-2:

(2-2)
$$\tau \approx \frac{1}{k_a n_0}$$

Where $k_a$ (unitless) is the collision kernel and $n_0$ (molecules m$^{-3}$) is the initial concentration of particles. The collision kernel (a unitless scaling constant) can be calculated using equation 2-3:

(2-3) $$k_a = \frac{8k_B T A_p}{3\mu D}$$

Where $A_p$ ($m^2$) is the cross sectional area of a particle of given size, $k_B$ ($J\ K^{-1}$) is the Boltzmann constant, $T$ (K) is the temperature of the particles, $D$ ($m^2\ sec^{-1}$) is the diffusion coefficient, and $\mu$ ($Kg\ m^{-1}\ sec^{-1}$) is the dynamic viscosity of the carrier gas. Assuming that the cross sectional area and the diffusivity scale to a value of 1 independent of particle size allows for equation 2-3 to simplify to 2-4:

(2-4) $$k_a \approx \frac{8k_B T}{3\mu}$$

We now make the following assumptions so that the model can produce analytical solutions:

1) When particles collide, their volumes are additive.
2) Diffusion is the dominant driving force for collisions.
3) Particle collisions occur exclusively between particles of the same size.

The third assumption is only valid for very short timescales with a relatively small number of collision events (when $t/\tau \leq 200$).

A cluster size distribution can now be approximated with equation 2-5:

(2-5) $$n_k = \frac{n_0 (t/\tau)^{k-1}}{1+(t/\tau)^{k+1}}$$

Where $t$ (s) is the time of flight (or amount of time the particles are allowed to aggregate), $k$ (molecules) is the size of a cluster and $n_k$ (clusters $m^{-3}$) is the concentration of clusters of size $k$. The most important parameters to investigate are initial particle concentration and aggregation time, as these are the main variables used to manipulate the AAS system. Aggregation time is reported as the time of

flight, calculated by the distance that a particle must travel to reach the substrate divided by the gas flow rate assuming that the dynamics of a particle in the gas stream is independent of its position in the chamber. Figure 2-2A plots cluster size distribution histograms for two different values for the time of flight (0.02 s and 0.2 s) representing the experimentally determined bounds of the system using an initial monomer concentration $n_0 = 10^{18}$ molecules $m^{-3}$ (The experimental bounds were found by performing a series of experiments at differing flow rates to find the lowest and highest values tolerable. These flow rates were then used to calculate time of flights based on the distance between the solid powder and the surface of the substrate). As can be seen, particle size distribution shifts rapidly towards larger particles as the aggregation time increases. In fact, for a half of a second increase in aggregation time, the particle size distribution can shift from particles under 23 molecules to those in excess of 100 molecules.

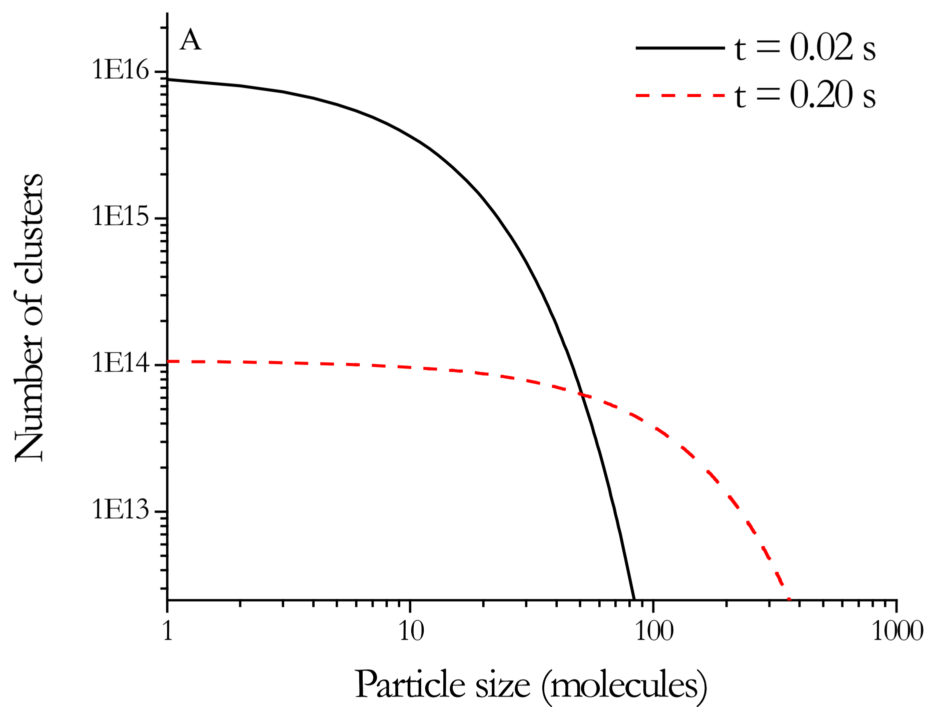


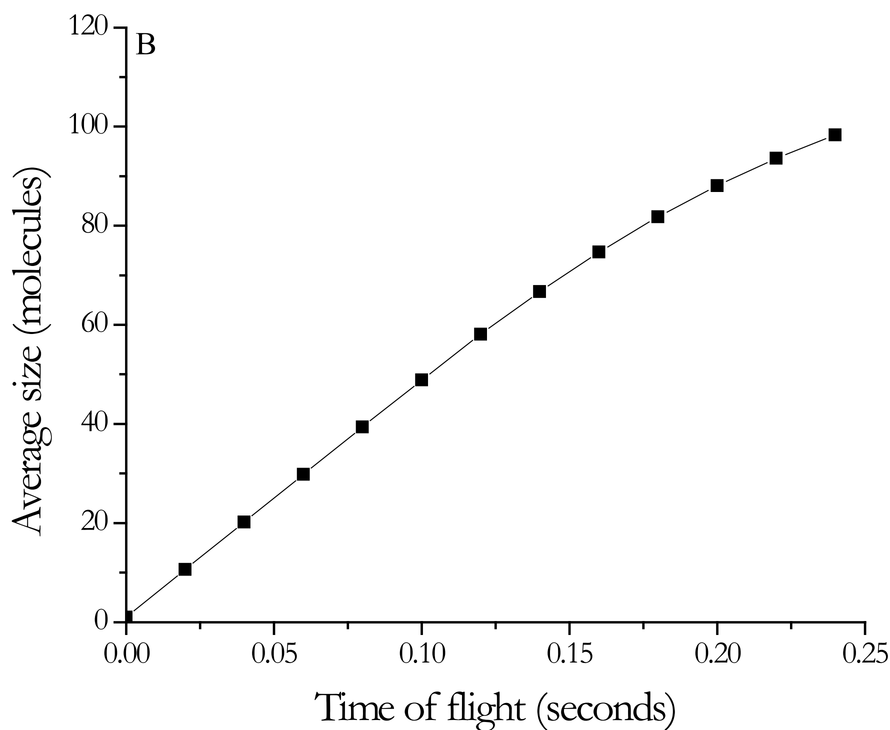


Figure 2-2: A) Theoretical particle size distribution as a function of time of flight. B) Theoretical average vapor phase cluster size versus time of flight

As the theoretical distribution of sizes shifts, so does the theoretical average particle size, illustrated in figure 2-2B, showing a linear relationship between aggregation time and average size which begins to tail off at longer times. It is interesting to note that under these conditions for every tenth of a second increase, the average particle size increases by ~50 molecules.

As stated previously, the ideal particle flux consists primarily of monomers. However, due to the increased number of collision events resulting from the use of an ambient pressure setup, the concentration of monomers in the AAS system will always be low, and will decrease exponentially with respect to aggregation time as shown in figure 2-3. For example the monomer concentration is predicted to drop

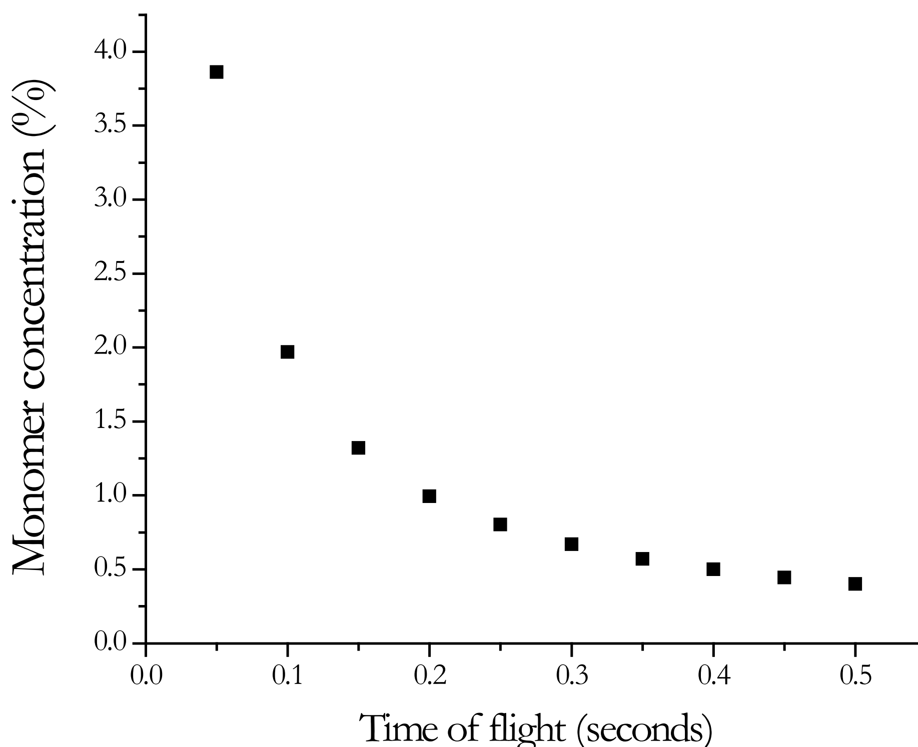


Figure 2-3: Theoretical representation of the exponential relationship of time of flight on monomer concentration. This relationship must conclude that monomer arrival is highly improbable under these experimental conditions.

from 100% to just 3.6% after the first 0.05s. Therefore, according to this model, in order for there to be a reasonable concentration of monomers, the time of flight must be on the order of milliseconds.

As is clear from the preceding discussions, initial vapor phase particle concentration ($n_0$) will strongly affect the particle size distribution. Indeed, it has been shown experimentally that high particle concentration can lead to unfavorable results (presented below). In order to estimate $n_0$, the AAS chamber was run for 24 hours, and the loss of mass from the crucible was measured. Based on the mass of tetracene sublimated (4.7 mg), and the gas consumed at standard run parameters, (~5 L) we estimate $n_0 \sim 10^{17}$-$10^{19}$ molecules $L^{-1}$ under typical conditions. Unfortunately,

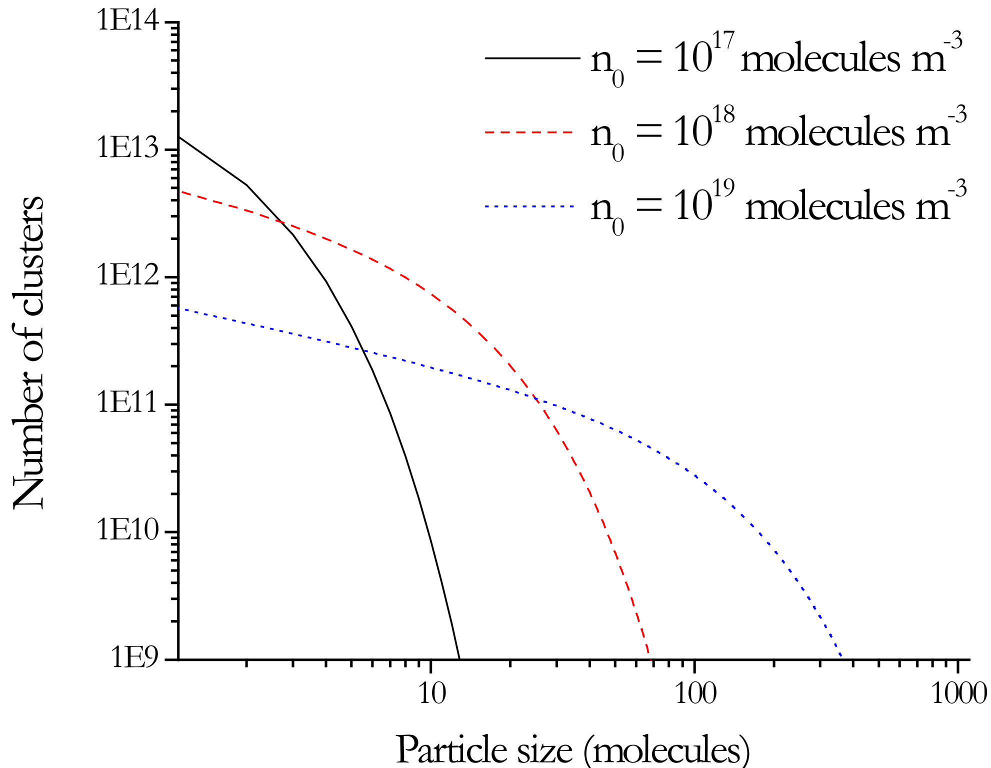


Figure 2-4: Theoretical particle size distributions for differing $n_0$ values. For this plot, the time of flight was 0.02 s.

the model predicts unacceptably large particles if the initial concentration exceeds ~ $10^{19}$ molecules $L^{-1}$, as particle sizes can theoretically reach 500 molecules shown in figure 2-4 for a time of flight of 0.02 s.

## Section 3
## Particle Deposition Model

Once the particle beam exits the mixing region, the hydrodynamics can be described by the axisymmetric stagnation-point flow model, represented by figure 2-5. The beam exits the nozzle located below the substrate at a position ($z^*$) with a velocity ($u_o$) varied by experiment. In order for the AAS system to follow the predictions made by this model, the inter-system spacing must obey certain geometric constraints. This condition is satisfied for a $z^*/r_{nozzle} \leq 4$.

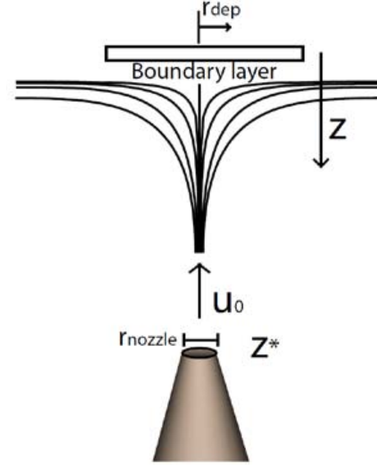


Figure 2-5: Schematic representation of the axisymmetric stagnation-point flow region

Due to the high degree of dilution of the heated sublimate, we assume that the temperature of the carrier gas is uniform and close to room temperature. (Preliminary experiments later confirmed this result, as the gas exiting the nozzle showed only a 1 degree Celsius increase in temperature.) Assuming the flow has zero viscosity (inviscid) and is incompressible near the stagnation point ($z$ = 0, $r_{dep}$ = 0) leads to the formation of hyperbolic streamlines with velocity components given by equations 2-6 through 2-8 as previously reported by D. F. Rogers.[4]

(2-6) $$v_r \approx ar$$

(2-7) $$v_z \approx -2az$$

(2-8) $$a = \frac{dv_z}{dz} \approx \frac{u_0}{2z*}$$

Where $a$ ($s^{-1}$) is the rate of change of the z-component of the flow between the nozzle and substrate (known as the axisymmetric flow constant), r (m) is the radial position in the beam, and z (m) is the vertical position in the beam. Note that the z component of velocity for particles exiting the nozzle will be independent of their radial position due to equation 2-6 and that the vertical velocity component of the gas is independent of radial position due to equation 2-7. *Therefore, we expect no radial dependence on particle flux rate or particle size leading to radially uniform thin film growth for the region directly above the nozzle ($r_{dep} \leq r_{nozzle}$).* This property of axisymmetric stagnation-point flow makes it potentially a very powerful method for depositing highly uniform films. However, this model will only produce accurate results for a small region above the nozzle ($r_{dep} \leq r_{nozzle}$), where the substrate is considered to be comparatively large with respect to the nozzle ($R >> d$).

As z approaches zero, so does the vertical component of velocity due to the no-slip boundary condition, which states that at a solid boundary, a fluid will have zero velocity relative to the boundary.[5] This leads to the formation of a boundary layer, with a uniform thickness δ over the entire deposition area calculated using equation 2-9:[6]

(2-9) $$\delta = \sqrt{\frac{v}{2a}}$$

Where ν ($m^2\ s^{-1}$) is the kinematic viscosity of the carrier gas. In order for a particle to reach the substrate, it must diffuse through this boundary layer. Particles may penetrate this layer through diffusion, by the action of non-flow forces such as gravitational or electrostatic forces, or as a result of inertia. However, for the system

in question, inertia will play no role due to the small size of the particles and electrostatic forces will be negligible (see chapter 3).

An appropriate model for transport of small particles across the boundary layer will follow the work done by Cooper *et al.* who analyzed the mechanics of particle deposition with gravimetric and electrostatic forces.[7] The particle flux at the substrate $j$ (particles $m^{-2}$ $s^{-1}$) is calculated using equation 2-10:

(2-10) $$j = nSh\frac{D}{r_p}$$

Where $n$ (molecules/$m^3$) is the concentration of gas phase particles at the boundary layer interface, $D$ ($m^2$ $sec^{-1}$) is the diffusion coefficient for these particles, $r_P$ (m) is the particle diameter, and *Sh* is the Sherwood number, a non-dimensional mass transport coefficient. The Sherwood number in this case will include two transport terms, gravitational and diffusional calculated with the Péclet number using equation 2-11:

(2-11) $$Sh \approx 0.616Pe^{\frac{1}{3}} - K_g$$

The gravitational constant is negative in our case due to the inverted geometry. The diffusion of particles through the boundary layer is calculated from the Péclet number (a dimensionless number relating the rate of advection to diffusion) by equation 2-12:

(2-12) $$Pe = \frac{2v}{D}\left(\frac{4apr_p}{\mu}\right)^{\frac{2}{3}}$$

The force due to gravity ($K_G$) can be calculated as the work done on a particle divided by its thermal energy (The force gravity exerts is simply particle mass times the acceleration constant and the distance this force acts is the radius of the particle, multiplied together to give work). Therefore, $K_g$ is given by equation 2-13:

$$K_g = \frac{mgr_p}{k_bT} \quad \text{(2-13)}$$

Where $m$ (kg) is the particle mass, $g$ (m sec$^{-1}$) is the acceleration due to gravity, $r_p$ (m) is the particle radius, Boltzmann constant and temperature. From these equations, it is clear that particle size will strongly affect deposition rate though the inclusion of $Kg$. Particle size is directly proportional to particle mass, and therefore larger particles will have a larger $Kg$ and thus a smaller j. Additionally, for the condition of Pe>>$K_g$, the deposition rate scales as $r_p^{-5/9}$. *Therefore, due to the dynamics of the boundary layer, there exists a particle size dependent deposition rate causing preferential deposition of smaller particles.* To model the particle size distribution of molecules that actually deposit on the substrate, we combine the two previous models (aggregation and deposition). As shown in figure 2-6, the majority of deposited particles are of size smaller than 10 molecules (for the idealized case when $n_0$ is $10^{18}$ molecules m$^{-3}$ and time of flight is 0.02 s). Additionally, by increasing the flow rate from 0.01 to 0.13 m/s (time of flights of ~0.3 s and ~0.02 s), we can increase the deposition rate by two orders of magnitude while maintaining a small particle size distribution. Therefore, there exists a regime accessible in the AAS system that will allow for deposition of small particles even though experiments are carried out under ambient conditions.

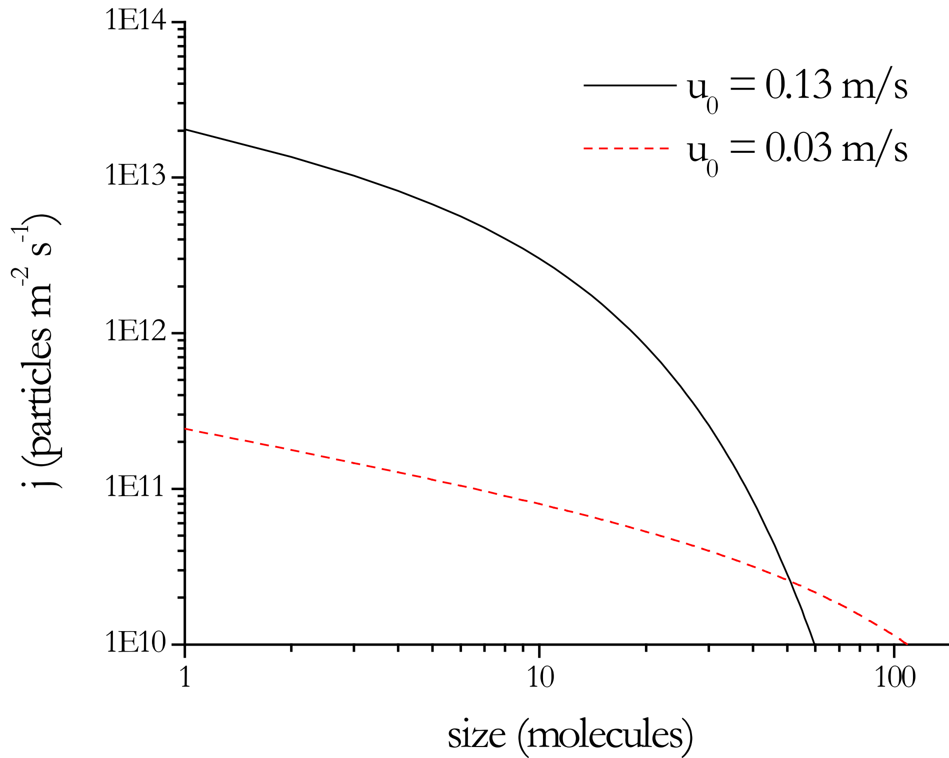


Figure 2-6: Theoretical deposition rate with respect to flow rate. The input parameters for these plots were: $n_0 = 10^{18}$ molecules $m^{-3}$; time of flight = 0.02 and 0.2 s respectively.

As the initial concentration of sublimate is increased, the average size of vapor phase clusters increases. As the boundary layer filters particles above a certain size, there will be a certain $n_0$ value which will give the highest deposition rate of preferred sizes. Therefore, as one of the goals of the AAS system was to improve the deposition rate of the OVLS method, sublimation rate must be kept relatively high. With a high sublimation rate however there exists a possibility for larger particles to pass the boundary layer if the gas flow rate is kept high. This problem cannot be solved by simply decreasing the flow rate as doing so increases the time of flight, which has a

significant effect on the resultant particle size distribution. Therefore, the flow rate and initial concentration of sublimate must be tuned in conjunction to keep the size of vapor phase particles low while keeping the concentration of vapor phase particles in the particle beam reasonably high.

Additionally, the particle stream exiting the nozzle must be laminar. Laminar flow is defined as collimated flow with uniform streamlines, represented in figure 2-7A. If the flow exiting the nozzle is turbulent (figure 2-7B), then large vapor phase aggregates will form and, as the boundary layer at the substrate cannot form under turbulent conditions, those large particles will deposit on the substrate. For the AAS system, the Reynolds number is kept below the theoretical laminar to turbulent transition (~2000)[8]. The Reynolds number in this case is calculated for a pipe flow by equation 2-14:

$$Re = \frac{\rho u D}{\mu} \tag{2-14}$$

Where $u$ (m/s) is the mean fluid velocity, $D$ (m) is the diameter of the pipe, $\mu$ (Pa s) is the dynamic viscosity of the carrier gas and $\rho$ (kg m$^{-3}$) is the density of the carrier gas. The flow inside the AAS system could also become turbulent by a length dependent transition. However, the system is designed so there is insufficient spacing for this type of transition.

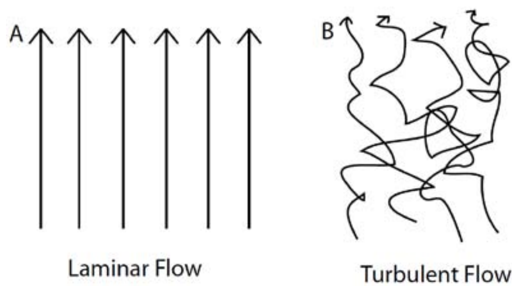

Figure 2-7: Flow line representation of two distinct streamlines: A) Laminar and B) Turbulent flow

Another important consideration is the choice of gaseous environment as a

high viscosity gas will inhibit cluster formation by decreasing the rate of vapor phase collisions. However, a high viscosity gas will lead to a larger boundary layer and therefore decrease overall deposition rate. This is illustrated in figure 2-8, which shows a series of viscosities for both the particle size distribution and the deposition distribution, presented as figure 2-8A and 2-8B respectively with the following input parameters: $n_0 = 10^{17}$ molecules $m^{-3}$, time of flight= 0.04 sec. As shown, a larger viscosity gas will lead to a larger deposition rate because the particle size distribution will remain small, having a much larger impact on $j$ then the boundary layer thickness.

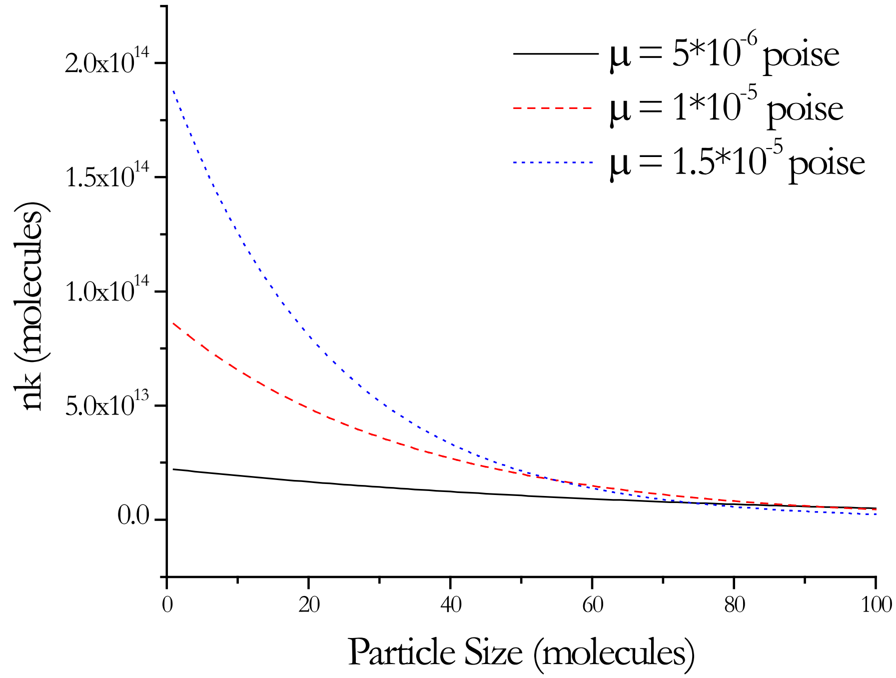


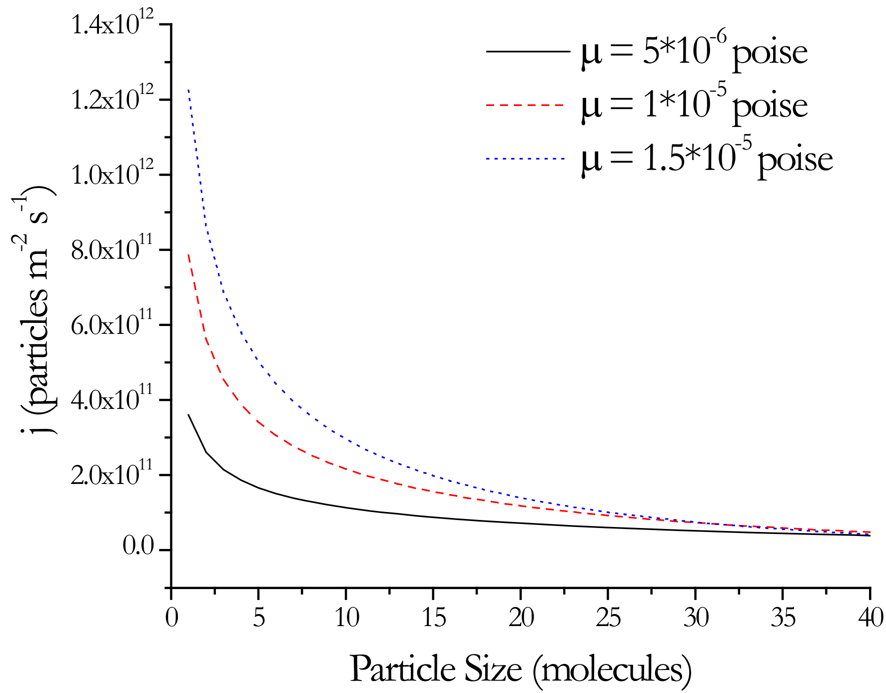


Figure 2-8: A) particle size distributions for different dynamic viscosities.
B) deposition rate distributions for different dynamic viscosities.

In addition to dynamic viscosity, the gas density will have a small impact on the resultant deposition rate distribution. Since a denser gas will lead to a smaller boundary layer, the overall deposition rate will increase slightly with a higher density gas due to a decrease in boundary layer filtering effectiveness. This result is presented in figure 2-9 for three different gas phase densities. The size of the scale for ρ used should indicate that the gas density has only a small effect of the system. The input parameters for figure 2-9 are: $n_0 = 10^{17}$ m$^{-3}$, $t = 0.04$ s.

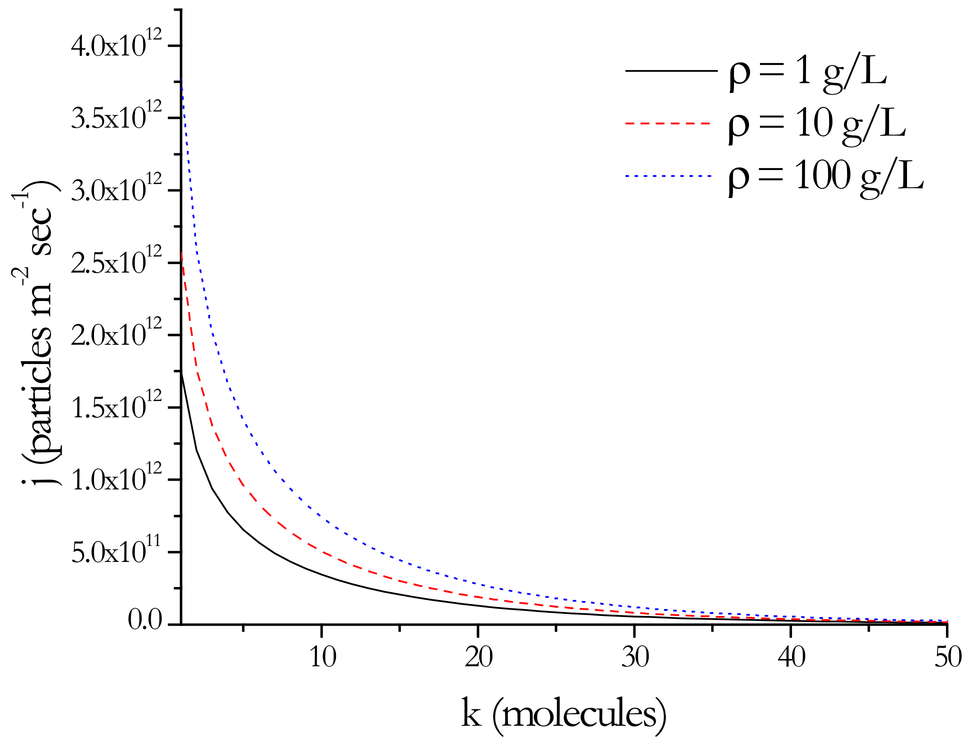


Figure 2-9: Theoretical effect of gas density on deposition rate distribution.

## Section 4
## Experimental Data

In order to grow high quality organic semiconductor thin films, it is necessary to deposit the smallest possible particles on the substrate (preferably monomers). It was discovered that for flow rates above a critical point, large clusters were deposited in large volume. At these large flow rates, a significant amount of turbulence existed in the chamber, increasing deposition rate of large aggregates. Additionally, turbulence leads to a greater degree of mixing throughout the chamber as diffusion is no longer the dominant force driving vapor phase particle collision. This increase in flux makes particle collision in the vapor phase more probable, and thus allows for formation of larger vapor phase aggregates. The form of these large vapor phase aggregates varied widely, ranging from complicated elongated structures to compact crystals presented in figure 2-10, and would have obvious detrimental impact on the resultant film's growth.

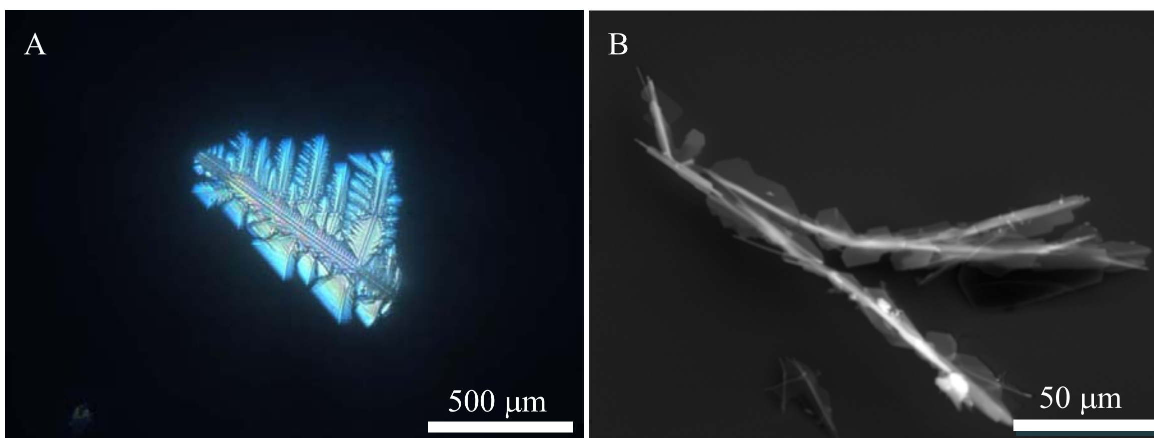


Figure 2-10: POM image of A) a large anthracene vapor phase aggregate (~$10^4$ molecules) and B) SEM image of a large tetracene vapor phase aggregate (~4500 molecules). Note that the anthracene vapor phase aggregate is significantly larger due to anthracene's ability to more readily grow crystals.

In order to prevent the formation and deposition of larger aggregates, it is necessary to experimentally determine the range of useable flow rates. Therefore, a series of experiments was performed over a range of inlet gas pressures with the results shown in figure 2-11 (with higher inlet pressures leading to higher flow rates). Below the critical flow rate, the deposited particles were sufficiently small and the resultant films showed no evidence of vapor phase growth, shown in figure 2-11A&B. However, above the critical flow rate, large yellow tetracene vapor phase aggregates appeared, shown in figure 2-11C. When the flow rate increased, the number of vapor phase aggregates increased as shown in figure 2-11D.

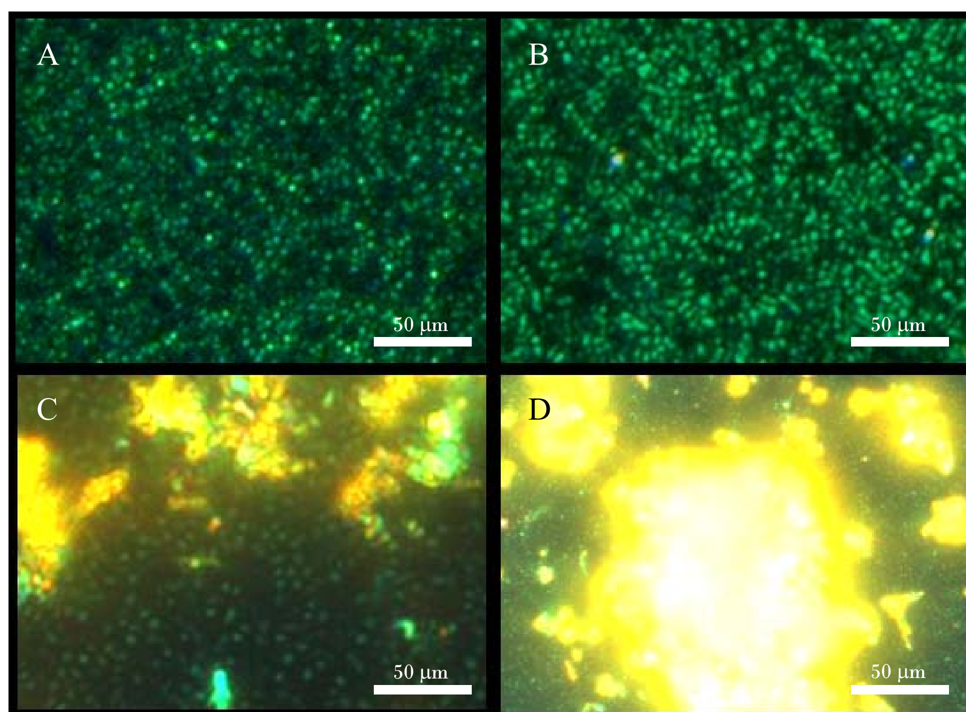


Figure 2-11: Polarized optical microscopy images of tetracene films grown with increasing inlet pressure (and therefore flow rate) at 400 x magnifications. A) 10 psi B) 20psi C) 30 psi D) 40 psi. The large yellow clusters in parts C&D are large vapor phase aggregates

In order to find the working ranges of sublimation rate, a series of tetracene thin films were grown at varying values of S (from equation 2-1). While a quantitative value for S is difficult to calculate, if one assumes the pressure, area of sublimate, and mass of sublimate are fixed and vary the temperature, we can calculate a comparative sublimation rate shown in equation 2-16.

(2-16) $$S \sim T_{cruc}^{1/2}\, e^{-1/T_{cruc}}$$

The results of an experiment performed with differing crucible temperatures (and therefore sublimation rates) are presented as figure 2-12 (Absorbance is used as a surrogate for total amount of material deposited). From this experiment set, we can

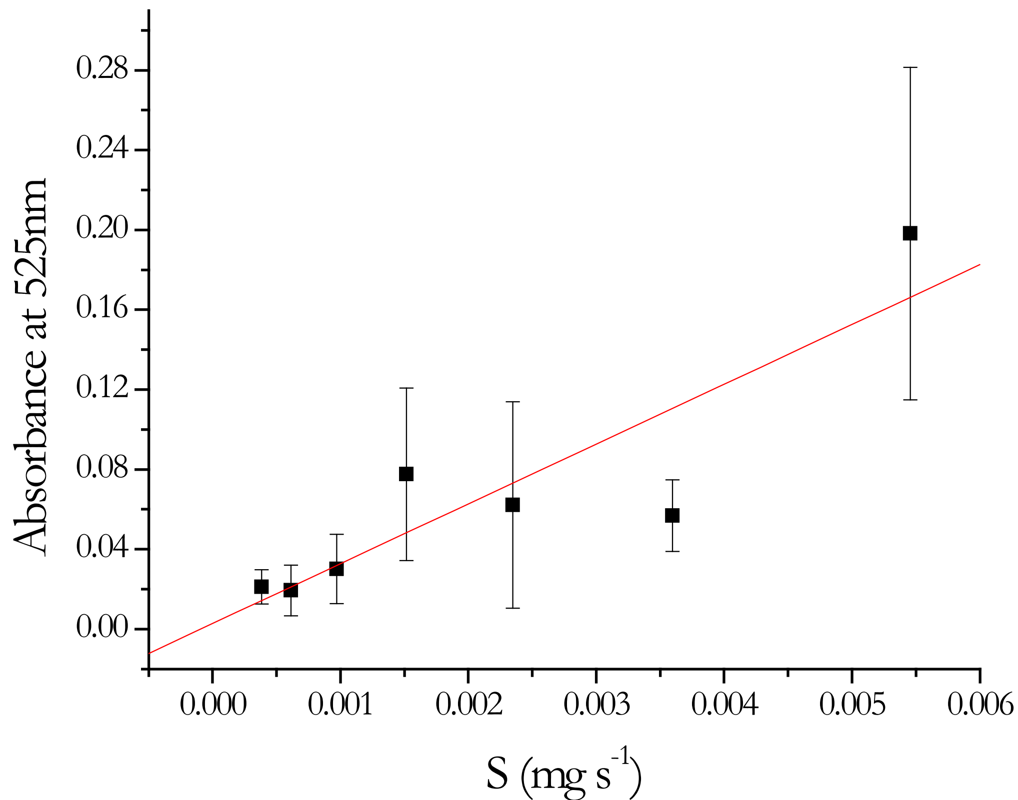


Figure 2-12: Total coverage of tetracene calculated by absorbance, measured at 525nm.

conclude that the deposition rate is linearly proportional to the sublimation rate for the range of crucible temperatures presented. Also, it is clear that the sublimation rate can be reliably tuned by the application of equation 2-18.

To a first order approximation, coverage is equal to flux rate multiplied by deposition time. Due to the importance of flux rate in surface dynamics calculations, an attempt was made to calculate flux rate. By studying coverage as a function of deposition time, we discovered that the deposition rate (and thus flux rate) held steady for a certain low coverage regime. However, after 20 min, the deposition rate

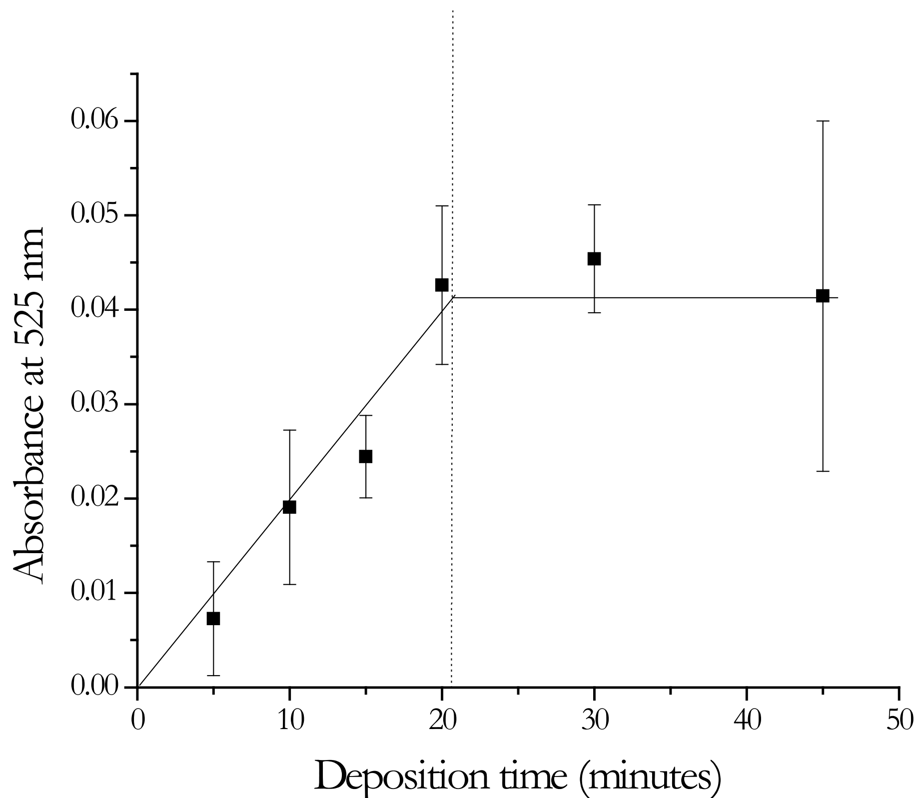


Figure 2-13: Coverage with respect to deposition time, with coverage measured by absorbance at 525nm.

declined to near zero. This result is shown in figure 2-13, with the deposition cut off shown at ~20 min. Coverage here is again measured as a function of absorbance at 525 nm. This result does not indicate the flux rate declines to near zero after 20 min but that 20 min is all that is required for the AAS system to deposit sufficient material to critically cover the substrate. At this point, the film is so dense that new nucleation is impossible and thus incoming particles will collide with existing crystals. As the dominant morphology encountered for tetracene crystals grown by the AAS system are platelets in which planar growth greatly outweighs out-of-plane-growth, the growth rate of crystals beyond this critical coverage is sufficiently lower.

The AAS system produces films with a high degree of radial uniformity for the area directly above the substrate ($r_{dep} \leq r_{nozzle}$). To quantify this behavior, a position relative optical intensity study was performed by POM with a band pass filter (500nm to 575nm) over its illumination source. The intensity of transmitted light was measured by a photo detector for a 0.85 mm by 0.65 mm rectangular region and absorbance was plotted as a function of radial distance from the center of the nozzle (figure 2-14). For this experiment, the diameter of the nozzle was ~3.5 mm. The area of the substrate directly above the nozzle ($r_{dep}$ < 1.75mm) shows relatively uniform deposition volume. Additionally, the size of the crystals on the substrate had

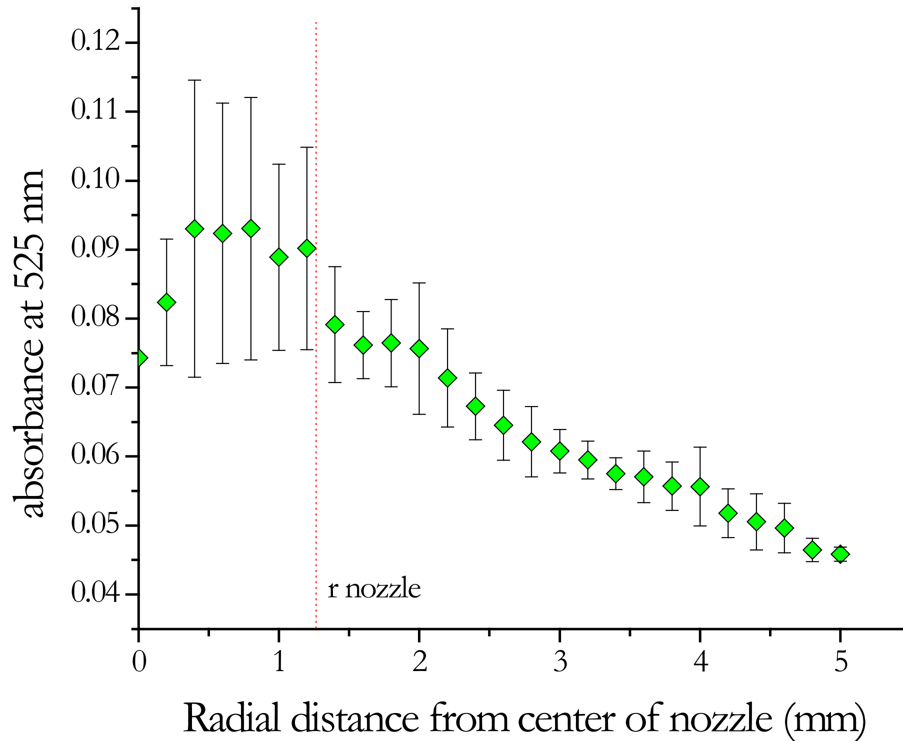


Figure 2-14: Radial intensity study for a tetracene film grown by the AAS method

qualitatively similar sizes. However, for all $r_{dep}$ values greater then $r_{nozzle}$, the deposition rate falls off rapidly with distance.

## Section 5
## Growth Kinetics

In an attempt to further understand the dynamics of the AAS system's flux, experiments were performed on bare substrates and analyzed for growth trends. The surface dynamics of films grown on bare substrates has been intensely studied in relation to epitaxial growth, and relationships between crystal size, crystal spacing, flux rate, nucleation rate, nucleation density and coverage have been developed which are applicable to a large number of different OMBE grown films.[9,10,11,12,13,14,15,16,17,21] While the sizes of particles deposited on the substrate for the AAS method are not assumed to be predominantly monomers, we will assume the arriving particles are small enough to undergo diffusive motion on the substrate (a result later confirmed by experiment).

Figure 2-15 shows a schematic representation of the surface of a substrate to which vapor phase particles of organic semiconductor impinge as well as the resultant competing processes. All of these processes occur simultaneously with characteristic rates, thus making it possible to classify the dynamics of growth by applying existing

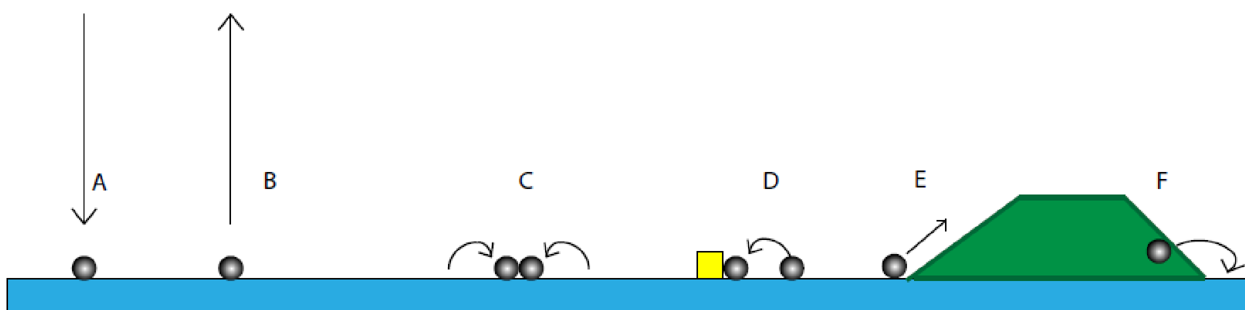


Figure 2-15: A visual representation of the concurrent processes of epitaxial growth.

models. Figure 2-15A represents adsorption of a monomer onto a bare area of the substrate. If the monomer has sufficient energy it can overcome the binding energy and desorb from the surface, shown in figure 2-15B. Should the monomer remain on the substrate, it will diffuse in a semi-random motion until it collides with another object on the substrate, be it another monomer (figure 2-15c), a defect site (figure 2-15d), or an existing crystal (referred to as an island (2-15e)).[18] If a monomer collides with another monomer on the surface, it forms an island. This island may be mobile (depending on the strength of surface/cluster binding and the temperature) and will either grow or shrink depending on whether or not it is stable. The stability of an island is dependent upon both the substrate/island interactions and the intermolecular forces of the monomers. The smallest stable size of an island is known as the critical nucleus size ($i$) plus one additional monomer. The critical nucleus size is therefore defined as the smallest island size in which growth outweighs dissociation and thus becomes a nucleation site. A nucleation site is defined as a cluster (or monomer) which serves as a seed to grow a larger crystal. If a monomer comes into contact with a defect site, it can become tightly bound and serve as an additional nucleation site.

When a monomer or collection of monomers collides with an existing crystal, it will become incorporated into the crystal lattice and form crystals with differing fractal dimensions based on the ratio of flux rate (here defined as monomers arriving per unit time)

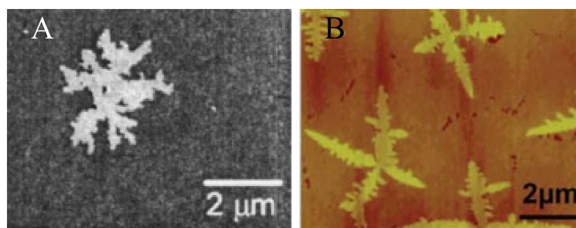


Figure 2-16: Examples of OMBE grown pentacene crystals on $SiO_2$ with A) low fractal dimension and B) high fractal dimension. Adapted from [20] and [21] respectively

and diffusion (speed at which a monomer can diffuse around the surface of the substrate). If the ratio of flux to diffusion is low, then monomers can diffuse around a crystal until they find their lowest energy conformation, resulting in compact crystals with a low fractal dimension (figure 2-16A).[19] When the ratio of flux to diffusion is high, monomers cannot diffuse around a crystal to find the lowest energy conformation, resulting in crystals with a high fractal dimension (figure 2-16B). [20]

For films grown by OMBE, there exist three distinct regimes separated by the rate of change of number of crystals over time, represented by figure 2-17.[18] The graph presents natural log of nucleation density (number of crystals per unit area) versus time. Initially, a substrate has a low density of crystals, and thus the growth of new crystals is the dominant process. The slope of this line is a strong indicator for growth kinetics (see below). When the nucleation density is sufficiently high, then nucleation of new crystals becomes improbable, and thus crystals simply grow. After crystals have grown to a size in which they begin to come into contact with their neighbors, the nucleation density declines, referred to as the coalescence regime.

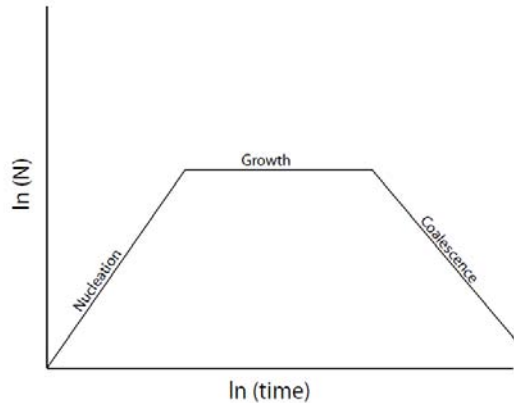

Figure 2-17: Regimes of epitaxial growth

As discussed earlier, we do not expect the incident particle flux to consist of primarily monomers, but we do assume that the incident particles are small and thus will undergo diffusive motion resulting in similar surface dynamics compared to films grown in high vacuum OMBE. In an attempt to determine whether the incident flux

consisted of particles small enough to undergo diffusive motion, a progressive deposition study was performed on tetracene thin films grown on a silicon wafer ((110) naturally grown oxide). The sample was subjected to a number of deposition steps, the results of which were imaged by SEM in the same 40 um x 30 um area. (In order to find the same area after each successive deposition step, it was necessary to create guides on the surface of the silicon sample. It is well known that a high energy electron beam can ablate surface atoms from a sample. Using this knowledge, the SEM electron beam was intensified (by increasing the current on the microfilament) to ablate the surface of the silicon wafer in locations of significant distance from the scan areas. A grid pattern of damaged locations was created to allow quick recognition of a 200um square area, from which each scan area can be located.) The imaged areas of the sample spent the minimal amount of time in the SEM's electron beam to avoid damaging the deposition area. The resultant SEM images are presented as figure 2-18 in order of total deposition time (A = 5 min, B = 10 min, C = 15 min, D = 30 min, E = 60 min, F = 120 min).

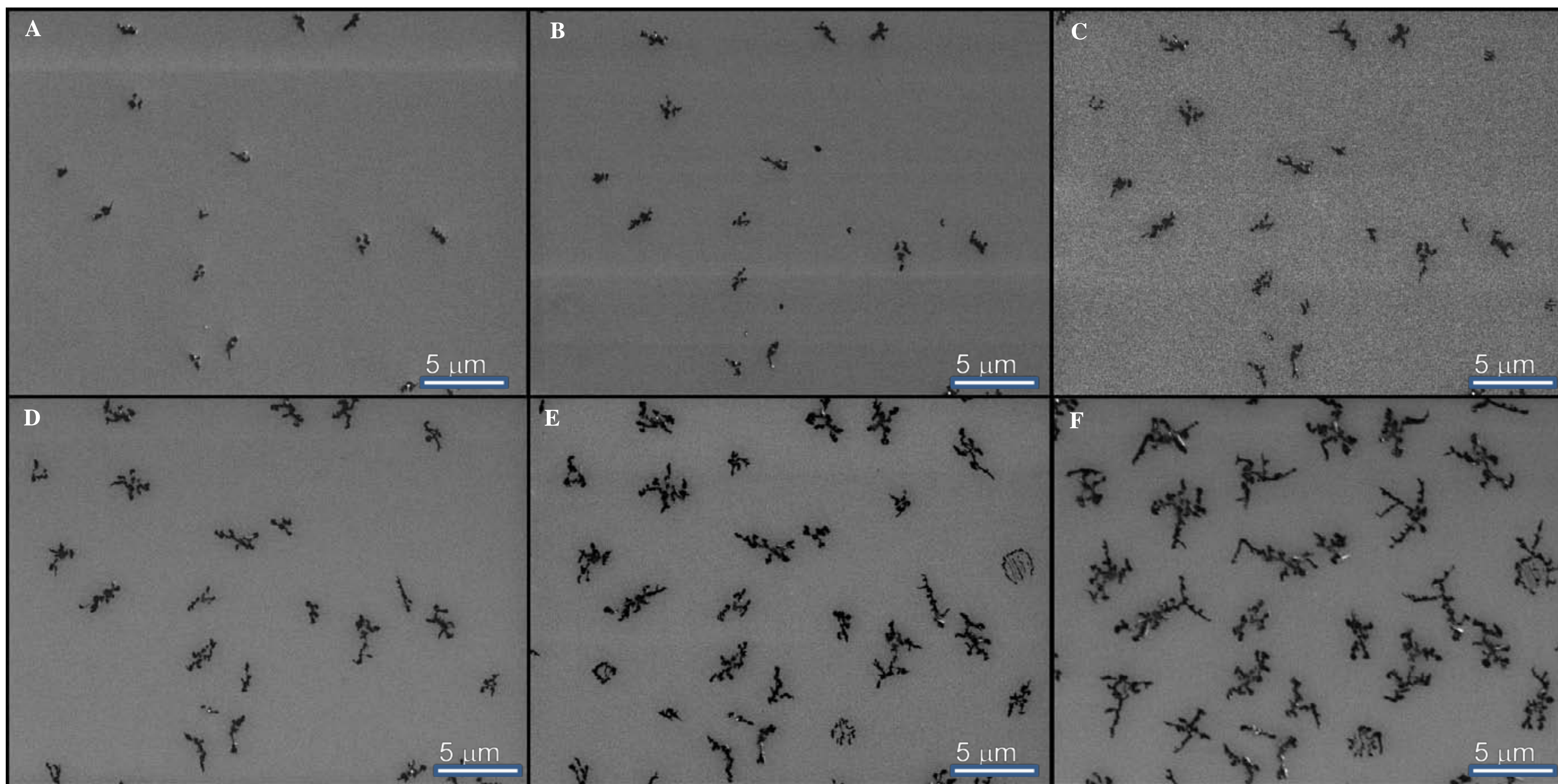


Figure 2-18: SEM images of tetracene films grown on silicon (100) at progressive deposition times of: A: 5 min B: 10 min C: 15 min D: 30 min E: 60 min F: 120 min

The crystals grown had a high fractal dimension, indicating a high flux to diffusion ratio. The fact that the crystals grew in volume with each deposition step states that they were able to capture additional material, indicating that the incident flux did consist of particle sizes small enough to undergo diffusive motion on the substrate. After 5 min, the nucleation rate of new crystals dropped, indicating that 5 min is sufficient to near the end of the nucleation regime. However, after longer deposition steps, a new morphology appeared. A high resolution AFM image of this morphology is presented in figure 2-19, which was not accounted for in the literature. Their unusual shape as well as their absence at shorter run times leads to the conclusion that this type of morphology either grew in the vapor phase or grew as a result of some impurity introduced in between the 30 and 60 min deposition step. The analysis of this progression study was performed by removing the abnormal morphologies and assuming that crystal height was directly proportional to 2D crystal volume.

Nucleation rate is an important variable as it can be used to extract useful growth kinetics information. Nucleation density can be used to calculate nucleation rate when considered as a function of deposition time. In the following section, we will use the equations given by Venables *et al.* Since the time of this work, many advances in this field have

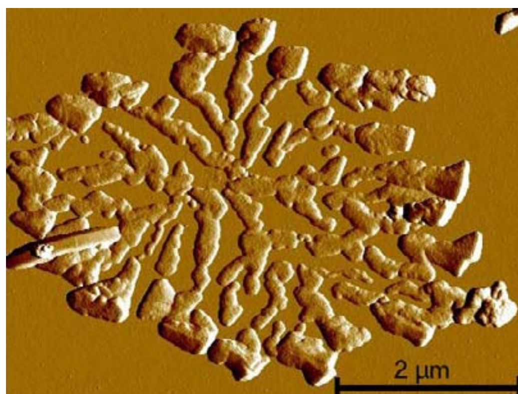

Figure 2-19: AFM image of long deposition time tetracene morphology

been made. However, the resolution of the data collected does not allow for a more rigorous analysis. The nucleation density $N$ (molecules/lattice site) is approximated by equation 2-17:[18]

(2-17) $$N \sim \theta^p \left(\frac{F}{D}\right)^p e^{\left[\frac{E}{(i+2)k_B T}\right]}$$

Where θ (monolayers) is surface coverage, $F$ (monolayers/s) is the flux rate, $D$ ($m^2\ s^{-1}$) is the diffusion rate, $i$ (molecules) is the critical nucleus size and E (joules) is a characteristic energy dependent upon substrate, compound, and growth regime. The value of p in equation 2-19 is an indication of the film's growth kinetics. There exist three different growth regimes: complete condensation, diffusion, and direct impingement.[18] In the complete condensation regime, all monomers that come in contact with the surface remain on the surface. These monomers are allowed to diffuse, nucleate and attach to existing islands. The diffusion regime allows for all the same processes as does the complete condensation regime and also allows for desorption of monomers. The direct impingement regime states that only monomers that impact existing monomers will cause crystal growth. In this regime, there is no diffusion, no nucleation (unless on a defect site) and no desorption. The value for p is dependent on the regime as follows: complete condensation ($p = i$), diffusion ($p = \frac{i+1}{i+3}$) direct impingement ($p = \frac{i}{i+2}$). These functions of p also depend on the critical nucleus size. Due to the fact that flux rate multiplied by time equals coverage, we can replace $\theta$ with $FT$ in equation 2-17.[21] When equation 2.4 is

rearranged, it is possible to create a natural log plot of the nucleation density versus both flux rate and time by equation 2-18.

(2-18) $$\ln(N) \sim p\left[\ln(FT) + ln\left(\frac{F}{D}\right) + \frac{E}{(i+2)k_B T}\right]$$

The slope of the resultant graph will give the value of p, and therefore it is possible to calculate the value of $i$. Equation 2-18 is applied to give figure 2-20, a natural log plot of the deposition time versus nucleation density obtained by SEM (Nucleation density can be defined as the number of nucleation sites (crystals) per unit area). The slope of the resultant graph was calculated to be 0.6.

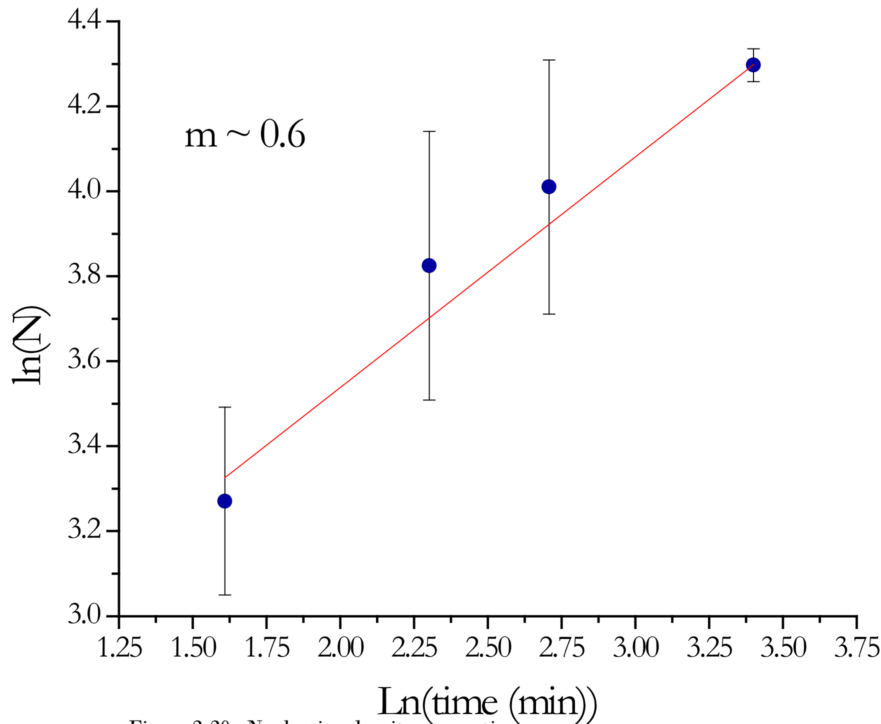

Figure 2-20: Nucleation density versus time.

As shown previously, sublimation rate can be reliably controlled by varying the temperature of the graphite crucible. Assuming that sublimation rate is directly proportional to flux rate, we can use sublimation rate as a surrogate for flux rate. In

order to confirm the results obtained by SEM, a number of films were grown on silicon (110) natural oxide at differing values of $T_{cruc}$. In this case, nucleation was measured by AFM in tapping mode. By applying equation 2-20 again except varying the value of F, we obtain figure 2-21. This plot also has a linear relationship and a p value of ~0.6. Looking at the equations for *p*, it is clear that this type of growth is defined by the diffusion regime as it is the only regime in which a value of 0.6 is possible. The results of this analysis suggest that the value for the critical nucleus for tetracene grown by AAS deposition on silicon (110) natural oxide is 2.

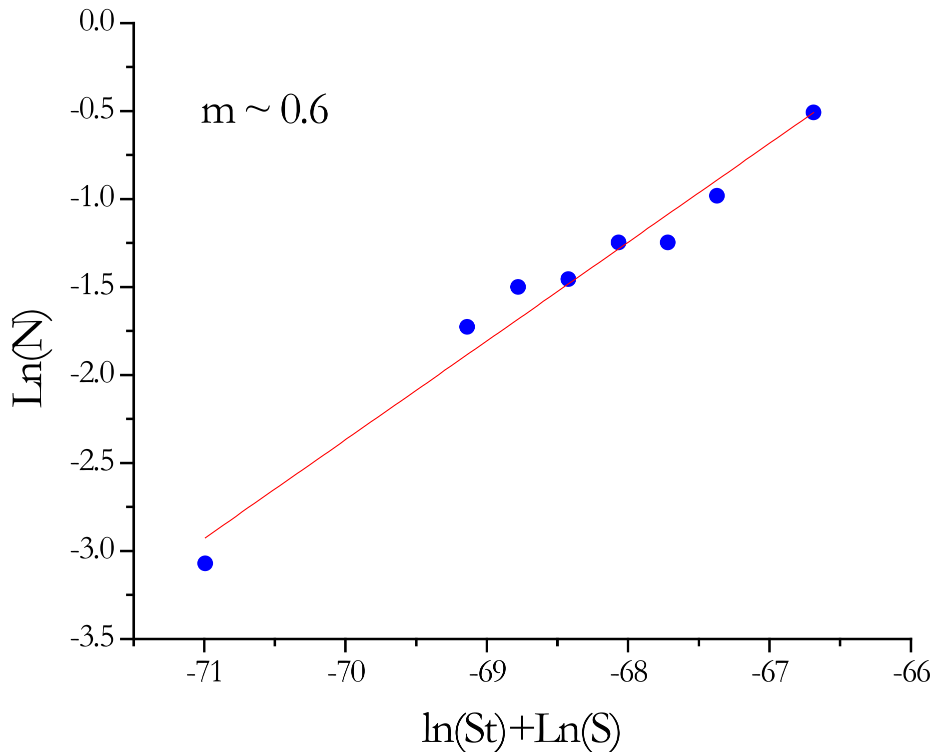


Figure 2-21: Density versus sublimation rate (controlled by crucible temperature) for tetracene film grown on Si(100) and observed by AFM

During the initial (low coverage) stage of crystal growth for this system, the crystal sizes are highly correlated. In fact, if one can measure the size of the crystals, then it is possible to construct a scaling plot by equation 2-19:

(2-19) $$N_s S^2 \theta = f(\frac{s}{S})$$

Where s (unit less) is the size of a crystal, S (molecules) is the average size of all crystals, Ns (a number density in units of per lattice site) is the density of crystals of size s, and *f(s/S)* solved analytically. Through our collaboration with Dr. Brad Johnson in the physics department of WWU, we obtained a function for *f(s/S)* which fits simulation data better than those reported in the current literature. The function depends only on the critical nucleus size and the ratio of size to average size (as is commonly reported) by equation 2-20:[22]

(2-20) $$f\left(\frac{s}{S}\right) = A_i x^i e^{-(b_i u - 1/2)^2}$$

With $A_i$ and $b_i$ solved by applying conditions of unit normalization and unit mean, leading to equations 2-21 and 2-22:

(2-21) $$A_i = \frac{2b_i^{i+1}}{D(i)}$$

(2-22) $$b_i = \frac{B(i)}{D(i)}$$

With D(i) and B(i) defined by equations 2-23 and 2-24:

(2-23) $$D(i) = \Gamma\left[\frac{i+2}{2}\right] 1F1\ \left[\frac{1-i}{2}; \frac{3}{2}; -\frac{1}{4}\right] + \Gamma\left[\frac{i+1}{2}\right] 1F1\ \left[\frac{-i}{2}; \frac{1}{2}; -\frac{1}{4}\right]$$

(2-24) $$B(i) = \Gamma\left[\frac{i+2}{2}\right] 1F1\ \left[-\frac{1+i}{2}; \frac{1}{2}; -\frac{1}{4}\right] + \Gamma\left[\frac{i+3}{2}\right] 1F1\ \left[\frac{-i}{2}; \frac{3}{2}; -\frac{1}{4}\right]$$

Where ${}_1F_1[a;b;c]$ is a confluent hypergeometric function. Equation 2-20 can now be used to create the size scaling plot shown as figure 2-22. For the low coverage images (5 min of deposition), the data scaled reasonably well, with large noise presumably due to low sample volume. However, the resolution of the data does not allow for a clear statement over the value of i. Figure 2-22A shows the case for $i = 1$, with the theoretical curve fitting just as well as figure 2-22B, which shows the case for $i = 2$. We therefore cannot make any solid conclusion between the two values of $i$ based on this plot.

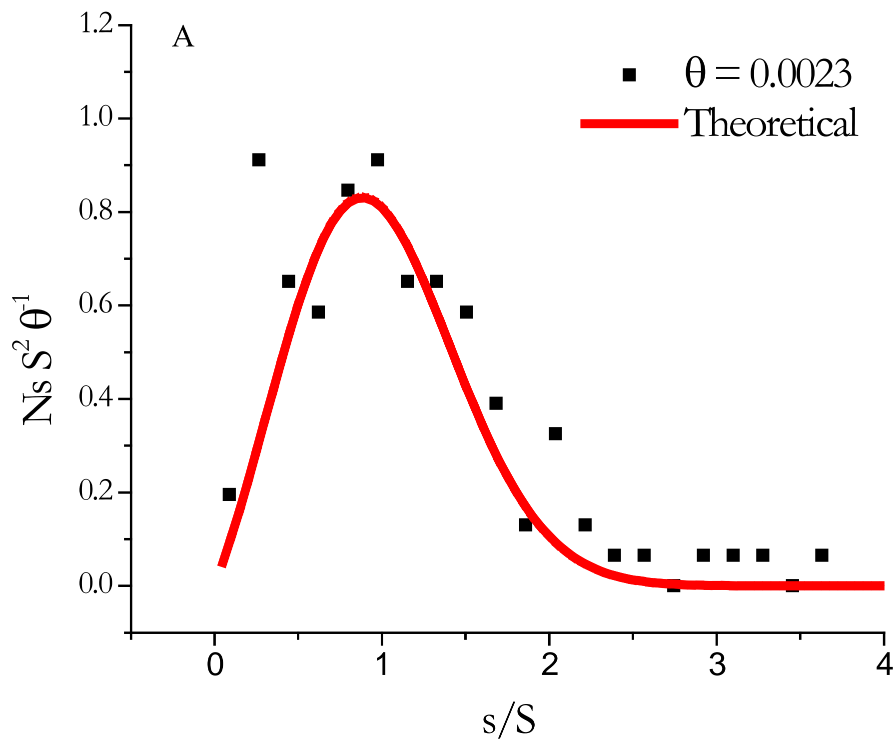


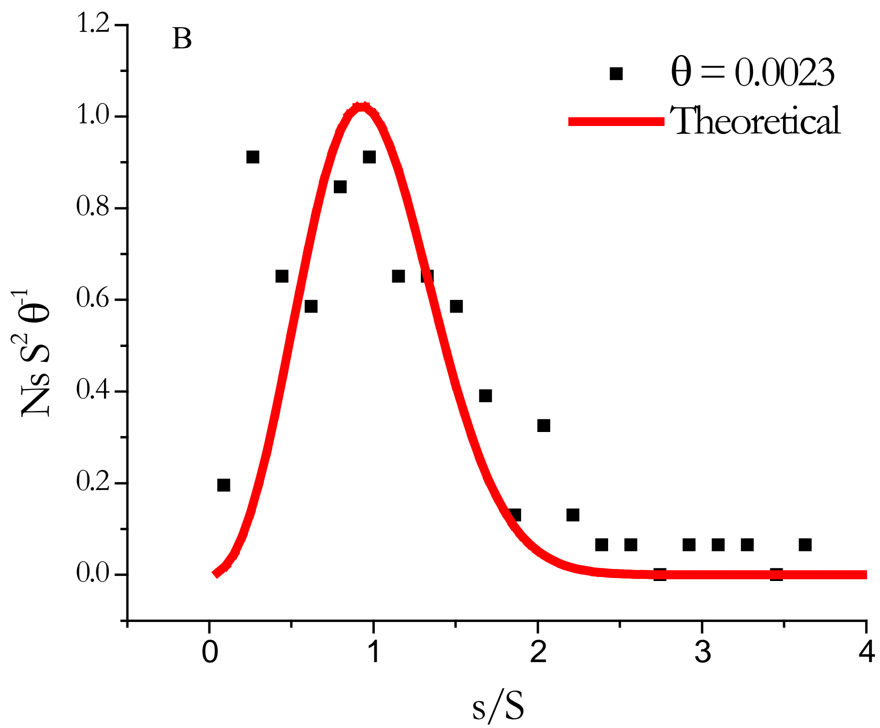


Figure 2-22: Size scaling plot for A) $i$ = 1 and B)$i$ = 2 for the low coverage images.

## Section 6
## Results

After the parameter space of the AAS system was explored, it was incorporated with OVLS substrates in an attempt to grow high quality thin films. As discussed previously, one must remain within certain experimental bounds in order to grow high quality organic semiconductor thin films. It was determined from the bare substrate data that there existed a range of parameters in which growth of films of sufficient quality existed. The AAS system was then explored within this range to find the optimum parameter space.

Presented in figure 2-24 is one of the best films grown by incorporation of the AAS system with OVLS substrates method. An ITO coated slide with a 100 um thick polyimide alignment layer and 1200 um thick film of EM Industries' LC ZLI-3471 was used to grow a tetracene thin film. This particular LC was chosen because it had shown promising results when used with tetracene in previous OVLS experiments. The resultant thin film is presented as figure 2-23 and shows many characteristics of a high quality thin film, namely, large crystal sizes (~30 to 50 μm) and uniform crystallographic orientation. The range of morphologies present in figure 2-23 illustrates that the growth medium chosen was capable of producing phase pure films. However, to grow this film, a very low flow rate was used. At these parameters, the AAS system offers little advantage in the area of high throughput film growth. In fact, the unaided OVLS system has grown films of comparable quality on the same timescale.

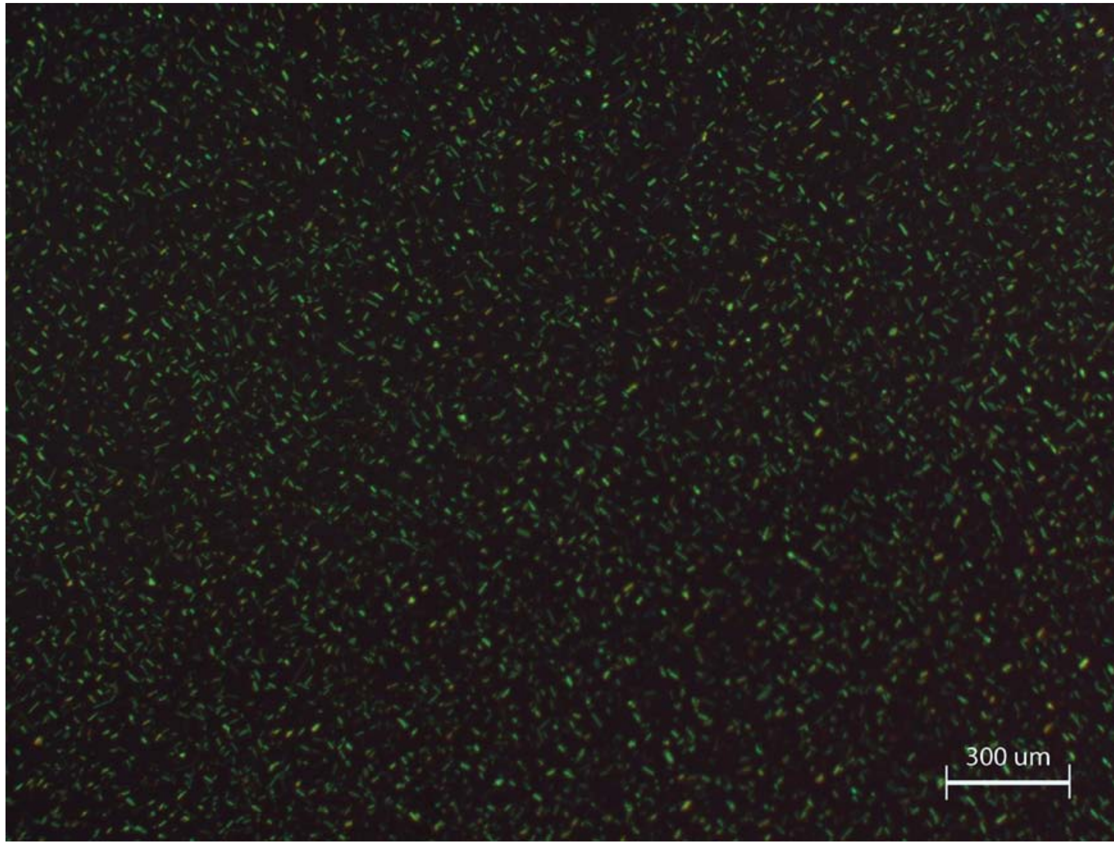


Figure 2-23: POM image of a tetracene thin film grown by AAS on an ITO coated glass substrate with a polyimide alignment layer and ~1200 nm thick film of the LC ZLI-3417

In order to increase the rate at which high quality films of tetracene grew, the rate of deposition for the AAS system was increased. The AAS system's deposition rate can be increased only by either increasing the sublimation rate or the gas flow rate. While the AAS system was found to be capable of growing high density films in under 30 min, the quality of these films never reached an acceptable level. Also, the lack of reproducibility meant that if a promising result was given, it was impossible to improve upon or even repeat. The reason behind this setback lies with the experimental bounds for the variables $u_0$ and $n_0$. When the sublimation rate was increased, the concentration of larger vapor phase aggregates was sufficient to allow for deposition of particles over 200 μm in size. Also, the average incident particle size

was too large to readily dissolve in the liquid layer even with the incorporation of substrate heating. When the gas flow rate was increased, the liquid layer on the substrate was effectively pushed out of the deposition region, even though the solvent was a high viscosity liquid crystal.

Incorporation of the AAS systems with the OVLS method resulted in mixed success. The AAS system provided sufficient controllability necessary to grow high quality films by the OVLS method. However, the goal of increasing deposition rate was deemed improbable due to the issues associated with the variables $n_0$ and $u_0$. It was therefore concluded that an additional force for particle deposition was needed, namely, electrostatic attraction. The inclusion of electrostatic forces will be presented in chapter 3.

# Chapter Two References


**1** M. Tesconi, M. Pikal, S. Yalkowsky, *J. Pharmaceutical Sci.*, **1997**, *86*.

**2** S. Mahajan, K. S. S. Harasha, *Principles of Growth and Processing or Semiconductors*, McGraw-Hill, 1999, p 239

**3** Elimelech, M.; Gregory, J.; Jia, X.; Williams. R.A. (1998). Particle Deposition and Aggregation - Measurement, Modelling and Simulation. (pp: 25-75).

**4** D. F. Rogers, Laminar Flow Analysis, Cambridge University Press, Cambridge, UK (1992)

**5** M. A. Day, *Erkenntnis*, **1990**, 33.

**6** R. J. Kee, M. E. Coltrin, P. Glaborg, "Chemically Reacting Flow Theory and Practice", John Wiley and Sons, Hoboken, N.J. (2003).

**7** D. W. Cooper, M. H. Peters, R. J. Miller, *Aerosol Sci & Technol.* **1989**, 11.

**8** R. H. Perry, C. H. Chilton, Introduction to Fluid Dynamics, In *Chemical Engineer's Handbook*, fifth edition; H. B. Crawford, R. J. Kelper, Eds.; R. R. Donnelly and Sons: New York, 1973; 4-5

**9** P. Jensen. *Rev. Mod. Phys.*, **1999**, 71

**10** M. Campione, S. Caprioli, M. Moret, A Sassella, *J. Phys. Chem.* **2007**, 111.

**11** S. Verlaak, S. Stuedel, P. Heremans, D. Janssen, M. S. Deleuze, *Phys. Rev. B* **2003**, 68.

**12** P. A. Mulheran, M. Basham, *Phys. Rev. B.* **2008**, 77.

**13** M. Tomellini, M. Fanfoni, *Current Opinion in Solid State & Materials Science*, **2001**, 5.

**14** M. Campione, A. Borghesi, M. Moret, A. Sassella, *J. Mat. Chem.* **2003**, 13.

**15** M. N. Popescu, J. G. Amar, F. Family, *Phys. Rev. B* **2001**, 64.

**16** F. Shi, Y. Shim, J. G. Amar., *Phys. Rev. B* **2005**, 71.

**17** J. G. Amar, F. Family, M. N. Popescu, *Computer Physics Communications* **2001**, 1.

**18** J. Venables,Surface processes in epitaxial growth. *Introduction to Surface and Thin Film Processes*, 1st edition, Cambridge University Press: Cambridge UK, 2000; 1, 145-156

**19** V. Kalihari, E. B. Tadmor, G. Haugstad, *Adv. Mater.* **2008**, 20.

**20** S. Pratontep, M. Brinkmann, F. Neusch, L. Zuppirolo, *Phys. Rev. B.* **2004**, 69.

**21** J. W. Evans, P. A. Thiel, M. C. Bartlet, *Surface Science Reports*, **2006**, 61

**22** B. L. Johnson, B. R. Hillman, D. L. Patrick, submitted for publication, **2010**

# Chapter Three

## Ambient Axisymmetric Spray with Particle Charging

Presented in this chapter is a new method for growing high quality organic semiconductor thin films using a system similar to the one presented in the previous chapter but with two significant improvements: namely, the inclusion of particle charging and mixing region purging. It was stated previously that a desired rate of deposition for the AAS system was unobtainable due to the issues associated with increasing sublimation rate and carrier flow rate. Therefore, an additional transport term in the deposition rate equation is necessary in order to achieve the goals of the thesis. It was concluded that particle charging by electrical discharge could increase the deposition rate by several orders of magnitude as it allows vapor phase particles to overcome the static boundary layer and therefore deposit on the substrate at a much higher rate. In this chapter I describe a modification to the AAS method that implements this charging concept, introduce a theoretical framework to account for its effects, and present the results of experiments characterizing its performance.

Electrical discharges have long been observed in nature in the form of lightning, northern lights, and St. Elmo's fire but were widely misunderstood. During the 19$^{th}$ century, electricity became more available, and fundamental experimentation on discharges began with early applications such as radio transmission, lightning arrestors, and ozone production. To this day, electrical discharges act as the basic part of many common sources for photons and charged particles. In fact, they have become so widespread that we see them almost everywhere, from fluorescent lighting,

to ozonizers, arc welders and furnaces and even surface hardening equipment. It is now well known that electrical discharges are strongly dependent upon electrode voltage, inter-electrode distances, electrode material, gas pressure, and gas composition. Therefore, controlling the environment in which the discharge takes place is essential.

The environment within an electrical breakdown can be described as a high field region in which a large density of high energy free electrons and ions exist. The fact that a discharge occurs implies that there are at least some charge carriers available since an electric field has little effect on neutral species. Under atmospheric conditions, there exist roughly $10^6$ free electrons per cubic meter due to cosmic radiation.[1] A discharge event begins when a free electron acquires kinetic energy from an electric field, or more accurately from the voltage source. The magnitude of the kinetic energy an electron acquires is based on its mean free path and the field strength. The free electron will eventually collide with a gas phase molecule, thus transferring some of its energy to either translational, rotational, or vibrational energy or cause excitation or ionization. Translation, rotation and vibration will have little impact on the behavior of the particle in plasma, and are therefore of little importance for this work. Excitation is a process in which a high energy electron induces a transition of an electron (on the molecule or element it collides with) to a higher energy state. This process requires an electron with several eV, depending on the molecule or atom (for argon, the lowest excitation requires ~11 eV).[2] The now excited species can either decay by spontaneous emission of a photon or can impart

energy by collision with another gas phase molecule. In general, decay by radiation and collision are in competition, unless radiative relaxation is forbidden by selection rules, causing a metastable excited species. These metastable species can have energies high enough to cause fragmentation (known as Penning Ionization) and can have lifetimes of several seconds.[3]

Ionization inside an electrical discharge requires free electrons. There are two ways in which a molecule/atom can acquire a charge (without chemical modification). A relatively low energy electron can be captured by a neutral gas phase species in a process known as attachment, leading to the formation of an anion. Alternatively, if an electron can acquire sufficient kinetic energy over the length of its mean free path it can cause secondary impact ionization. Secondary impact ionization usually requires an election with a temperature above 10 eV, and removes a valence electron from the gas molecule creating an additional free electron as well as a gas phase cation. This situation leads to a phenomenon known as an electron avalanche, the propagation mechanism for plasma.

Electrical discharges have been utilized in the creation of what is known as electrostatic precipitators (ESP), which are of particular interest to this research due to their ability to remove gas phase molecules and small particles from the air. Most ESPs operate with a low-temperature plasma known as an electrical corona discharge.[1] An electrical corona discharge can be described as a self-sustained electrical gas discharge where a geometrically determined electric field confines the primary ionization process to regions close to high field electrodes.[4] There exist three

different possible corona discharges, distinguished by the charge on the electrode: DC negative, DC positive and radio frequency AC. The DC negative corona discharge was chosen for our system because it contains a higher concentration of free electrons of lower temperature then that of DC positive coronas and is therefore more efficient at particle charging and less efficient at generating ozone.[4]

## Section 2
## Corona Discharge

A configuration for corona formation of particular interest, known as point-to-plane discharge, is shown in figure 3-1, and consists of three main regions. The first region which directly surrounds the curved electrode is known as the ionization region. It consists of an area of high-field in which the governing processes of an electrical discharge are confined. Outside the ionization region is a low-field region where particles move under the influence of the field, known as the drift region. Near the oppositely charged plane, ionized gas phase species are collected on a substrate with a high magnitude opposite charge relative to the ionization region, known as the collector region (The collector region can be held at ground with respect to the atmosphere, as long as the requirement of a steep voltage gradient is satisfied.[4]) Charge is passed from the high field electrode to the collector region by gas phase ions, resulting in a current. The current for corona discharge is low, typically on the order of 10 μA even though voltages used typically lie in the range of 3-15kV. Corona discharges fall under the broader category of low temperature glow discharges, with a concentration of free electrons in the range of $10^8$ to $10^{12}$ $cm^{-3}$ with kinetic energies ranging from 1-20 eV depending on the geometry, voltage, and distance between electrodes.[5]

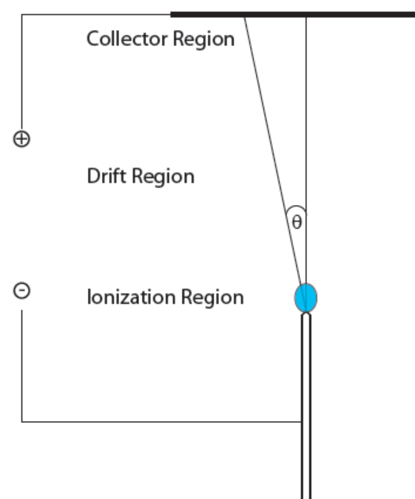


Figure 3-1: Regions of the point-to-plane corona discharge

Current measurements in a point to plane corona discharge are directly related to quantity of charged species impacting the collector. Therefore, by studying the relation of radial position on the plane versus current, it is possible to map the path of charged species between the ionization and collection region. By assuming that the collector is sufficiently larger than the corona discharge and that there is no gas flow, the radial current density becomes a simple function of θ by equation 3-1.[4]

(3-1) $$\frac{I}{I_{max}} \approx \cos^5(\theta)$$

Where θ is the angle between the tip of the ionizing electrode and the location on the substrate (shown in figure 3-1)

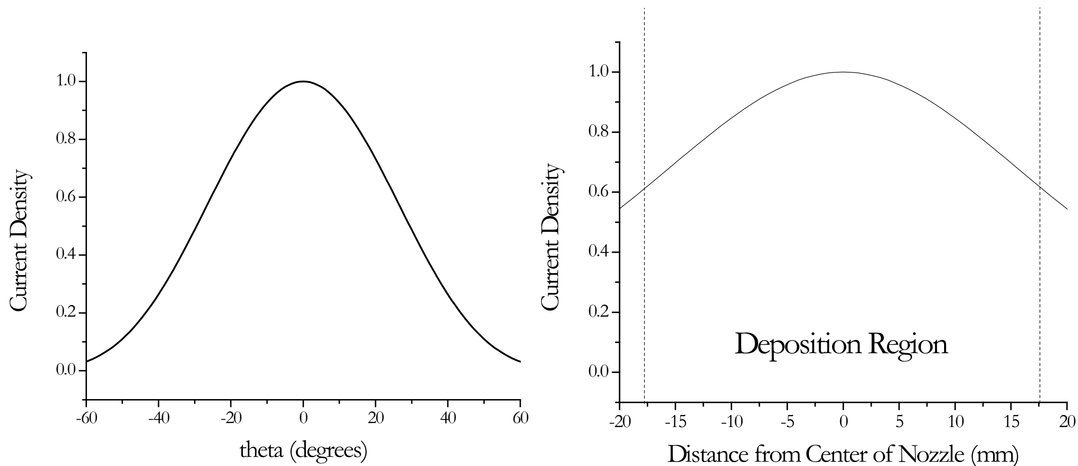


Figure 3-2: A) Radial current density plot for a point-to-plane corona discharge. B) Current density as a function of distance from the center of the nozzle.

Presented in figure 3-2A is a current density plot for a negative point to plane corona discharge.[4] It is clear that the point to plane corona discharge will give a fairly uniform distribution for small values of theta. Figure 3-2B illustrates the radial

current distribution in terms of distance from the center of the nozzle for the current system. These results indicate that an unfocused corona beam with no included gas flow would lead to a large deposition region with a strong radial dependence. Therefore, the beam must be restricted to a narrow passage to allow for retention of radial uniformity. Additionally, corona discharge's requirement for high field magnitude conflicts with the geometric restraints of the axisymmetric stagnation point model since the distance from the corona event to the substrate would be sufficiently small to allow for complete breakdown. Therefore, the ionization region is held further from the collector region and therefore the flow must be restricted.

# Section 3
# Modified AAS System

To increase radial uniformity, the point to plane discharge set up was modified by the addition of a focusing tube between the charging region and the deposition region. Glass was the material of choice for the tube due to its low surface roughness and dielectric properties. It was discovered that even though glass is a dielectric, particle attachment allowed the surface to acquire sufficient charge to quench the corona discharge. Therefore, an electrode was attached to the focusing tube to deplete surface charges. However, due again to the requirement of high charge on the ionizing electrode, electrical arcing became significant when the focusing tube was simply grounded. Therefore, a negative charge was added to the focusing tube, resulting in corona sustainment and retention of radial uniformity.

The new chamber was a modification of the AAS system, with two changes. First, the DC negative corona discharge set up was included to induce particle charging. Second, a mixing region purge sidearm was added to keep the concentration of vapor phase particles in the mixing region low. It was shown in the previous section that vapor phase aggregation was strongly affected by concentration in the vapor phase. We determined that much of the vapor phase aggregation was occurring in the mixing region and therefore included this purging system to flush larger stagnant vapor phase aggregates. The final form of the AAS system is illustrated in figure 3-3.

Table 3: Additional AAS control parameters

| Parameter | Abbreviation |
|---|---|
| **Needle voltage** | $V_n$ |
| **Substrate voltage** | $V_{sub}$ |
| **Focusing tube voltage** | $V_{ft}$ |
| **Side arm purge rate** | $U_{sap}$ |

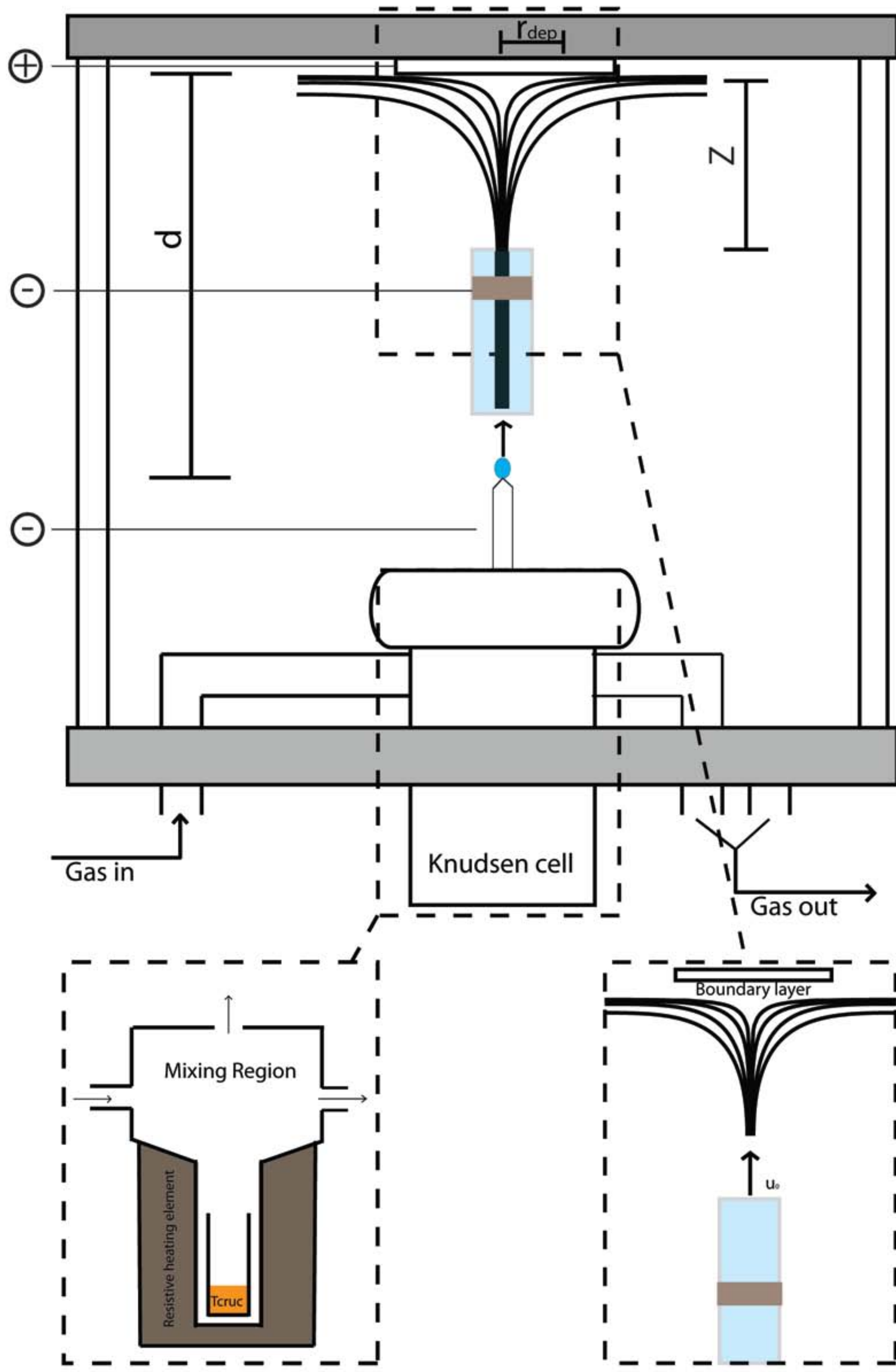


Figure 3-3: Schematic of the AAS system with the addition of particle charging

# Section 4
# Characterization of the Modified AAS System

Recent theoretical studies have developed the relation between certain parameters for atmospheric pressure DC negative corona discharges operating in point to plane mode in an argon atmosphere. A paper published by Dandaron *et al.* described the manner in which a corona discharge could be characterized by experimentally fitting an equation based on established similarity criteria.[6] The criteria of importance were reported by Zhukov *et. al*, and were Ohm's law $\left(\frac{U}{I}\right)$, energy criterion $\left(\frac{I}{CD}\right)$, Reynolds number $\left(\frac{u}{D}\right)$, Knudsen number $(pd)$, and the criterion accounting for the dimensions of the setup $\left(\frac{D}{d}\right)$ where $U$ (kV) is the voltage across a DC negative corona discharge gap, $d$ (cm) is the inter-electrode spacing, $D$ (cm) is the diameter of the chamber, $I$ (uA) is the current across the gap, $u$ (kg sec$^{-1}$) is the mass flow of argon gas, and $p$ (atm) is the pressure of the chamber.[7] From these criteria, an equation was fit to experimental data, resulting in equation 3-2.[6]

(3-2)
$$\frac{U_d}{I} = 0.038\left(\frac{I^2}{uD}\right)^{-0.37}\left(\frac{u}{D}\right)^{-0.68}(pd)^{1.17}\left(\frac{D}{d}\right)^{-0.8}$$

Equation 3-1 can be rearranged to equation 3-3 to be in a more convenient form.

(3-3)
$$U = 0.038\left(\frac{I}{d}\right)\left(\frac{I^2}{uD}\right)^{-0.37}\left(\frac{u}{D}\right)^{-0.68}(pd)^{1.17}\left(\frac{D}{d}\right)^{-0.8}$$

When a plot is constructed which compares the log of the current detected at the substrate versus the log of the voltage across the gap, the expected slope would be 1/0.26 = 3.846, due to equation 3-4 (a rearrangement of equation 3-3).

(3-4) $$\log(I) = \frac{1}{0.26}\, log(\gamma\, U^{-1})$$

Where γ is simply a collection of values (which are held constant) by equation 3-5.

(3-5) $$\gamma = .038\, d^{0.97}\, u^{-0.31}\, D^{0.25}\, p^{1.17}$$

In order to test the validity of applying this model to our system, a series of data was obtained from the AAS system, the results of which are presented in figure 3-4. As shown, the experimental data fits extremely well to the model. In fact, when a least squares fit was performed, the slope of the resultant curve was 1/0.26 (3.846). These results indicate that we can reliably predict the response of the system to alteration of any of the variables, being geometric or electrical. Additionally, there was no current detected at the focusing tube electrode, which indicates that charged species are discharging or depositing on the surface of the tube at an insignificant rate.

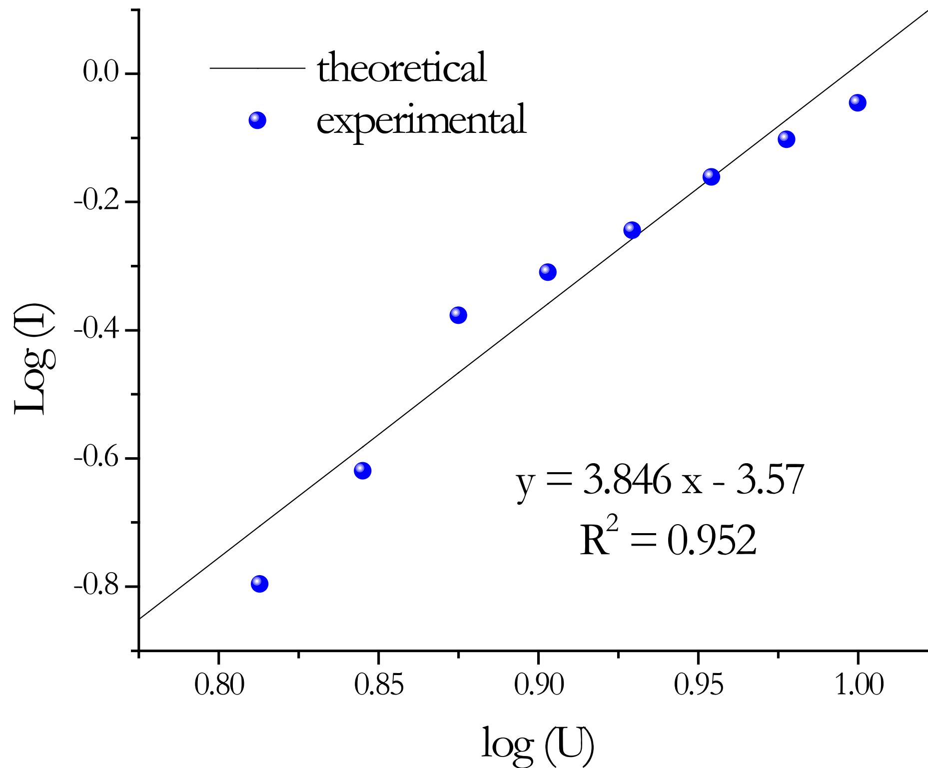


Figure 3-4: Log version of the current/voltage plot showing the slope for experimental data to be 1/0.26 (~3.8). These points were obtained with the values of important variables as follows:

$d$ = 4.75 cm; $p$ = 1.68 atm; $D$ = 12.1 cm; $u$ = 1.56 x $10^{-5}$ kg $s^{-1}$

The voltage applied to the focusing tube electrode was shown to have a small impact on the resultant deposition. Presented in figure 3-5 is a collection of radial absorption plots for differing focusing tube voltages. As shown, when the voltage of the focusing tube is increased from -0.5kV to -2kV, the organic beam seems to become more focused. It is assumed that this effect will be more significant should a larger percentage of the vapor phase particles acquire a charge. The voltage on the focusing tube has no effect however on the falloff outside the deposition region.

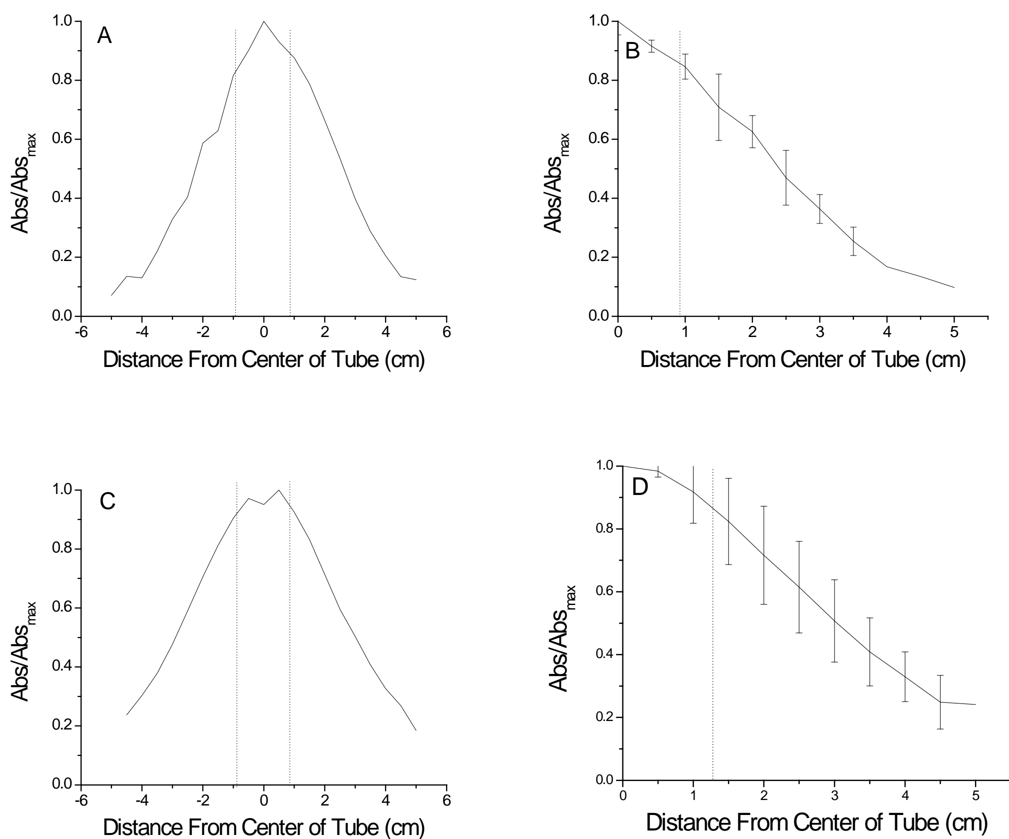


Figure 3-5: Radial distribution plots for different $V_{ft}$ values for anthracene thin films. $V_{ft}$ values were: A & B = -2kV, C & D v -.5kV. Plots B and D were obtained by averaging radial data (ex. 1 and -1) from plots A and C respectively. The plots were obtained with the following run parameters:

d = 4.75 cm; p = 1.68 atm; D = 12.1 cm, u = 1.56 x $10^{-5}$ kg $s^{-1}$; $T_{cruc}$ = 155c; U = 3.1kV; I = 0.47 μA

The requirement for the separation between the focusing tube and the needle introduced the possibility of turbulence in this region. To test for this possibility, several experiments were done with typical experimental parameters. Since anthracene particles fluoresce under ultraviolet light, it was possible to obtain photographs of their averaged trajectories by flooding the chamber with high intensity UV light and removing all visible light. Presented in figure 3-6 is an image taken with a 10 minute exposure time. As shown, the organic beam does in fact spread out in this region, but does not incur a large degree of turbulence. Additionally, the beam showed some response in regards to advection in this region with respect to focusing tube voltage, indicating that this may be the region in which the focusing effect is taking place.

Figure 3-6: Long exposure time photography of the ionization region and portion of the drift region below the focusing tube.

An important consideration for the AAS system is the creation of ozone. Even though the plasma method chosen has been shown a less efficient ozonizer, production of ozone is still possible.[1] Therefore, $O_2$ concentration in in the AAS chamber is kept below 50 ppm $O_2$. It is not possible to remove all of the oxygen however due to the

need for electropositive gasses for formation of a negative corona discharge.[4] Due to the presence of photoemission in this environment, we can conclude that electron temperature can reach as high as 11 eV. This means that fragmentation as well as chemical modification of organic material is possible. In fact, chemical modification in plasmas is a field of intense study.[8,9,10,11] Therefore, it was necessary to test the purity of the films grown by this method.

## Section 5
## Film Purity

Corona discharges are known to create unstable ozone radicals as well as promote chemical reactions, leading to the possibility of impurities depositing on the substrate. This could potentially lead to films that are not applicable to device structures as, discussed in chapter one, impurities can drastically alter the charge transport properties of an OSTF when present in even low concentrations. Therefore, a number of thin films were grown on copper substrates under different conditions and tested for impurities. The impurities deposited were assumed to serve as an accurate representation of the impurities created both in volume and in chemical structure.

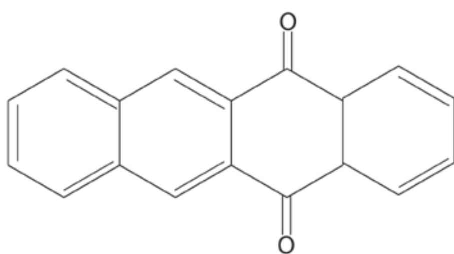


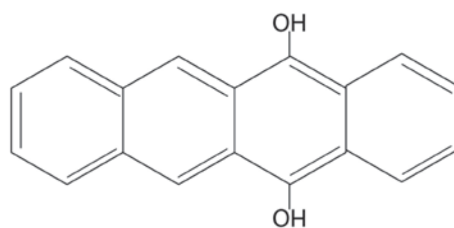


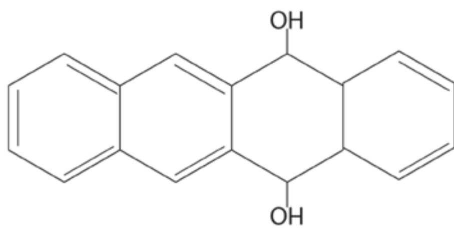


Figure 3-7: Oxidative products of tetracene

Due to its relatively easily oxidized nature, tetracene was chosen as the qualifier for purity studies. Tetracene is known to readily oxidize into one of three oxygen-containing compounds: 5-12,napthacenequinone (NQ), 5,12-dihydroxytetracene, and 5,12-dihydro-5,12-dihydroxytetracene, displayed in figure 3-7.[12] A variety of methods including UV-Vis

spectrometry, Infrared spectrometry, Gas Chromatography/Mass spectrometry and Nuclear Magnetic Resonance spectroscopy were considered for impurity detection. Infrared (IR) spectrometry was chosen due to the ease of detection for both carbonyl and alcohol stretching modes present in the three impurities of tetracene.

The tetracene used in these experiments was obtained from Sigma-Aldrich at 98% purity and underwent no further purification. All IR spectra were obtained using the Thermo Nicolet iS10 IR with an atr sensor. 3-8 shows the IR spectrum of 98% pure tetracene. The presence of a NQ carbonyl impurity peak at 1675nm indicates a detectible quantity of NQ is present even at low concentration. Also, the absence of an O-H stretch around 3400nm indicates that the other two main oxidative products (5,12-dihydroxytetracene or 5,12-dihydro-5,12-dihydroxytetracene) are below the detection limit. Due to the strength of the carbonyl stretching mode of NQ, as well as being reported as the main oxidative product, NQ concentration will be the qualifier for purity. A NQ standard was therefore purchased from Sigma-Aldrich at 97% molar purity and underwent no further purification.

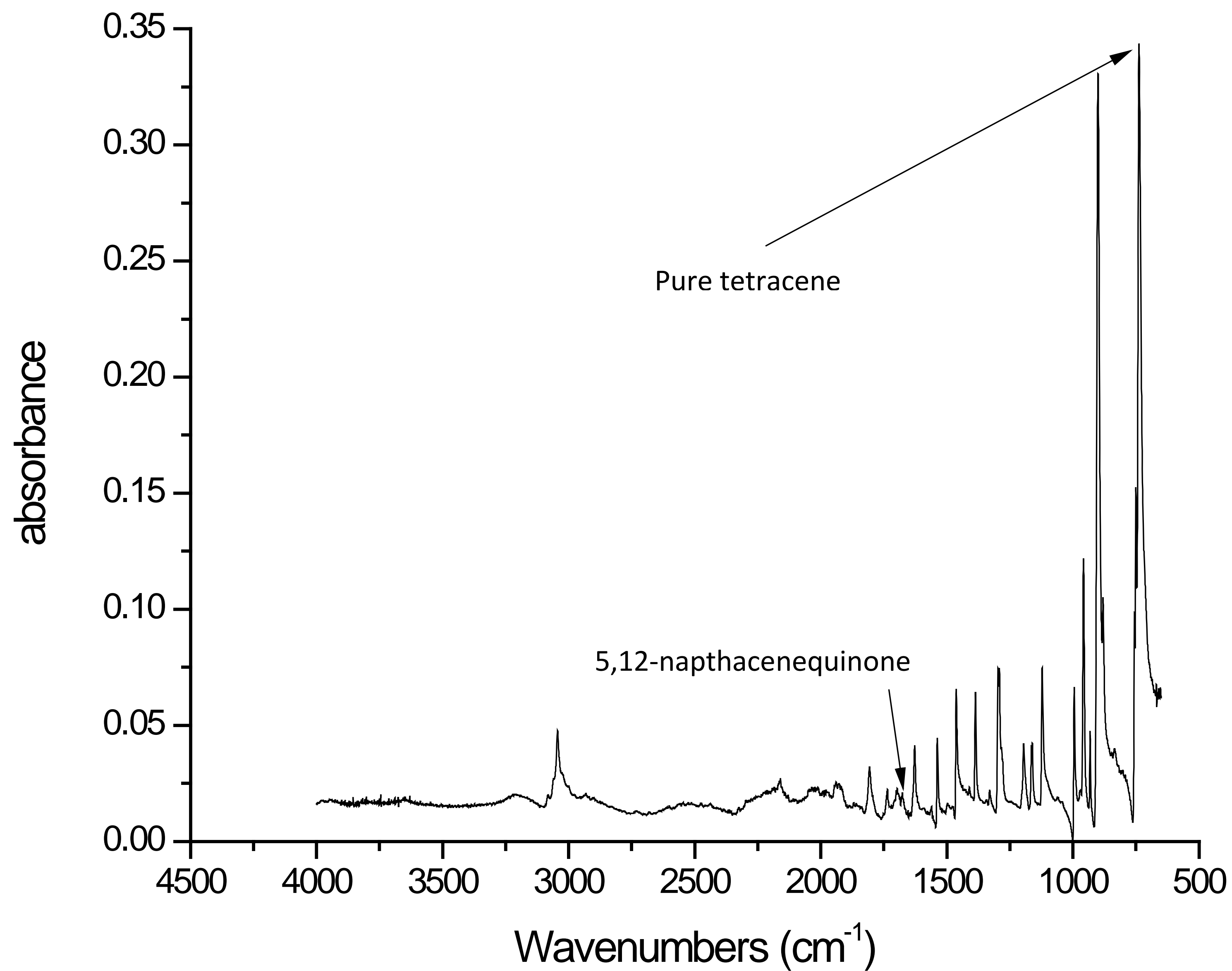


Figure 3-8: IR spectra of 98% pure tetracene sample obtained from Sigma Aldrich. The instrument used was a Thermo Nicolet iS10 IR smart itr

Calibration for the ratio of tetracene/NQ was performed by analyzing 6 samples of varying impurity percentages. The strongest peak in tetracene, an aromatic C-H stretching mode which absorbs at 737 $cm^{-1}$, was chosen as the tetracene reference peak. The strongest peak for NQ, the carbonyl stretching mode which absorbs at 1675 $cm^{-1}$, was chosen as the NQ reference peak. A ratio of the two reference peaks ($R_{peak}$) was normalized ($R/R_{min}$) and plotted against the mass percent ratio of the two compounds ($R_{comp}$) to give a calibration curve. Table four presents the sample's $R_{comp}$ as well as their corresponding $R_{peak}$ and $R/R_{min}$ values. The peak ratios were found to depend on the concentration of NQ by equation 6 (the y offset is due to detection limits), which produced the graph presented as figure 3-9.

Table 4: Percent impurity calibration curve data

| $R_{comp}$ | $R_{peak}$ | $R/R_{min}$ |
|---|---|---|
| **0.020** | 0.025 | 1.0 |
| **0.23** | 0.34 | 14 |
| **0.45** | 1.3 | 51 |
| **0.62** | 1.8 | 70 |
| **0.81** | 2.4 | 96 |
| **0.97** | 2.9 | 110 |

(3-6) $$\frac{R}{R_P} = \left(\frac{mass\ NQ}{mass\ tetracene + mass\ NQ} + 1.3\right)/1.2$$

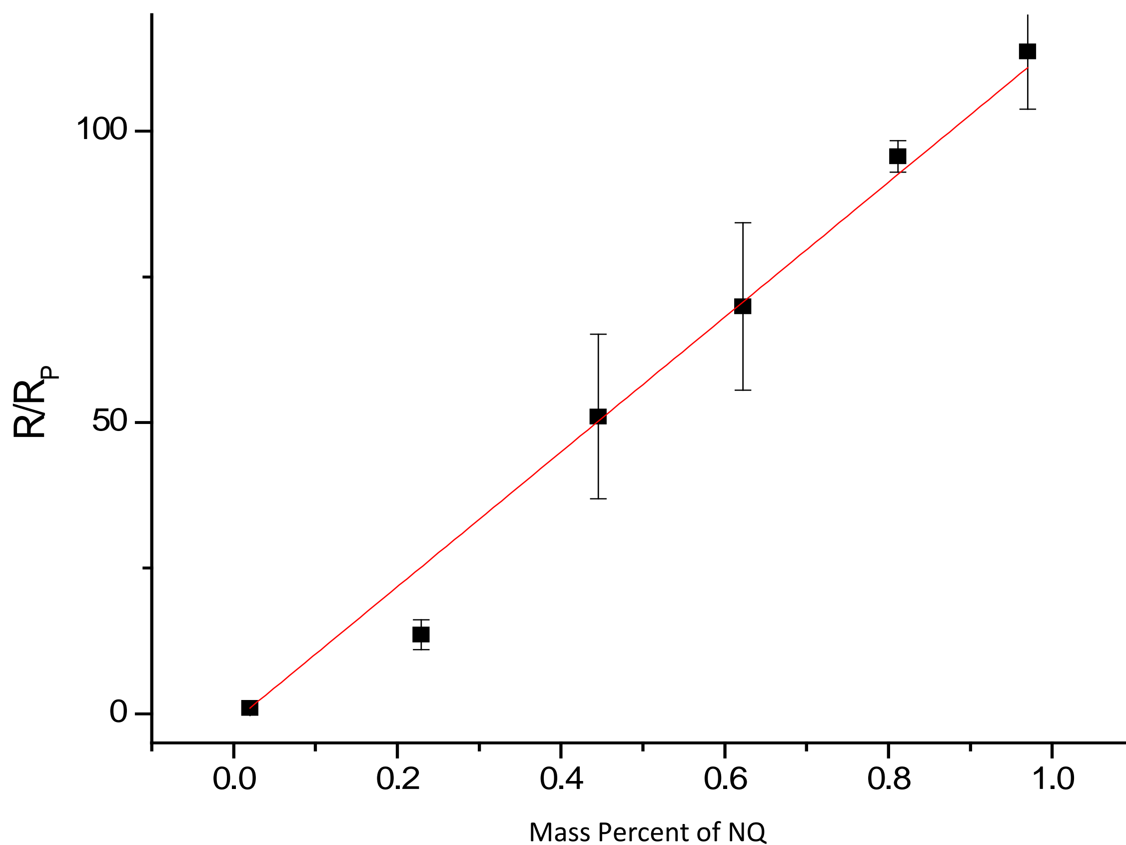


Figure 3-9: Tetracene impurity calibration curve calculated for the presence of NQ

Using the now calibrated $R/R_P$ values, the purity of a tetracene film grown by the plasma spray method under ambient conditions was calculated. As expected, the oxidative product NQ was present in a higher concentration when the tetracene was subjected to a corona discharge. In order to acquire a more accurate background, a tetracene film was grown by sublimation with no corona. Sublimation is a well-established purification method for organic semiconductors, and in this specific case, purification by sublimation lowered the NQ levels to 1.6%.[13,14] (The percentage of impurity present in the film grown with no particle

charging more accurately depicts the levels of impurity of grown films then that of tetracene taken from a bottle.)

In order to counteract oxidation, a number of steps were taken. Initially, the overall concentration of oxygen gas in the plasma spray chamber was decreased by purging with argon. Argon gas was chosen due to its ability to reliably form a corona discharge.[15,16,17] It was found that by simply lowering the concentration of oxygen gas below 50 ppm that percentage of NQ present was cut in half. A number of additional steps were taken in an attempt to further reduce the creation of NQ, including use of radical scavengers (such as t-butanol) and incorporation of gas scrubbers to increase the purity of the incoming argon gas. However, these modifications either made no difference or in some cases increased the oxidation. It was also discovered that the positively charged ions resultant from the plasma charging did have a lower NQ concentration but allowed for the formation of an unknown product, possibly an epoxide due to the appearance of 2 peaks at 1010 and 1073$cm^{-1}$. When water vapor was added to the inlet gas, the percent of NQ was lowered almost to the starting purity. This unexpected result may be due to water colliding with high energy electrons and forming a charged shell around vapor phase molecules. The percent of 5,12-napthacenequinone impurity for various plasma environments is presented in figure 3-10.

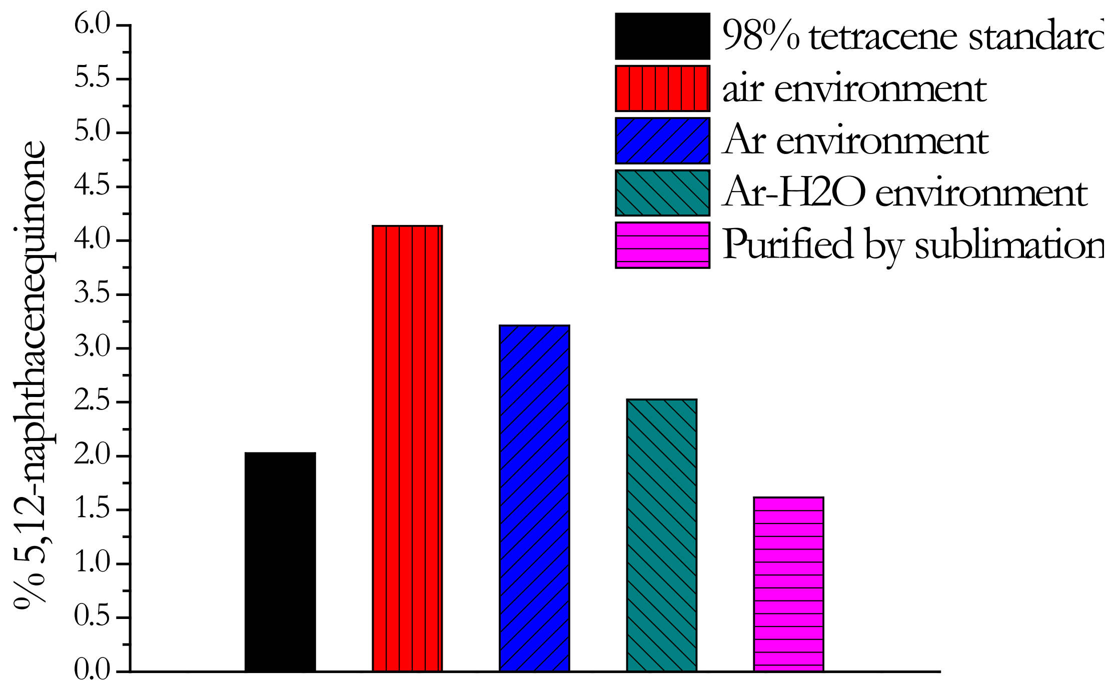


Figure 3-10: Purity of tetracene films grown by AAS in different plasma environments

Anthracene, another member of the polyacene family, was also tested for plasma induced impurities. The main oxidation product of anthracene is anthraquinone and thus should show a very strong carbonyl stretch in IR spectroscopy. However, an anthracene film grown in an argon environment with less than 50 ppm $O_2$ showed no evidence of oxidation.

## Section 6
## Modeling Deposition Rate

The destructive nature of the corona discharge was minimized, and the environment has been characterized. Now I will characterize the discharge in terms of particle charging and its effect on deposition rate. Incorporation of electrostatic attraction between charged particles and the substrate requires the addition of another characteristic force in the deposition model introduced in chapter 2. With the inclusion of electrostatic forces, the Sherwood number now includes an electrostatic transport term, $K_E$ (unitless), according to equation 3-7.

(3-7) $$Sh \approx 0.616Pe^{\frac{1}{3}} - K_g + K_E$$

The electrostatic transport term is calculated again by a ratio of work, in this case the electrostatic attraction force over the same distance (radius of particle), to the thermal energy by equation 3-8:[18]

(3-8) $$K_E = \frac{qE_{sub}r_p}{k_BT}$$

Where $q$ (C) is the charge on a particle, $E_{sub}$ ($m^{-1}$ $C^{-1}$) is the electric field created by the substrate, $r_p$ (m) is the radius of a particle, the Boltzmann constant and the temperature. The field created by the substrate is calculated assuming a circular disk by equation 3-9:

(3-9) $$E_{sub} = \frac{q_{sub}}{\epsilon_0 \pi {r_p}^2}$$

Where $q_{sub}$ (C) is the charge on the substrate, and $\varepsilon_0$ (F $m^{-1}$) is the permittivity of free space. The charge on the substrate is calculated by equation 3-10:

(3-10) $$q_{sub} = V_{sub} C_{self}$$

Where $C_{self}$ (C $V^{-1}$) is the self capacitance of the substrate and $V_{sub}$ (V) is the voltage applied to the substrate. The self capacitance of the substrate is calculated assuming a radially uniform disk by equation 3-11:

(3-11) $$C_{self} = \epsilon_0 2^{3/2} \pi r_{sub}$$

Where $r_{sub}$ (m) is the radius of the substrate (the size of the deposition area). All of these equations assume 100% efficient particle charging. However, a reasonable estimate for particle charging efficiency was determined experimentally (see below) to be ~0.005% (commercial grade corona charging guns for powder coating typically run with ~5% efficiency).[19] Due to the relative concentrations of free electrons and tetracene molecules in the ionization region and the low probability of electron attachment, we assume that if a tetracene molecule does in fact acquire a charge, it will only do so once and therefore the magnitude of the charge will be that of one electron. Even with the maximum charge on a tetracene molecule being one electron, the electrostatic term dominates the deposition equation, showing the relative strength of this effect.

When these conditions are added to the deposition rate equation from chapter 2, the following plot is obtained with $n_0 = 10^{18}$ molecules $m^{-3}$, $u_0 = 2.5$ m/s, $\mu = 1.5 \times 10^{-5}$ kg $m^{-1}$ $sec^{-1}$, $V_{sub} = 2kV$. We now see a theoretical increase in deposition rate by ~3 orders of magnitude, shown in figure 3-11 (As a reference, a plot with no particle charging is given as the red dashed line).

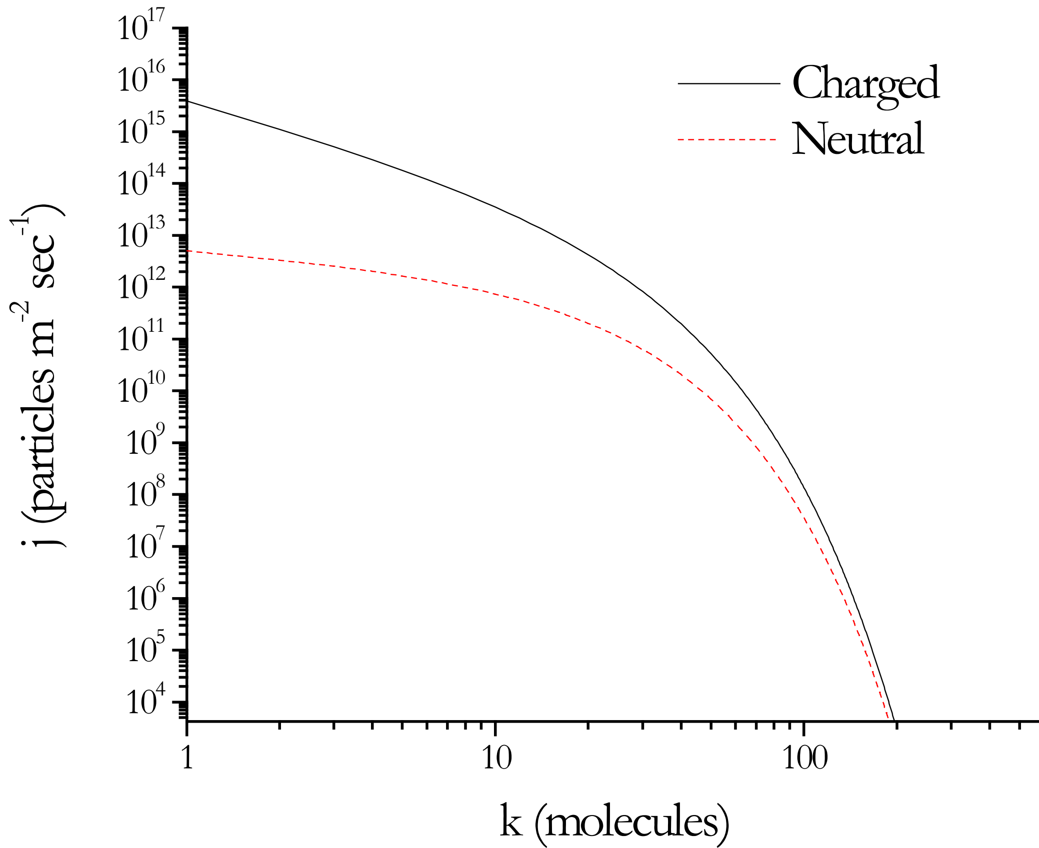


Figure 3-11: Deposition rate versus particle size assuming uniform charging probability with electrostatic forces. The input parameters were: $n_0 = 10^{18}$ molecules $m^{-2}$; tof = 0.02 sec; charging efficiency = 0.005%

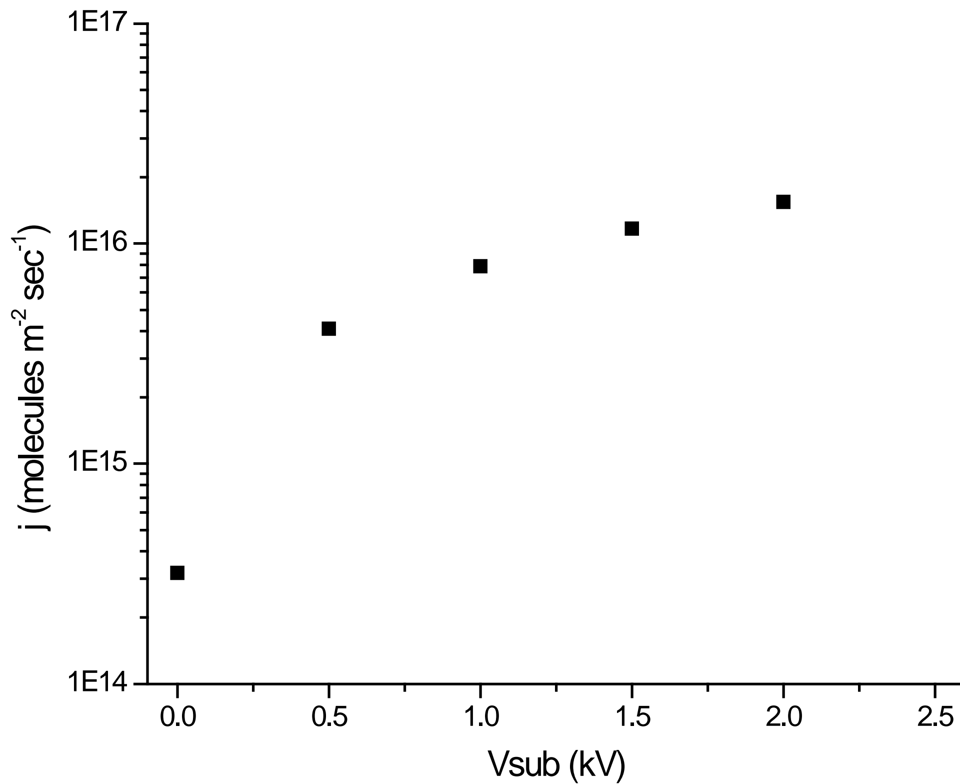


Figure 3-12: Theoretical deposition rate as a function of substrate voltage with .005% assumed particle charging efficiency. $n_0 = 10^{18}$ molecules $m^2$; tof = 0.02 sec

We now see a three orders of magnitude increase in deposition rate, with the effect of substrate voltage as follows in figure 3-12. For all values of $V_{sub}$ above zero, deposition rate increases relatively linearly with increase in substrate voltage. When a substrate voltage of zero is included in this model, misleading results are obtained. This model cannot account for image charges (an induced charge due to close proximity of a charged species) and therefore cannot accurately predict the case for a grounded substrate. However, the model does accurately predict the increase in deposition rate (see below).

These results were confirmed experimentally, as presented in figure 3-13, which was obtained by the AAS system with the following run parameters: $d$ = 4.75 cm; $p$ = 1.68 atm; $D$ = 12.1 cm; $u$ = 1.56 x $10^{-5}$ kg $s^{-1}$; $T_{cruc}$ = 245 $^0$C; $V_{FT}$ = -500 V. Figure 4-2 shows not only that a significant increase in deposition rate is attainable by particle charging, but also that the main product of the AAS charging method is negative, due to the fact that when the substrate is given a negative charge, the deposition rate decreases significantly.

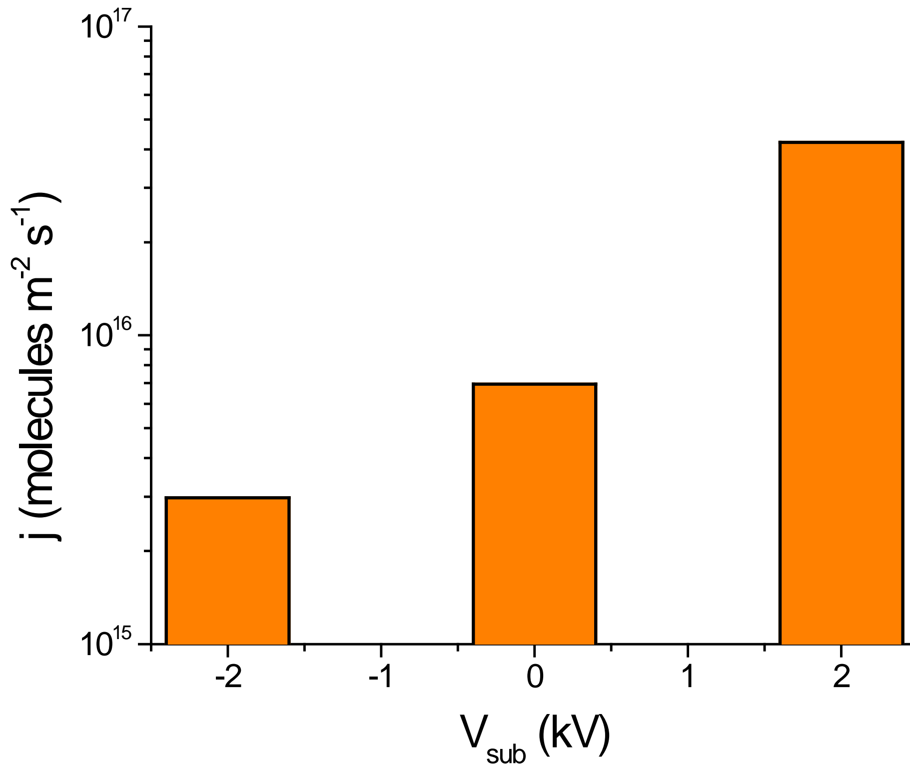


Figure 3-13: Experimental deposition rate as a function of substrate voltage.

As shown in the previous section, the required modifications to the AAS system were added and characterized. The system now exhibits a significant increase in deposition rate as well as the ability to keep concentration of vapor phase molecules in the mixing region low by means of mixing region purging. The AAS system is now capable of growing thin films of organic semiconductor at short timescales without sacrificing film quality. Additionally, the inclusion of particle charging has shown to be only minimally destructive. Presented in the following chapter are the results of the completed AAS system which proves its capability as a quality OSTF growth method.

## Chapter Three References


**1** W. R. Rutgers, E. M. van Veldhuizen, Fundamentals of Non-Thermal Gas Discharges at Atmospheric Pressure, in *Electrical Discharges for Environmental Purposes: Fundamentals and Applications*, 1, E. M. van Veldhuizen, Eds., Nove Science Publishers: New York, 2000; 5-15

**2** P. Hammond, *J. Phys. B: Atomic, Molecula and Optical Physics*, **1996**, 29

**3** K. Hiraoka, S. Fujimaki, S. Kambara, H. Furuya, S. Okazaki, *Rapid Communications in Mass Spectrometry*, **2004**, 18

**4** Sigmond R S and Goldman M 1983 Corona discharge physics and applications *Electrical Breakdown and Discharges in Gases: B. Macroscopic Processes and Discharges* ed E E Kunhardt and L H Luessen (New York: Plenum) pp 1–64

**5** A. Fridman, Introduction to theoretical and applied plasma chemistry, in *Plasma Chemistry,* 1, Cambridge University press: Philadelphia, **2008**, 3-36

**6** G.-N. B. Dandaron, V. B. Shagdarov, B. Ts. Bazarsadaev, *Technical Physics*, **1997**, 77

**7** M. F. Zhukov, I. M. Zasypkin, A. N. Timoshevskiĭ, et al., *Electric-Arc Generators of Thermal Plasmas*, **1999**

**8** J. D. Skalny, P. Lukac, *Acta Physica Universitatis Comenianae*, **1992**, 1

**9** R. J. Van Brunt, L. Sieck, I. Sauers, M. C. Siddagangappa, *Plasma Chemistry and Plasma Processing*, **1988**, 8

**10** P. Iwo, B. Witkowska, *Zeszyty Nauwe Politechniki Slaskiej, Chemia*, **1973**, 63

**11** M. Sato, B. Sun, T. Ohshima, Y. Sagi, *J. Adv. Oxidation Tech.*, **1999**, 4

**12** R. Dabestani, M, Nelson, M. E. Sigman, *Photochemistry and Photobiology*, **2008**, 64, 1

**11** J. Pflaum, J. Niemax, A. K. Tripathi, *Chem. Phys.*, **2006**, 325, 1

**12** O. Yosuke, K. Noriyuki, U. Akihito, *Jpn. Kokai Tokkyo Koho*, **2005**, JP 2005111303

**13** V. D. Peskov, *Proc. Int. Conf. Phenom. Ioniz. Gasses*, **1977**, 92

**14** H. M. Gaunt, J. D. Craigs, *Nature*, **1951**, 167

**15** G. L. Weissler, *Phys. Rev,* **1943**, 63

**16** R. J. Van Brunt, L. Sieck, I. Sauers, M. C. Siddagangappa, *Plasma Chemistry and Plasma Processing*, **1988**, 8

**17** G. –N. B. Dandaron, B. B. Baldanov, *Plasma Physics Reports*, **2007**, 33

**18** D. W. Cooper, M. H. Peters, R. J. Miller, *Aerosol Sci. & Technol.* **1999**

**19** J. F. Hughes, *J. Electrostatics*, **1989**, 23

# Chapter Four

## Results, Conclusions and Future Work

This chapter summarizes some of the main findings discussed earlier in the thesis and presents results demonstrating use of the AAS method to deposit films of anthracene and tetracene. Recall that the goals of this project were to:

1. Develop a model to account for vapor phase aggregation, deposition rate, and particle charging.
2. Reduce the extent of vapor phase aggregation to a level compatible with liquid coated substrates.
3. Increase reproducibility
4. Significantly reduce the timescale required for film deposition

A number of steps were taken to achieve these goals, beginning with the development of a theoretical framework.

## Section 4-2
## Theoretical Framework

The aggregation model presented in chapter two provides an approximation for vapor phase aggregation. It predicts that there will in fact be a particle size distribution due to the AAS system being run at near ambient pressure and temperature. The theoretical particle size distribution was shown to depend strongly upon time of flight and initial concentration of vapor phase particles, and to a lesser extent, gas dynamic viscosity. However, it is only valid for short timescales and only calculates collisions between like sized particles. This assumption was made in order to eliminate the need for complex calculation which would require sophisticated computer modeling. Future work must be done to develop a model for vapor phase aggregation which can account for collisions between all particle sizes.

The deposition rate equations presented in chapters two and three provide a semiqualitative picture of how deposition in the AAS system is effected by the particle size distribution. They also provide insight into the boundary layer's filtering effect as well as an explanation as to why, even though particles of up to 500 molecules in size can readily be formed in the vapor phase, they are not present in the resultant films. The deposition rate equation also allows for calculation of charged species deposition. Future work should be done to include image charges and to more accurately represent the effect of a negatively charged substrate. The estimate for the particle charging efficiency should also be refined, as the estimate given was fitted by experimental data and assumes no other discrepancies between the deposition rate equations and the experimental results.

## Section 4-3
## Improvements

The degree of vapor phase aggregation has been significantly reduced over the course of this work. Initially, there was no mixing region, and vapor phase particles had to pass through a region of high concentration in order to reach the substrate. The inclusion of the mixing region helped reduce the concentration in the chamber, and thus lead to films with fewer vapor phase aggregates deposited. The size of the mixing region was reduced and a sidearm purge was added to further reduce the degree of aggregation in this region.

With these modifications, the AAS system became capable of growing films of tetracene and anthracene with no large vapor phase aggregates present. To demonstrate this, representative images are shown in figure 4-1 of anthracene and tetracene films deposited onto ITO coated glass, which show evidence of surface based growth and therefore small, mobile particles deposited. One should note that the high fractal dimension, dendridic crystals are typically formed when there are small mobile species present on the surface of the substrate. Additionally, the evidence presented in chapter two, section five show without

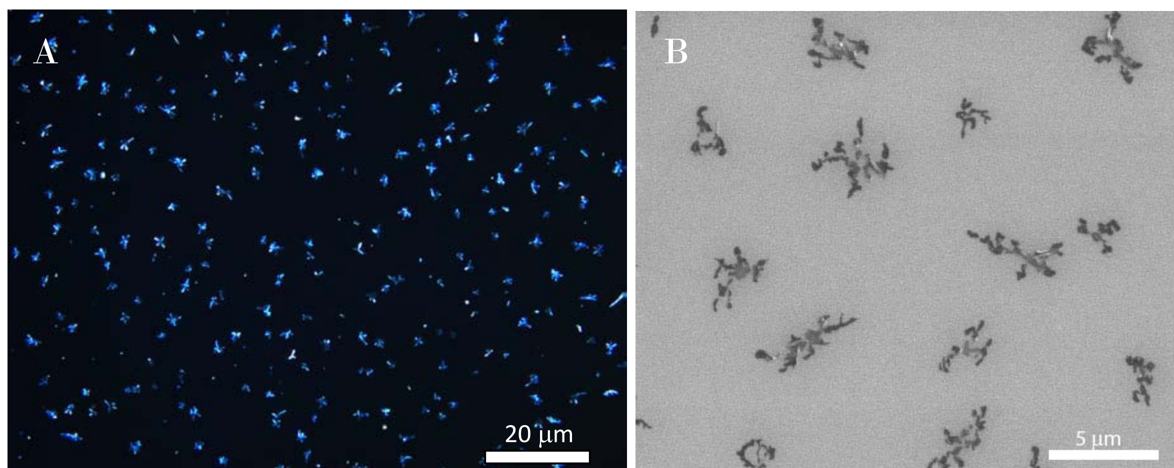


Figure 4-1: Films of A) anthracene grown on ITO and B) tetracene grown on silicon oxide which show evidence of surface based growth.

a doubt that crystals are in fact growing on the surface of the substrate; a behavior which would be very unlikely if the arriving particles were of substantial size.

In order to test whether the AAS system is capable of growing films of comparable quality in 30 minutes to those grown in 14 h by the OVLS method, a number of films were grown. Results with anthracene showed that the AAS system is capable of reproducibly depositing small particles of anthracene on a substrate under optimal run parameters. Also, the AAS system has proven capable of growing thin films of anthracene in the LC ZLI-3417 with relatively high nucleation density while retaining phase purity and crystallographic orientation in less than 30 minutes, as presented in figure 4-2. The phase purity of the film is suggested by the fact that all of the crystals form the same crystallographic shape. The fact that the film is highly ordered can be discerned by the direction that the crystals are pointing. We do not know which direction is the most beneficial for charge transport, but since all crystals more or less share the same orientation, it is not a needed piece of information at this time as contacts could be placed on any part of the substrate. Additionally, the anthracene film grown shows uniform coverage which is an important trait when considering incorporation into devices.

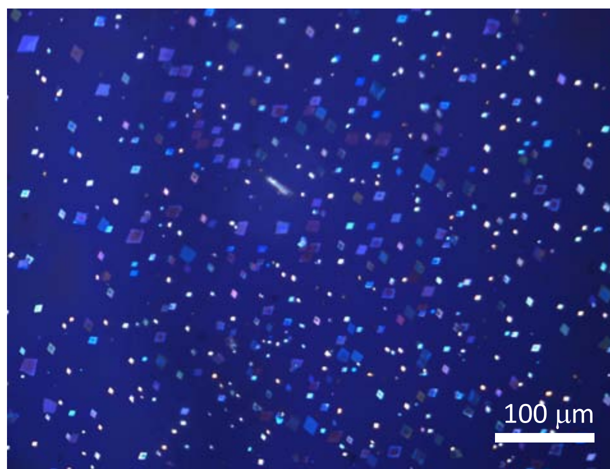


Figure 4-2: Anthracene thin film grown by the AAS method on an ITO coated glass substrate with a polyimide alignment layer and a ~1500nm thick film of the LC ZLI-3417 with the following parameters:

$d = 4.75$ cm; $p = 1.68$ atm; $D = 12.1$ cm, $G = 1.56 \times 10^{-5}$ kg s$^{-1}$; $T_{cruc} = 150$c; $U = 4.2$kV; $I = 0.43$ µA

The reproducibility of the AAS method has improved significantly. However, the reproducibility is still not at a level where the AAS system would be commercially viable. The sublimation rate can vary significantly from run to run, perhaps due to an inefficient Knudsen cell or small variations in solid particle size and volume. Possible solutions to these problems include the design of a new heating region, better milling of the solid powder, and more accurate measurements of the amount of powder used.

The inclusion of an electric field could possibly remove the radial uniformity of the deposition region due to a non-uniform field produced from the substrate. To test this assumption, an experiment was performed which showed that within the deposition region, the rate of deposition is in fact uniform. The experiment was performed by fitting a completely opaque mask with a 0.7 mm radius hole through in the path of a beam of light emitted from an UV/Vis spectrophotometer. The mask was then moved in 0.5 mm steps to make a 2 dimensional map of the sample. The results of this study are presented as figure 4-4, and a representative optical image of a thick film of anthracene is presented as figure 4-3. Consistent deposition rate inside the deposition region is beneficial, as it leads to highly uniform thin films. One can imagine that if a thin film has anisotropic density, it would severely affect the transport of charge carriers.

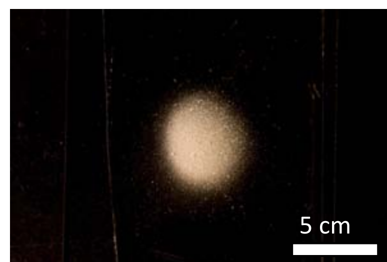

Figure 4-3: Optical image of an anthracene film.

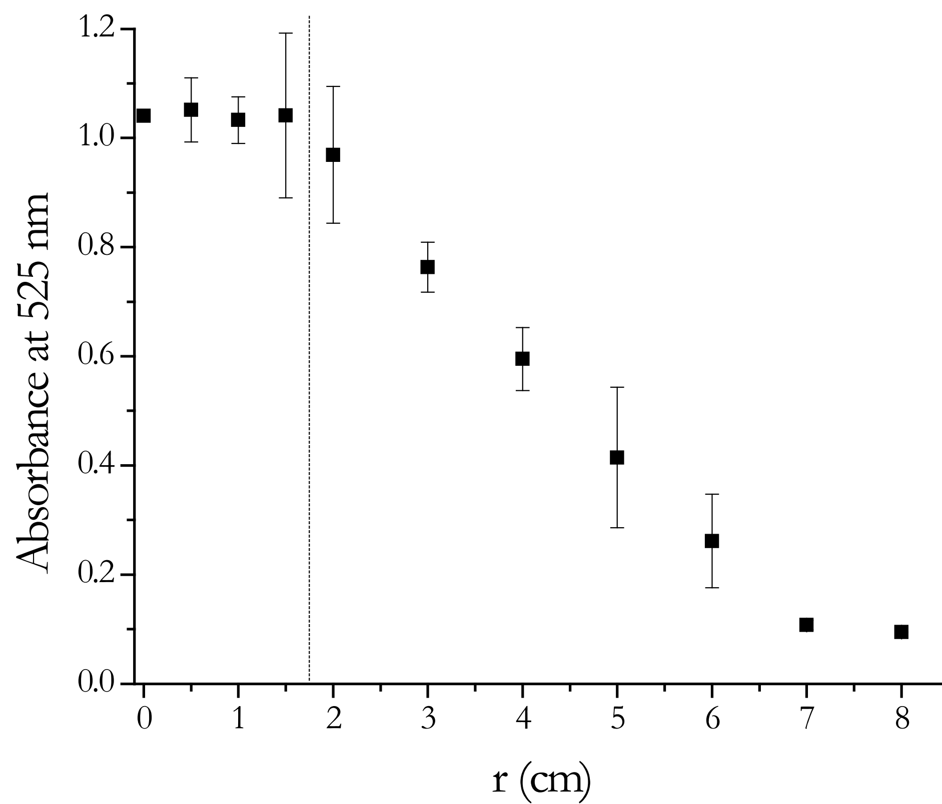


Figure 4-4: Radial UV-Vis intensity study of a tetracene thin film grown by the AAS method. Note that within the deposition region (before the dotted line), the deposition is fairly uniform.

## Section 4-3
## Patterning

Organic semiconductor thin film based devices sometimes require their semiconducting layer to be grown into complex patterns. Therefore, compatibility with patterning methods such as shadow masking is a significant advantage. Presented in figure 4-5 is an optical image of a substrate which was patterned by attaching a thin sheet of patterned plastic on top of an ITO substrate to selectively expose areas to the deposition beam. Figure 4-5 shows the boundary between exposed and unexposed areas with the orange area being the tetracene film and the dark area being the unexposed area where we see no deposition. As shown, the inclusion of the shadow mask does not hinder the deposition as inside the deposition area, as there is no variation in coverage. Also, as expected, there is no tetracene outside the desired area.

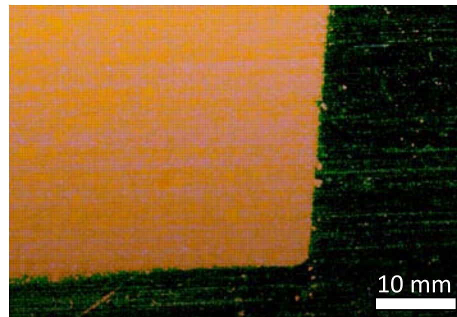


Figure 4-5: Tetracene patterned edge by shadow masking.

In addition to shadow masking, a new type of patterning was attempted, entitled electro masking, in which the substrate was patterned with conductive and nonconductive areas to promote preferential deposition. The results of the electro masking experiments showed that there is promise to this type of patterning, as shown in figure 4-6. Figure 4-6A shows an indium tin oxide coated slide with half of the conductive layer removed. A tetracene film was then grown on the substrate, with the conductive side held at 2kV (lower half of the image). As shown, the volume of tetracene (and thus the deposition rate) on the

conductive area was much greater than that of the-non conductive area. Similar results were obtained for a glass slide with patterned aluminum electrodes, shown in figure 4-6B. This type of patterning shows promise, however the deposition rate on the nonconductive areas remained large, possibly due to the low charging efficiency of the AAS system (estimated 0.005%). Due to the results presented in chapter 3, section 6, if a substrate could be patterned with both positively and negatively charged areas, one would expect that the deposition in the undesired (negative) areas would be significantly less.

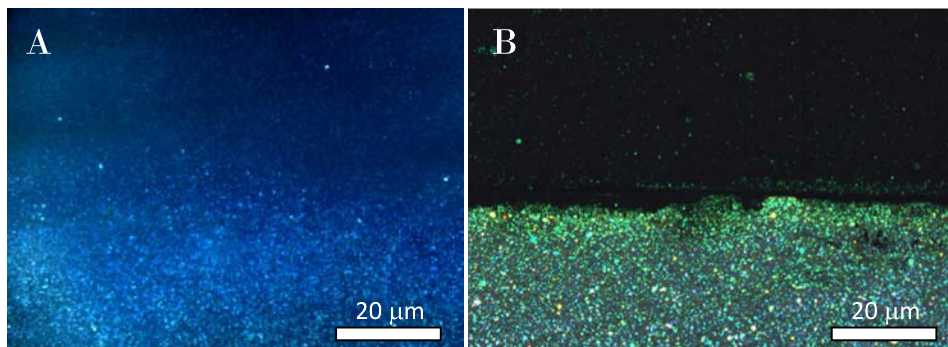


Figure 4-6: Optical image of the electro masked substrates. The lower regions were the conductive areas while the upper regions were nonconductive. A) Half ITO coated glass substrate B) grown aluminum electrodes on a glass substrate

## Section 4-4
## Summary

This thesis describes the development of the AAS system as well as its ability to grow thin films of the organic semiconductors tetracene and anthracene. The AAS system was first tested without particle charging and showed promising results. A theoretical framework for both cluster formation and particle deposition was developed, which allows for prediction of system responses to variables such as sublimation rate and flow rate. When particle charging was excluded, particles reaching the substrate were small enough to undergo diffusive motion even though aggregation of particles was occurring at a significant rate. The AAS system was able to grow films of tetracene and anthracene without particle charging, but required exceedingly long run times to do so. Therefore, particle charging was incorporated, which resulted in a three order of magnitude increase in deposition rate. Also, films of anthracene and tetracene grown with the inclusion of particle charging indicated that the arriving particle size distribution was small enough to undergo diffusive motion. Preliminary AAS system experiments with the inclusion of particle charging showed that high density, phase pure oriented films of anthracene can be grown in the LC ZLI-3417. Also, the AAS method is compatible with shadow masking. The AAS system is therefore a powerful tool for growing organic semiconductor thin films.